Charge and Exciton Dynamics in Organic Optoelectronic Devices

by

Caleb Coburn

A dissertation submitted in partial fulfillment
of the requirements for the degree of
Doctor of Philosophy
(Physics)
in The University of Michigan
2019

Doctoral Committee:

Professor Stephen Forrest, Chair
Professor Jay Guo
Professor Jennifer Ogilvie
Associate Professor Kai Sun

Caleb Coburn

calebcob@umich.edu

ORCID iD: 0000-0003-4299-2629

For Jessie

ACKNOWLEDGEMENTS

It has been said that a dwarf may see further than a giant when standing on its shoulder. Just as Newton famously attributed his achievements to the giants that preceded him, so my work would not have been possible alone. In the course of my graduate work, I've had the great pleasure of being introduced to a scientific community that has both paved the way for my own contributions to the field and supported me through the journey. Of course, foremost among them is Prof. Stephen Forrest who mentored and advised me during my graduate school experience. The example, opportunities, insights, and training he provided shaped my growth as a scientist. Thank you.

I am also grateful to the senior students who mentored me as a new student: first Yifan Zhang, who carefully trained me and introduced the rigor that would be expected of me. I also owe thanks to Michael Slootsky, Kyusang Lee, Xin Xiao, and especially Jaesang Lee, who worked closely with me on several projects and mentored my early work on OLEDs. I appreciate the friendship and support of my contemporaries, including Quinn Burlingame, Yue Qu, Anurag Panda, Xiao Liu, Xiaozhou Che, Dejiu Fan, Jongchan Kim, and the other students and post docs who were a part of my graduate experience.

A special mention goes to Eva Ruff. She goes above and beyond as our Administrative Assistant: she is a friend and support, and assisted with the editing of this thesis.

Most importantly, I am grateful to my wife, Jessica, who was next to my side through each step. Her grounding influence has motivated me to work hard and try to be my best self. Her patience with my long hours in the lab, sympathy when things didn't go well, and excitement when they did have made the journey much sweeter. Also, thanks go to my family, who support me and prepared me to succeed.

TABLE OF CONTENTS

LIST OF FIGURES

Figure

LIST OF TABLES

Table

LIST OF ABBREVIATIONS

ALD atomic layer deposition

CCD charge-coupled device

CCT correlated color temperature

CGL charge generation layer

CRI color rendering index

DFT density functional theory

EBL electron blocking layer

EIL electron injection layer

EL electroluminescence

EML emission layer

EQE external quantum efficiency

ETL electron transport layer

FWHM full width at half maximum

HBL hole blocking layer

HJ heterojunction

HIL hole injection layer

HOMO highest occupied molecular orbital

HTL hole transport layer

IMF index matching fluid

IPES inverse photoelectron spectroscopy

IQE internal quantum efficiency

ISC intersystem crossing

J*–*V current density–voltage

LCD liquid crystal display

LED light emitting diode

LPE luminous power efficiency

LUMO lowest unoccupied molecular orbital

MOS metal-oxide-semiconductor

OCCD organic charge-coupled device

OLED organic light emitting diode

OPV organic photovoltaic

PHOLED phosphorescent organic light emitting device

PLQY photoluminescence quantum yield

PV photovoltaic

SSL solid-state lighting

SWOLED stacked white organic light emitting device

STA singlet-triplet annihilation

TIR total internal reflection

TPA triplet-polaron annihilation

TTA triplet-triplet annihilation

UPS ultraviolet photoelectron spectroscopy

VTE vacuum thermal evaporation

LIST OF CHEMICALS

Alq_3 tris-(8-hydroxyquinoline)aluminum

BAlq bis(8-hydroxy-2-methylquinoline)-(4-phenylphenoxy)aluminum

BPhen bathophenanthroline

BPyTP2 2,7-bis(2,20-bipyridine-5-yl)triphenylene

C_{60} fullerene carbon-60

C_{70} fullerene carbon-70

CBP 4,4'-bis(9-carbazolyl)-1,1'-biphenyl

CPD di(phenyl-carbazole)-N,N'-bis-phenyl-(1,1'-biphenyl)-4,4'-diamine

CZSi 9-(4-tert-butylphenyl)-3,6-bis(triphenylsilyl)-9H-carbazole

DBP tetraphenyldibenzoperiflanthene

DCM2 4-(dicyanomethylene)-2-methyl-6-julolidyl-9-enyl-4H -pyran

DTDCPB 2-[(7-(4-[*N*,*N*-bis(4-methylphenyl)amino]phenyl)-2,1,3-benzothiadiazol-4-yl)methylene]propane-dinitrile

DTDCTB 2-((7-(5-(dip-tolylamino)thiophen-2-yl)benzo[c][1,2,5]thiadiazol-4-yl) methylene)malononitrile

FIrpic bis[2-(4,6-difluorophenyl)pyridinato-C2,N](picolinato)iridium(III)

HATCN hexaazatriphenylene hexacarbonitrile

ITO indium tin oxide

Ir(5'-Ph-ppy)$_3$ iridium (III) tris[2-(5'-phenyl)phenylpyridine]

Ir(dmp)$_3$ iridium (III) tris[3-(2,6-dimethylphenyl)-7-methylimidazo[1,2-f] phenanthridine]

Ir(ppy)$_3$ tris[2-phenylpyridine]iridium(III)

Liq 8-hydroxyquinolinato lithium

mer-Ir(pmp)$_3$ mer-tris-(N-phenyl, N-methyl-pyridoimidazol-2-yl)iridium (III)

mCBP 4,40-bis(3-methylcarbazol-9-yl)-2,20-biphenyl

NPD N,N'-Di(1-naphthyl)-N,N'-diphenyl-(1,1'-biphenyl)-4,4'-diamine

PQIr iridium (III) bis(2-phenyl quinolyl-N,C20) acetylacetonate

PtOEP Pt (II) octaethylporphine

SubPc boron subphthalocyanine chloride

TPBi 2,2',2"-(1,3,5-benzenetriyl tris-[1-phenyl-1H-benzimidazole]

Tris-PCz 9,9'-diphenyl-6-(9-phenyl-9H-carbazol-3-yl)-9H,9'H-3,3'-bicarbazole

ABSTRACT

Organic optoelectronics use carbon-based molecules to interface between light and electrical signals. The operation of these devices is determined by the dynamic behaviors of their charges and excited states. For example, organic light-emitting diodes use injected electrical charges to form excited states that, in turn, emit light. Organic photovoltaics and photodetectors operate by the reverse process. Understanding the dynamics of charges and excited states is crucial to designing high performance devices.

The first part of this thesis focuses on understanding charge and exciton dynamics in organic light emitting devices. First, charge balance and exciton confinement in blue-emitting phosphorescent organic light-emitting diodes are studied using sensitizer methods and an analytical model based on drift-diffusion transport. We find that triplet excitons leak into the hole transporting layer at high current densities and improve device performance by incorporating a high triplet energy blocking layer to prevent such leakage. The impact of changes in charge balance and exciton confinement on the lifetime of blue phosphorescent organic light emitting diodes is also investigated. We find that that contribution of loss of charge balance is negligible, and that increased exciton leakage is responsible for less than 4% of luminance loss. The understanding gained in these studies is then applied to the design of a highly reliable stacked white-emitting device for solid state lighting. These devices employ

red-emitting blocking layers as well as highly stable, low voltage charge generation layers. A five-stack device achieves 2780 K coordinated color temperature with a high color rendering index of 89 and 80±20 krs lifetime (T70, 1000 cd/m^2).

The second part focuses on charge diffusion in organic heterostructures laterally, i.e, in plane with the thin film. Because of the low charge mobilities of organic semiconductors, organic devices are typically thin with negligible lateral charge transport. We show that charge can be transported laterally across centimeters in certain organic heterostructures. This phenomenon arises from the combination of a trap-free, high diffusivity channel and energetic confinement of carriers that prevents rapid recombination. The confining energy barrier arises from a polarization shift of the acceptor material when blended with a highly dipolar donor. Lateral transport heterostructures are then used to develop the first organic charge-coupled devices. We observe clear charge-coupled transport of photogenerated charge packets in a linear four-pixel shift register. Calculations indicate that millisecond readout times are possible using many-pixel organic charge-coupled sensors, and strategies for the improvement of these devices are discussed.

CHAPTER I

Introduction

Organic optoelectronic devices are increasingly prevalent in modern technology. Among them, organic light emitting diodes (OLEDs) have met with the most commercial success due to their desirable properties for use in information display applications. Other notable organic optoelectronic devices still in development or in the early stages of commercialization include organic photovoltaics (OPVs), OLEDs for solid-state lighting (SSL), thin film transistors, photodetectors, lasers, and more. Inorganic semiconductors are more commonly used for many of these optoelectronic device applications, i.e, light emitting diodes (LEDs), photovoltaics (PVs), etc. The viability of optoelectronic devices based on organic materials depends on the value of the unique properties of organics to the application in question. For example, amorphous organics can achieve efficient light emission that is tunable across the visible spectrum. This gives OLED displays a large advantage over their inorganic counterparts because of the relative ease of patterning amorphous rather than crystaline materials into active pixels. This has led to the commercial success of OLED display technology, which is widely viewed as superior to liquid crystal display (LCD) technology. The true inorganic analogue to OLED display, dubbed microLED, is still in development due to the high cost and difficulty of pixel transfer processes.

Despite the successful commercialization of OLEDs, there remain some key areas of research for their improvement. These include efficient light outcoupling, high power efficiency, and reliability. Outcoupling refers to extracting light from the high-index organic materials into the air where it is viewed. Power efficiency requires maximizing the efficiency with which electrical current is converted into light power, and minimizing the operating voltage to near the thermodynamic limit. Finally, improving reliability requires understanding the active degradation mechanisms in device structures. The reliability of blue emitting OLEDs is particularly challenging due to the high energy excitation required to reach the blue end of the spectrum. The first half of this thesis addresses advances in OLED technology, with emphasis on understanding the relationship between charge and exciton dynamics and the reliability of blue OLEDs.

In addition to enabling useful optoelectronic devices, there is rich science to explore in the field of organic electronics. Often, improving our understanding of phenomena observed in organic semiconductor systems in turn enables new applications. The second part of this thesis focuses on one such phenomenon, long range lateral charge transport in organic heterostructures, and its application to organic charge-coupled devices (CCDs).

1.1 Introduction to small molecule organic semiconductors

1.1.1 Organic small molecules

Molecules containing carbon-hydrogen bonds are classified as organic. Small molecules have low molecular weight and are typically less than 900 atomic mass units. Organic molecules used in optoelectronic applications are held together by covalent bonds and often are assembled by joining several organic groups together. Some examples of these organic groups are shown in Fig. 1.1. It is understood that

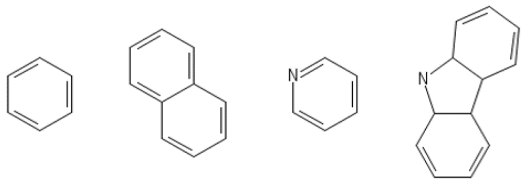

Figure 1.1: **Common simple organic small molecules.** Molecular structures from left to right are: benzene (phenyl), napthalene, pyridine, and carbazole. Verticies represent the positions of carbon atoms. Hydrogen atoms at the exterior positions are omitted.

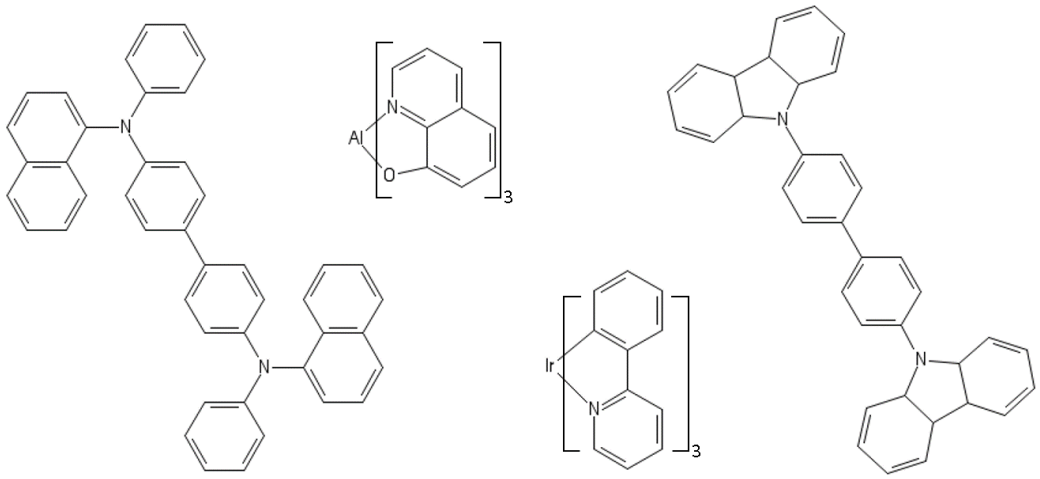

Figure 1.2: **Example molecules used in OLED applications.** From left to right: NPD, Alq_3, $Ir(ppy)_3$, and CBP.

the hydrogen atoms (not drawn for simplicity) are absent at the bond positions when these molecules are incorporated into larger organic molecules. Some examples of commonly used organic molecules for OLED applications that contain these groups are given in Fig. 1.2.

Importantly, conjugated organic molecules contain delocalized pi bonds. For example, three of the four valence electrons of a carbon atom can form single (or sigma) bonds to each of the three nearest neighbor atoms. The remaining valence electron resides in a barbell shaped orbital oriented perpendicular to the plane of the atoms in the molecule. The overlap of these out-of-plane orbitals form pi bonds, that are a

result of double bonds between carbon atoms. A classic demonstration of this bonding structure is benzene (see Fig. 1.1). Due to the symmetry of the molecule, the pi bonds are delocalized over the ring. This forms a conjugation system, or system of connected, delocalized pi bonds. Electrons can move freely along the conjugation system (intramolecular conduction), while the overlap of pi bonds between adjacent molecules also allows for intermolecular conduction.

While organic molecules are held together by covalent bonds, they typically have closed outer shells and thus do not chemically bond with each other. Rather, organic solids are made of molecules held together by van der Waals bonds that result from dipole interactions between molecules. van der Waals bonds are much weaker ($\sim$meV) than covalent bonds ($\sim$eV). Having strong intramolecular bonds but weak intermolecular bonds gives rise to many of the properties unique to organic solids.

1.1.2 Energy levels of organic semiconductors

Weak van der Waals bonds lead to poor electronic coupling between organic molecules. Organic semiconductors therefore only rarely exhibit band like transport, and then only for highly purified, well-ordered crystals. It follows that amorphous organics do not have the familiar valence and conduction bands like inorganic semiconductors, rather they have molecular energy levels. The energy levels of primary interest are the highest occupied molecular orbital (HOMO) and lowest unoccupied molecular orbital (LUMO) levels. As their names suggest, these correspond to the highest energy level occupied by the electrons of the neutral molecule and the lowest energy unoccupied level. These energies are typically specified in units of electron volts, referenced to the vacuum level, as shown in Fig. 1.3. Particles tend to relax to the lowest energy state available to them. For electrons, energetically preferred states are in the negative direction compared to vacuum (down), while for holes, which are simply the absence of an electron, energetically preferred states are in the positive

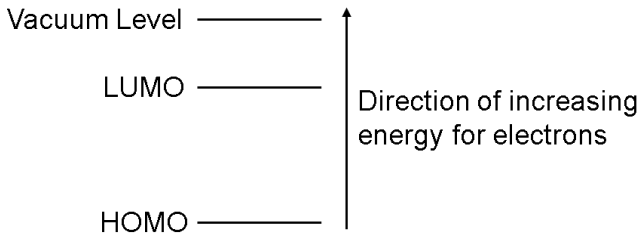

Figure 1.3: **Organic molecule frontier orbitals.** Orbitals are measured from the vacuum level. HOMO levels are filled in the ground state, while LUMO levels are not. The HOMO and LUMO are analogous to the valence and conduction bands of inorganic semiconductors, respectively.

direction (up). The HOMO is analogous to the valence band: its states are fully occupied by electrons until an electron is promoted to the LUMO or a hole is injected. Similarly, the LUMO is analogous to the conduction band.

There are a variety of methods for determining HOMO and LUMO energies. These include density functional theory (DFT) calculations and cyclic voltometry, as well as ultraviolet photoelectron spectroscopy (UPS) for HOMO energies and inverse photoelectron spectroscopy (IPES) for LUMO energies. Additionally, the LUMO is often estimated as the HOMO level plus the optical gap (or emission energy), however this often significantly underestimates the HOMO-LUMO gap because it does not account for relaxation of excited states before emission. Of these methods, UPS amd IPES are the most reliable because they are direct measurement methods of the material in solid state. UPS involves irradiating a sample with high energy photons, which ionizes the organic molecules by promoting electrons from the HOMO into vacuum. If a monochromatic illumination source is used, the difference between the photon energy and the maximum measured electron energy can be used to deduce the HOMO level. IPES is the reverse process, where the organic material is bombarded with electrons. As the electrons relax from near the vacuum level to the LUMO of the molecules, photons are emitted with energies corresponding to the difference between the energy levels.

1.1.3 Charge transport

The electric field from electrons and holes polarizes the molecules surrounding the charges. This screens the electric field from more distant locations and energetically stabilizes the charges. Together, the charges and their associated relaxation are referred to as polarons. Because organic molecules have weak intermolecular bonds and therefore electronic coupling, charges tend to be localized onto single molecules, and the transport of polarons occurs in discrete molecule-to-molecule steps, called 'hopping' transport. The coupling between molecules improves as the overlap between their pi orbital systems increases. However, because the polarization of the surrounding medium is centered on the electron, the polaron carries with it a small potential well. The result is that the polaron is 'sticky,' i.e, it takes energy to instigate a hop over the barrier at the edge of the potential. This situation is shown schematically in Fig. 1.4.

The two parabolas represent the potential surface for an electron on two adjacent molecules. To hop from one to the other, the electron must overcome the rise in potential between the two potential minima. This barrier increases as the energy of the destination site increases relative to its origin. The hopping rate, as described by Marcus theory, relates to the energy offset via $k_{transfer} \propto exp[-E_B/k_BT)]$, where the energy barrier $E_B = (\lambda - G_0)^2/(4\lambda)$. Here, λ is the height of origin potential at the position of the destination potential, and G_0 is the difference in potential minima. Because organics are disordered, there is variation in the energy of each site even for similar molecules due to local variations in molecular orientation and position. Thus, the microscopic details of hopping transport are complex and usually inaccessible experimentally. To understand bulk charge transport properties, it is useful to define bulk properties that describe the average behavior of charges in the solid.

Because applying an electric field makes it energetically favorable for charges to hop in the direction of the field, it results in the net flow of charges. The mobility, μ,

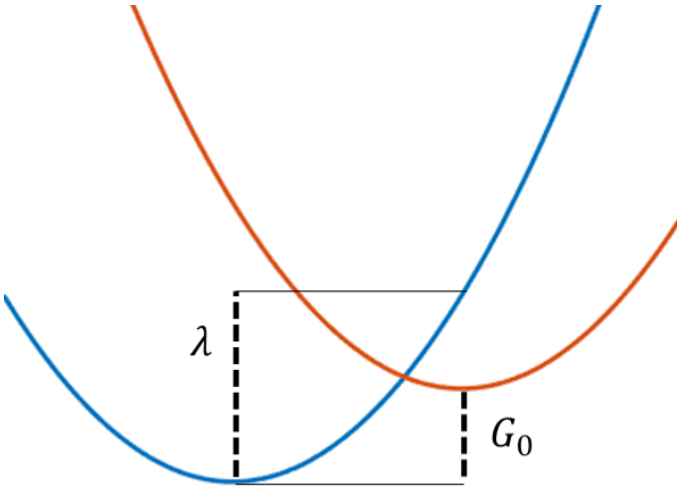

Figure 1.4: **Potential surfaces for hopping transport.** The two parabolas represent the potential of a charge as it moves between two adjacent molecules.

describes how fast the charges move in response to an applied field via the definition $v = \mu F$, where v is the velocity of the charges and F is the magnitude of the electric field. The drift current is $J_{dr} = \mu F n$, where n is the carrier density. Additionally, charges undergo random, thermally driven hopping motion, called diffusion. Because the diffusion is random, there is a net carrier flux from areas of high charge concentration to areas with low concentration. There is no driving force pushing charges towards areas of low concentration, rather it arises from purely statistical considerations. Quantitatively, the diffusion current is $J_{di} = D\frac{dn}{dx}$, where D is the diffusivity. In general, the mobility and diffusivity are different for electrons and holes. The time evolution of a distribution of charges modeled with drift diffusion can then be described by the partial differential equation:

$$\frac{d}{dt}n(x,t) = \nabla(D(x)\nabla n(x,t)) - \nabla(\mu(x)n(x,t)F(x,t)) \tag{1.1}$$

together with appropriate boundary conditions.

In many cases the drift-diffusion model is too ideal to adequately describe the behavior of charges in organic semiconductors, and other effects must be considered.

For example, it does not consider the energy barrier between transport sites due to disorder and lattice polarization. Because hopping transport is often thermally activated, the transfer rate to a molecule with higher energy than the original position is decreased. Barrier reduction can be described using Poole-Frenkel theory via the field-dependent mobility function $\mu = \mu_0 exp(-\sqrt{F})$.

1.1.4 Excited states of organic semiconductors

Excited states are formed when an electron is promoted to a higher lying energy level, for example the LUMO. This is commonly done by photon absorption or by electrical excitation via injection of carriers at conductive contacts. The electron in the higher lying state is still Coloumbically bound to the positive counter-charge of the net-neutral molecule. The bound excited state is called an exciton. The binding energy and how it changes with the distance between charges as well as the dielectric constant can be understood by the Bohr model which describes the classical energy of electron orbits. The Bohr model energy is $E = \frac{e^2}{8\pi\epsilon r}$, where e is the electron charge, ϵ is the dielectric constant, and r is the distance between the charges. The binding energy is reduced in high dielectric constant media. This effect is pronounced for inorganic semiconductors ($\epsilon \gtrsim 10$). The binding energy is also reduced because the effective mass of the charges is small, leading to larger orbitals and average distance between carriers. Excitons in inorganic semiconductors therefore have smaller binding energies that are easily overcome by thermal energy at room temperature. The excitons readily dissociate into free carriers.

This type of exciton, i.e, delocalized and weakly bound, are called Wannier-Mott excitons. Organic semiconductors, on the other hand, typically have a lower dielectric constant (≈ 3). Thus the exciton binding energy is high compared to the thermal energy. Tightly bound, localized excitons are called Frenkel excitons.

1.1.4.1 Single and Triplet Excitons

The Pauli exclusion principle states that no two identical Fermions can occupy the same state on a single molecule, i.e, they must differ by at least one quantum number. This can be shown to be equivalent to requiring that the total wave function of electrons in a molecule or atom be antisymmetric under particle exchange. Because most organic molecules in the ground state have full outer shells, each electron is paired with an electron that differs only in spin, leading to zero net spin. Zero-spin two-electron states are called singlet states because there is only one such state, i.e, $\frac{1}{\sqrt{2}}(|\uparrow\downarrow\rangle - |\downarrow\uparrow\rangle)$, which is antisymmetric under particle exchange. To satisfy the Pauli exclusion principle, the spatial component of the wavefunction must be symmetric under exchange.

If two electrons differ in, for example, the principle quantum number, three spin wavefunctions with total spin of 1 are possible in addition to the singlet state mentioned above. These are: $\frac{1}{\sqrt{2}}(|\uparrow\downarrow\rangle + |\downarrow\uparrow\rangle)$, $|\uparrow\uparrow\rangle$, and $|\downarrow\downarrow\rangle$, each of which is symmetric under particle exchange. These are called triplet states. To satisfy the Pauli exclusion principle, the spatial portion of a triplet state wavefunction must be antisymmetric with respect to exchange, opposite the spatial symmetry of singlets. This has important consequences for photon emission, because radiative transitions cannot couple wavefunctions with opposite particle exchange symmetries in the spatial wavefunction. Thus, excited state and ground state singlets are coupled via absorption and emission, but the ground state singlet can't be optically excited to a triplet state, nor a triplet state radiatively relax into the ground state.

Emission from excited singlet states is called fluorescence, and typically has a radiative rate $\sim 10^9$ s^{-1}. Phosphorescence, which refers to emission from excited triplet states, would not be possible without mixing singlet and triplet states. Perturbations to the potential, such as spin-orbit coupling, cause some state mixing. This means that triplet states acquire some singlet character, causing absorption and emission

to become weakly allowed. For organic molecules composed entirely of light atoms such as pure hydrocarbons, the resulting radiative rate is slow, typically $10^0 - 10^3$ s^{-1}. However, the magnitude of spin-orbit coupling scales as the atomic number to the fourth power. Thus incorporating heavy elements, such as Ir and Pt, can dramatically increase the radiative rate, with some phosphorescent compounds reaching $\sim 10^6$ s^{-1}. Before they relax due to radiative or nonradiative processes, excitons may diffuse in the organic material.

While photon absorption primarily results in singlet excitons, both singlets and triplets can be stimulated by current injection. Because the spins of injected carriers are uncorrelated, electrical excitation is statistically expected to yield one singlet for every three triplets, following the multiplicity of the states[1]. Thus, the theoretical maximum internal quantum efficiency (IQE) of fluorescent devices is expected to be $\sim 25\%$ (not considering annihilation effects, which are discussed later). In a phosphorescent device, the maximum attainable IQE reaches 100%[2].

1.1.5 Energy transfer and exciton diffusion

Exciton diffusion occurs primarily by Förster[3] or Dexter[4] energy transfer. Förster transfer (often referred to as Förster resonance energy transfer, or FRET) is a nonradiative process by which excitons are transferred between molecules through dipole-dipole interactions. Because dipole field strength varies as r^{-3} and Förster transfer results from the interaction of two dipoles, Förster transfer rate scales as r^{-6}. Specifically, the transfer efficiency is $\frac{1}{1+(r/r_0)^6}$, where r_0 is the Förster radius, or 50 percent transfer efficiency distance. The Förster radius is calculated as

$$r_0^6 = \frac{9\kappa^2\Phi}{128\pi^5 n^4} \int \phi(\lambda)\sigma(\lambda)\lambda^4 d\lambda. \tag{1.2}$$

Here, κ^2 is the dipole orientation factor, Φ is the quantum yield of the donor, n is the index of refraction, ϕ is the emission spectrum (normalized to area), and σ is

the attenuation cross section of the acceptor. For isotropic dipole orientation, $\kappa = 2/3$. Thus, Förster transfer becomes more efficient over smaller distances and with increased overlap of the absorption and emission spectra of the molecules. Typical Förster radii are less than 10 nm. The same selection rules that disallow triplet absorption and emission also disallow Förster transfer, however it is accessible by triplets on phosphorescent molecules due to singlet state mixing, and between two excited triplet states.

Dexter transfer, in contrast, results from the coincident hopping of electrons between neighboring excited and ground state molecules. As such, it is shorter range than Förster transfer. The Dexter transfer rate depends on the overlap of emission and absorption spectra, the distance between sites, and the details of the wavefunctions and exchange Hamiltonian[4]. The rate scales approximately with separation as

$$k_{dexter} \propto Jexp(\frac{-2r}{L}), \tag{1.3}$$

where J is the overlap integral of the emission spectrum of the donor with the absorption spectrum of the acceptor, r is the distance between donor and acceptor, and L is an effective average radius of the excited and ground states involved. Dexter transfer is not restricted by dipole transition selection rules. It only requires that spin be conserved during transfer. Thus, triplet states are free to transfer via the Dexter mechanism to adjacent ground state singlet molecules.

These mechanisms are represented schematically in Fig. 1.5. Triplet Förster transfer and singlet Dexter transfer are also possible, but tend to be dominated by triplet Dexter transfer and singlet Förster transfer, respectively.

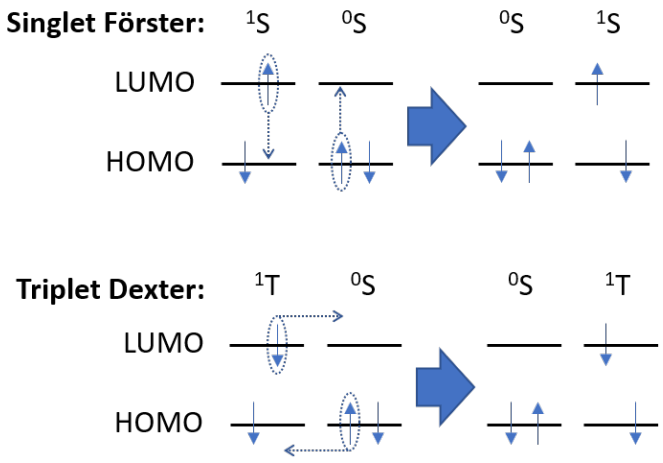

Figure 1.5: **Exciton transfer mechanisms.** (Top) Schematic representation of singlet-singlet Förster transfer. (Bottom) Schematic representation of triplet-singlet Dexter transfer. ^1S is the first (lowest energy) singlet excited state, ^0S is the ground singlet state, and ^1T is the first triplet state.

1.1.6 Bimolecular annihilation reactions

At high excitation densities, there can be annihilation reactions caused by excited state reactions. The most common of these in phosphorescent devices involve triplets, primarily triplet-triplet annihilation (TTA) and triplet-polaron annihilation (TPA). In fluorescent devices, including organic lasers, singlet-triplet annihilation (STA) plays an important role.

TTA occurs when triplet excitons interact, possibly by diffusing to the same molecule. This results in the relaxation of one exciton and further excitation of the other, creating a hot state. This is followed by rapid thermalization of the hot excited state to the first excited state. An example of a TTA reaction is

$$T_1 + T_1 \rightarrow S_n + S_0 \rightarrow S_1 + S_0 \tag{1.4}$$

where ^1T is the first (lowest energy) triplet excited state, S_n is a multiply excited singlet state, S_1 is the first singlet state, and S_0 is the ground state. TPA proceeds similarly, with a polaron and triplet reacting, resulting in a ground state molecule

and a hot polaron that quickly relaxes back down to the transport level. Because they result in the net loss of an exciton, these annihilation reactions are a channel for energy and efficiency loss. The annihilation rate increases with the excitation density as $k_{TT}T^2$ and $k_{TP}nT$ for TTA and TPA, respectively, where k_{TT} and k_{TP} are rate constants, T is the triplet density, and n is the polaron density. The rate constants are proportional to the sum of the diffusivities of the participating particles, i.e, annihilation is more severe for larger diffusivities. As they are quadratic in the particle densities, these effects are most pronounced at high intensity. This causes efficiency roll-off in phosphorescent OLEDs[5] as well as accelerating intrinsic degradation in blue phosphorescent organic light emitting devices (PHOLEDs)[6] due to resultant hot states causing bond rupture of the molecules.

1.2 Basics of organic light emitting devices

In its simplest form, an OLED comprises a single layer of organic material sandwiched between two contacts. When the contacts are biased, electrical carriers are injected, holes from the anode and electrons from the cathode. These can recombine in the organic layer, forming excitons which may emit light. If one or more of the electrodes is transparent, some of the generated light will be emitted out of the device. This is shown schematically in Fig. 1.6a. Of course, it is often desirable to add multiple functional layers to improve device operating characteristics, some of which are described in Fig. 1.6b. Top and bottom emitting schemes are shown in Fig. 1.6c-d. Fully transparent structures are also possible. Layers are often grown with the anode closest to the substrate, however the electrode polarities and organic stack structure may also be inverted.

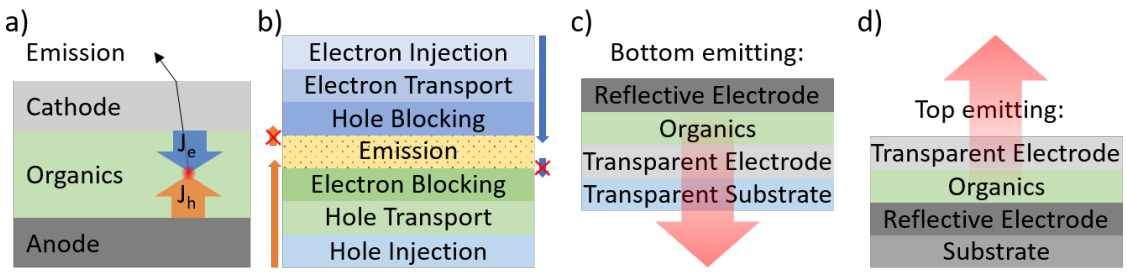

Figure 1.6: **OLED structures.** a) Simple schematic of an OLED, showing the electron and hole currents J_e and J_h, respectively. b) A detailed hypothetical layer structure, with layers labeled by function. Injection layers reduce barriers at the organic-electrode interfaces to facilitate injection. Blocking layers prevent carriers leaving the emission layer. The emission layer is where exciton formation and light emission occurs. Dots represent luminescent chromophores, which are commonly doped into a wide energy gap host matrix. c) Bottom emitting device scheme. d) Top emitting device scheme.

1.2.1 OLED performance metrics

There are several common metrics of OLED performance. The external quantum efficiency (EQE) is the ratio of photons emitted into the air to charges injected from the electrodes. It can be broken into constituent efficiencies:

$$\eta_{EQE} = \eta_{OC} \times \eta_{CB} \times \eta_{EC} \times \eta_{ET} \times \eta_{QY} \times \eta_{EU}. \tag{1.5}$$

Here, η_{OC} is the outcoupling efficiency, i.e, fraction of extracted to generated photons; η_{CB} is the charge balance efficiency, i.e, the fraction of injected charge carriers that recombines in the emission layer; η_{EC} is the exciton confinement efficiency, i.e, the fraction of excitons generated that do not diffuse out of the emission layer before relaxing; η_{ET} is the energy transfer efficiency, i.e, the fraction of excitons that are generated on or are transferred to a luminescent chromophore; η_{QY} is the quantum yield, i.e, the probability of photon emission per emissive exciton on the chromophore; and η_{EU} is the exciton utilization efficiency, i.e, the fraction of emissive excitons. For flu-

orescent devices, η_{EU} is the singlet yield. Bottom emitting devices using a top metal cathode and glass substrate (index ∼1.5) have a maximum outcoupling efficiency of about 20%[7], which can be enhanced significantly by employing light-extraction structures[8–11]. For well-designed devices, near unity η_{CB} and η_{EC} are achievable. This largely depends on the energetics of the confinement layers and position of the exciton formation zone, which is determined by the details of carrier transport. For appropriate doping concentrations employing a host-dopant pair with efficient host-to-guest energy transfer (by Förster or Dexter mechanisms), η_{ET} can also approach unity. The quantum yield is a property of the chromophore, arising from details of its chemical structure. Finally, η_{EU} is often considered to be 0.25 for fluorescent devices due to the singlet yield, however this neglects TTA and other sources of delayed emission such as back transfer from singlet to triplet states. For phosphorescent devices, $\eta_{EU} = 1$. Removing η_{OC} from the right hand side of Eq. 1.5 yields the IQE.

Power conversion efficiency, η_{PCE}, is the ratio of optical output power to electrical input power, which is 100% if the device operating voltage corresponded to the photon energy (in eV) and $EQE = 100\%$. In practice, this is difficult to achieve even for devices with IQE = 100% due to losses in outcoupling as well as resistive losses and relaxation of the exciton, causing the emission energy to be less than the HOMO-LUMO gap. For a green bottom emitting device with no outcoupling scheme, 100% IQE, and operating voltage of 7 V (∼3× the photon energy), $\eta_{PCE} \approx 6\%$.

Additional efficiency metrics that are important for evaluating devices intended for display or illumination require an understanding of human color perception. Standards for human color and luminosity perception were defined in 1931 by the International Commission on Illumination based on the experiments of Wright and Guild[12,13]. The standards are based on the response functions of the three types of cone cells that our eyes use to distinguish color, known as the color matching functions. The three color matching functions are plotted in Fig. 1.7.

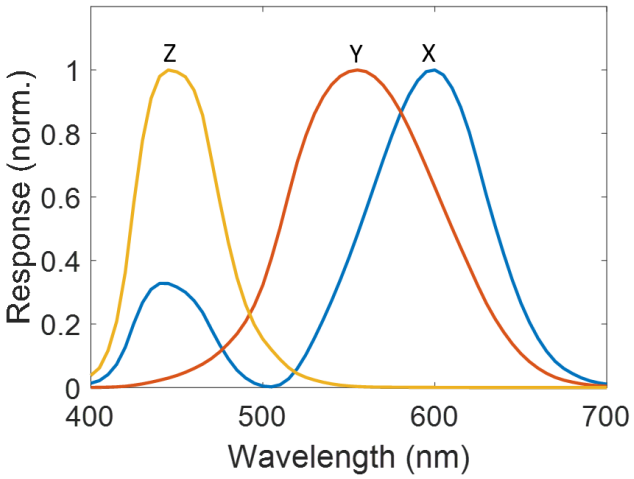

Figure 1.7: **CIE 1931 color matching functions.**

The Y color matching function, which peaks at 555 nm, is also known as the photopic response curve, which describes how we perceive brightness. In this context it is defined to be 683 lumens per watt (lm/W) at its maximum. Thus, emission spectra with high intensity in the green appear brighter than spectra with equal optical intensity but centered in the red, blue, or outside of the visible spectrum. Quantitatively, the responsivity of the eye, Φ, to an arbitrary spectrum is

$$\Phi = 683 \int \phi(\lambda) Y(\lambda) d\lambda, \tag{1.6}$$

where $\phi(\lambda)$ is the input spectrum, normalized to unit area. We can now define the luminous power efficiency (LPE), which is simply $\eta_{LPE} = \Phi \eta_{PCE}$, and describes the luminous flux output per unit power input.

Another quantity of interest, especially for describing a display, is the luminance, measured in cd/m^2. Luminance describes the luminous intensity per area as observed from a given direction, which is a measure of the apparent brightness of the source observed directly (as opposed to luminous flux, which is a measure of the total illumination output of a source). Quantitatively, luminance is

$$L_V = \frac{d^2\Phi_L(\theta)}{dAd\Omega cos(\theta)}, \tag{1.7}$$

where $\Phi_L(\theta)$ is the luminous flux emitted from area dA into solid angle $d\Omega$, and θ is the angle between surface normal and the emission direction. For a lambertian emitter radiating into a 2π sr half-space, i.e, the special case for which $\Phi_L(\theta) = \Phi_{L,max}cos(\theta)$, the luminance is constant and is related to the luminous flux per area by 1 cd/m^2 = π lm/m^2. Yet another performance metric, primarily used for displays, is the luminance current efficiency, measured in cd/A.

The color matching functions in Fig. 1.7 are used to quantify the color of a spectrum. First, the spectrum is integrated against the three color matching functions to obtain $\bar{X}$, $\bar{Y}$, and $\bar{Z}$:

$$\bar{X} = \int \phi(\lambda)X(\lambda)d\lambda,$$

$$\bar{Y} = \int \phi(\lambda)Y(\lambda)d\lambda,$$

$$\bar{Z} = \int \phi(\lambda)Z(\lambda)d\lambda.$$

The CIE color coordinates are then calculated as:

$$\bar{x} = \frac{\bar{X}}{\bar{X}+\bar{Y}+\bar{Z}}, \bar{y} = \frac{\bar{Y}}{\bar{X}+\bar{Y}+\bar{Z}} \tag{1.8}$$

with the pair $(\bar{x}, \bar{y})$ indicating the color coordinate on the 1931 CIE color chart, shown in Fig. 1.8.

For white light sources, the spectrum can be described by its correlated color temperature (CCT) and color rendering index (CRI). The CCT is the temperature of the black-body closest to the white light source on the CIE color space, determined

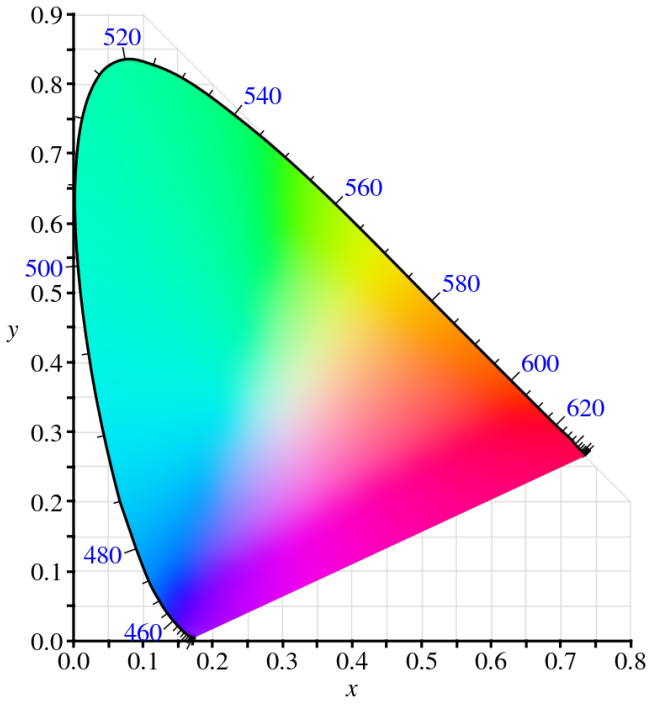

Figure 1.8: **CIE 1931 color space.** Blue numbers labeled around the colorspace indicate the wavelength in nm for monochromatic spectra.

by the intersection of the line perpendicular to the Plankian locus that also intersects the $(\bar{x}, \bar{y})$ coordinate of the light source. The CRI describes how similar the spectrum is to a black-body with the same CCT. It is calculated by averaging the difference between reflection spectra from a series of standard color samples when illuminated by the white light source versus the black-body reference spectrum[14].

1.2.2 Optics of OLEDs

The outcoupling efficiency as well as the angular intensity and spectral dependencies, are determined by the optical structure of the device. The optical power transport can be modeled by calculating the emission pattern from point dipoles located at the position of the excitons. For a conventional bottom emitting device employing a top metal electrode, there are several available modes into which the optical power will be coupled. These include air modes, substrate modes, waveguide modes, and

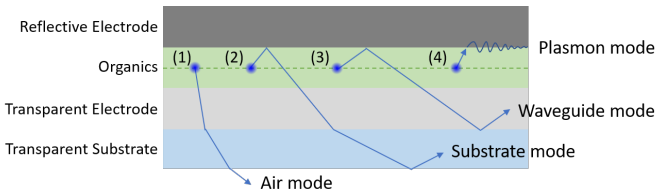

Figure 1.9: **Optical modes.** Optical modes in a bottom emitting device. (1) An air mode, for which light couples out of the device. Optical structures are designed with the goal of maximizing coupling or scatting into these modes. (2) A substrate mode. Light coupled to substrate modes are trapped by TIR at the substrate-air interface. (3) A waveguide mode, where light is confined to the high-index organic and anode layers. (4) A plasmon mode. Coupling to plasmon modes requires the emitter be in the near-field, allowing excitation of lossy charge oscillations at the surface of the metal. This diagram is illustrative only, as ray optics are not appropriate to describe propagation in all of these modes.

plasmon modes at the metal cathode surface. These are shown schematically in Fig. 1.9.

Because the electric field must vanish at the metal surface (or near it, considering skin depth), there is a node in the electric field there. Outcoupling is improved when the dipole is positioned near to the antinode, where the field strength is maximum. The antinode is at $\lambda_0/(4n)$, where λ_0 is the freespace wavelength of the light and n is the index of refraction of the organic material, thus the optimal spacing of the emission layer (EML) from the metal electrode is larger for longer wavelengths of light. While this is a useful rule of thumb, the details of modal power coupling in the OLED structure are best calculated using computational simulations, such as by a Green's function method[7].

1.2.3 OLED characterization

Accurate OLED characterization is important for reliably comparing data across multiple experiments and laboratories. To accomplish this, standards for measurement and calculation of OLED efficiency have been established[15]. Importantly, using a large area photodetector to capture all the light coming out the face of the device

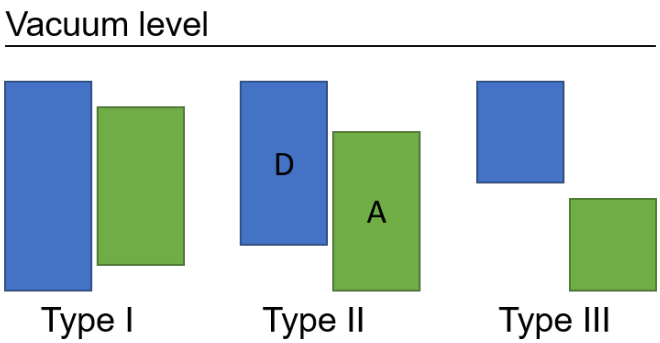

Figure 1.10: **Types of organic heterojunctions.** From left to right, type I, II, and III heterojunctions. In a type II heterojunction, the material with the shallower LUMO is called the acceptor (labeled A), and other is called the donor (labeled D).

allows accurate determination of the optical power output. One consideration while performing this measurement is the angular and polarization dependence of the detector that is used, as calibration data is usually only given for normal incidence. Bottom-emitting devices optimized for outcoupling have weak microcavities. The output is close to lambertian and only weakly polarized at high angles. For a silicon detector, the expected error from neglecting the angular dependence of the detector responsivity is small ($\sim$1%), however for strong cavities these effects need to be considered to avoid significant errors.

1.3 Organic heterojunctions

A heterojunction (HJ) is the interface between two dissimilar materials. Organic-organic HJs and metal-organic HJs both play an important role in the operation of organic photoactive devices, such as OPV and organic photodectectors.

1.3.1 Types of organic heterojunctions

Semiconductor HJs are divided into three types based on their energy level alignment. For organic materials, this refers to the energy gap and the relative positions

of the HOMO / LUMO values. The three types of HJ are shown in Fig. 1.10. For a Type I HJs, the HOMO and LUMO of one material lie within the energy gap of the other. This results in blocking behavior for charges and excitons on the smaller energy gap material and exothermic transfer across the HJ for those on the wide energy gap material. Type II HJs have staggered energy gaps, such that transfer across the interface is exothermic for holes in one direction and for electrons in the opposite direction, and can facilitate charge separation of excitons. The materials in a type II HJ are called donors and acceptors, according to the direction of electron transfer, i.e, the material with the deeper LUMO is the acceptor. Type III HJs involve materials without any overlap in the energy gaps.

The energy levels of the individual materials may shift from their bulk values at the HJ due to the formation of interface dipoles, charge transfer, polarization, or dielectric effects[16]. The energy shifts can be investigated using UPS and IPES on a series of samples where the second material is added to the first in thin layers ($\sim$1 monolayer thick at a time). The energy of emission due to charge recombination across the HJ can also be used to determine the donor HOMO-acceptor LUMO offset.

1.4 Charge photogeneration in organic heterojunctions

In photovoltaic and photodetector devices, absorbed light is converted to electrical signal. Excitons generated by photon absorption can dissociate at HJ interfaces between donor and acceptor molecules. Intermixing donor and acceptor molecules in bulk heterojunctions can reduce the distance that excitons must diffuse to reach a HJ interface to single molecule or nanometer-scale domain lengths. If the energy difference between the donor HOMO and acceptor LUMO is less than the exciton energy of the single molecules, there is a driving force for charge separation across the interface. One of the charges in the electron-hole pair that makes up the exciton may transfer across the HJ. This excited state, which is shared across two molecules,

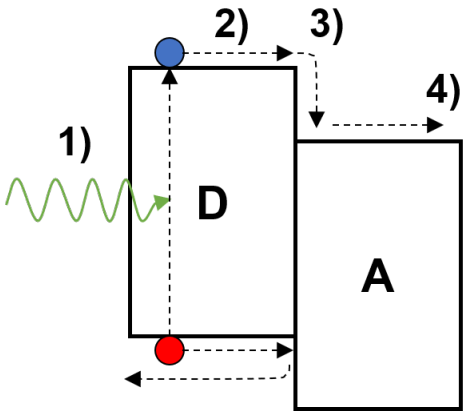

Figure 1.11: **Charge generation steps.** 1) An incident photon is absorbed either in the donor (D) or acceptor (A), resulting in an exciton. 2) The exciton diffuses to a HJ interface. 3) The excition transfers to a charge-transfer state, with the electron on the acceptor. 4) The charge transfer state dissociates into free charges, which can be collected at electrodes.

is called a charge transfer state. When the charge transfer state dissociates, free charge is generated that can then be extracted from the device at the electrodes. The steps of the charge generation process are shown in 1.11.

The efficiency of charge photogeneration, η_{CG}, is simply the product of the constituent step efficiencies:

$$\eta_{CG} = \eta_A \times \eta_{ED} \times \eta_{CT} \times \eta_{CC},$$

where η_A is the light absorption efficiency, η_{ED} is the exciton diffusion efficiency, η_{CT} is the charge transfer efficiency, and η_{CC} is the charge collection efficiency. Light absorption is affected by light incoupling, the optical field in the thin-film structure, layer thickness, parasitic absorption outside the HJ, and the overlap between the absorption spectrum of the HJ and illumination source[17]. The diffusion efficiency depends critically on the exciton diffusion length and the average distance of absorption sites from a HJ interface. Using a bulk (i.e, mixed) HJ allows the use of thicker layers without decreasing η_{ED}. Charge transfer efficiency is influenced by the energy offset at the HJ and wavefunction overlap. Recent work has focused on minimizing the

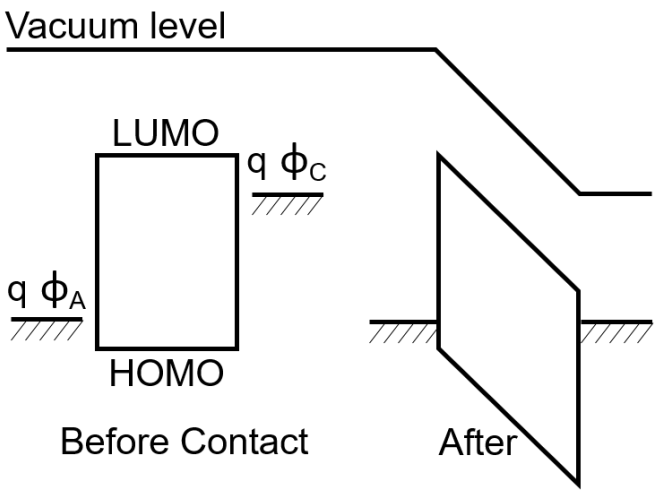

Figure 1.12: **Built-in field.** (left) Energy levels of the organic and ionization potentials of the anode and cathode relative to vacuum. (right) After contact at zero bias, there is a uniform potential drop across the organic layer, resulting in a built-in field.

energy offset while maintaining high η_{ED} to increase power generation in OPVs[18]. Charge collection efficiency results from the competition between collection and recombination rates. Charge collection can be assisted by the presence of a built-in field that results from a mismatch in electrode work functions, as shown in Fig. 1.12. Here, the anode and cathode work functions, $q\phi_A$ and $q\phi_C$, respectively, are offset. After making contact at the interfaces and placing the device in a short-circuit condition, the electrode potentials must be equal. Treating the organic layer as a charge-neutral insulator, a uniform potential drop forms across the organic layer, equal to the work function offset. This results in a built-in field of magnitude $F_{BI} = q(\phi_C - \phi_A)/d$, where d is the thickness of the organic layer.

1.5 Organic photodetector structures

Organic photodectors typically consist of a transparent electrode, buffer layers, one or more HJ layers, and a reflective electrode, as shown in Fig. 1.13. Buffer layer materials are chosen to give selective charge collection at the electrodes (holes on one

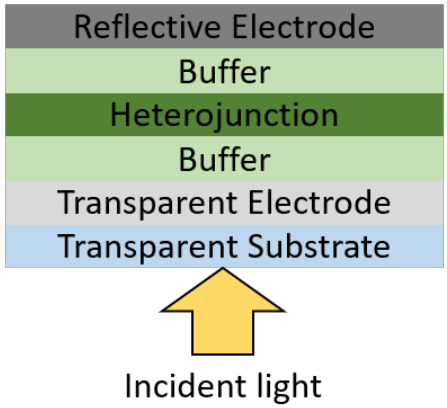

Figure 1.13: **Organic photodetector structure.** The heterojunction region is separated from the elctrodes by buffer layers. One of the electrodes is transparent, the other reflective. A substrate-side illumination device is shown, but the device layer structure could also be inverted.

side, electrons on the other) as well as to prevent exciton quenching at the electrode interfaces. The HJ region may comprise a planar junction between neat donor and acceptor layers, a bulk HJ, or some combination of the two.

1.6 Photodetector current-voltage characteristics

Organic photodetector current-voltage characteristics are qualitatively similar to inorganic PV and photodiodes. An example following the ideal diode equation, $I = I_S(\exp qV/kT - 1) - I_{Ph}$, is plotted in Fig. 1.14. Here, I_S is the reverse bias saturation current, q is the electron charge, kT is the thermal energy, and I_{Ph} is the photocurrent. The open circuit voltage, V_{OC}, and short circuit current, J_{SC}, are also shown. The red shaded region has an area of $V_{OC} \times J_{SC}$. The blue shaded area intersects the current-voltage characteristic under illumination at the maximum power point. The ratio of the blue to red regions is defined as the fill factor (FF). For OPVs, the power conversion efficiency can be calculated simply as $(J_{SC} \times V_{OC} \times FF)/P_{incident}$, where $P_{incident}$ is the incident power. The ideal diode equation for organic heterojunctions has been shown to take the same functional form as inorganic diodes, albeit with

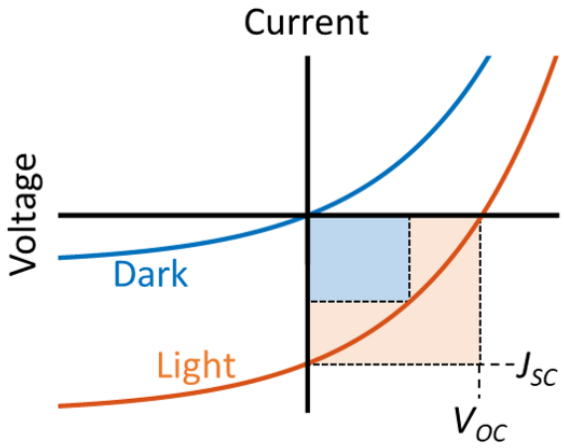

Figure 1.14: **Organic photodetector current voltage characteristic.**

different physical underpinnings[19,20].

CHAPTER II

Determining polaron and exciton distributions in organic light emitting devices

An important part of the success of PHOLEDs in the display industry has been achieving near unity IQE through control of charge balance and exciton confinement[21–25]. These are still challenging issues for long lived blue PHOLEDs due to the energy levels required of blocking materials to confine energy to the already large gap blue host and guest layers[21–24]. As discussed in Ch. 1, the efficiency of OLED devices is directly proportional to η_{CB} and η_{EC}. However, it is difficult to determine these factors in a device. A device which maximizes its theoretical *EQE* may be assumed to have near unity η_{CB} and η_{EC}, but even in these cases the role of exciton and charge confinement - and the potential loss thereof - in the roll-off of efficiency at high brightness is uncertain. In some cases unintended emission due to fluorescence of the transport or blocking layers indicates poor charge confinement, but the absence of unintended emission does not guarantee that $\eta_{CB} \approx \eta_{EC} \approx 1$. In this chapter a method for directly measuring η_{CB} and η_{EC} is introduced. The method involves doping thin sensitizing layers into the EML and its surrounding layers, and monitoring the sensitizer emission. In addition, a model is derived that links material properties to the blocking performance and the charge carrier and exciton distributions. The

technique provides a powerful tool for understanding the performance and carrier distribution of a given device structure versus current density. The main conclusions of this chapter were published in *Advanced Optical Materials*[26].

2.1 Theory of charge and exciton distributions in a PHOLED

It is important to understand charge transport and the resulting exciton density distribution to determine an appropriate blocking layer material. Injected charges have three possible eventualities: first, recombination in the EML; second, recombination outside of the EML; or third, they traverse the full thickness of device and are collected at the opposing electrode. We can describe carrier transport using drift-diffusion and thermionic emission over energy barriers[25,27,28] (for example at blocking layer interfaces), using the equations:

$$J_n(x,t) = q\mu_n(x,t)F(x,t) - kT\mu_n(x,t)\frac{\delta}{\delta x}n(x,t), \tag{2.1}$$

$$\frac{d}{dx}F(x,t) = \frac{q}{\epsilon}[p(x,t) - n(x,t)] = -\frac{d^2}{dx^2}V(x,t), \tag{2.2}$$

$$\mu_n(x,t) = \mu_{0n}(x)exp\left(\sqrt{\frac{F(x,t)}{F_0}}\right) \times \begin{cases} exp(-\frac{\phi_p - \Delta\phi(t)}{kT}) & \phi_n > \Delta\phi \\ 1 & \phi_n < \Delta\phi \end{cases} \tag{2.3}$$

The hole current density, $J_p(x,t)$, is found using an equation analogous to Eq. 2.1. Here, $F(x,t)$ is the electric field at position x and time t, q is the elementary charge, k is Boltzmann's constant, T is the temperature, and ϵ is the dielectric constant of the material. Also, $J_n(x,t)$ is the electron current density, $\mu_n(x,t)$ is the electron mobility, $n(x,t)$ is the electron density, $p(x,t)$ is the hole density, F_0 is a reference electric field, ϕ is the frontier orbital energy difference across an interface, and $\Delta\phi(t) = F(t)d$ is

the potential difference across the interface of width d. The boundary conditions are $V(0) = V_a - V_{bi}$ and $V(L) = 0$, where V_a is the applied voltage, and V_{bi} is the built-in voltage. Here, $x = 0$ corresponds to the position at the anode side of the EML, and $x = L$ at the cathode. The Einstein relation is used to relate the mobility and diffusion constants. The mobility has a Poole-Frenkel type field dependence common to organics[29]. Charge balance is calculated from the solution to these equations, defined quantitatively as:

$$\eta_{CB} = \frac{J_p^{inj} - J_p^{leak} + J_n^{inj} - J_n^{leak}}{J_p^{inj} + J_n^{inj}} \tag{2.4}$$

where subscripts n and p denote the polarity of the current and superscripts denote if the current is injected into or leaking out of the EML.

Triplet excitons that are formed in the EML either relax there or diffuse into adjacent layers. Assuming Langevin recombination[28,30], the exciton formation rate is $\gamma(x,t)n(x,t)p(x,t)$, where $\gamma = q(\mu_n + \mu_p)/\epsilon$ is the Langevin rate constant. We approximate the diffusion of triplet excitons into the adjacent layers by assuming the the diffusivity $D = D_N$ at the boundary if the triplet energy of the adjacent layer is less than kT above the triplet energy in the EML and $D = 0$ otherwise. Thus, rate equations for the polaron and exciton densities are

$$\frac{d}{dt}n(x,t) = -\gamma(x,t)n(x,t)p(x,t) - \frac{d}{dx}J_n(x,t), \tag{2.5}$$

$$\frac{d}{dt}p(x,t) = -\gamma(x,t)n(x,t)p(x,t) - \frac{d}{dx}J_p(x,t), \tag{2.6}$$

$$\frac{d}{dt}N(x,t) = \gamma(x,t)n(x,t)p(x,t) - \frac{d}{dx}\left[D_N(x)\frac{d}{dx}N(x,t)\right]. \tag{2.7}$$

The spatial dependence of the mobility arises from the field dependence of the mobility, the interface behavior mentioned above, and most importantly the spatial dependence of the doping concentration in the EML. For triplet diffusion by the

Dexter transfer mechanism, the diffusivity varies with the transfer distance between dopant sites, a, as $D_N \propto a^2 exp\left(-\frac{2a}{L}\right)$, where $L = 1.6$ nm is the exciton Bohr radius for typical Ir based phosphors[31]. The spacing between dopant molecules is related to the doping concentration by $a = (CN_M)^{-1/3}$ where C is the doping concentration and $N_M \approx 10^{21}$ is the molecular density of the film. Equations 2.1-2.3 and 2.5-2.7 are solved using a finite difference method, with initial conditions $n(x,0) = p(x,0) = N(x,0) = 0$. The solution is continued until the system reaches steady state.

2.2 Method of sensitizers

Exciton formation regions have previously been mapped inside a device EML using luminescent[32,33], or quenching[25] sensitizers. The idea is to fabricate a series of devices, each having a thin sensitizing layer embedded at a different position within the device. The spectral intensity of the sensitizer is measured as a function of position to determine the local density of excitons at the location of the sensor. In this work, this concept is expanded by placing sensitizers outside the EML to monitor for leaked excitons or charge recombination in the transport and blocking layers. We employ ultrathin ($\leq$2 nm) sensor layers comprising a phosphor with lower emission energy than that of the dopant in the EML. This increases the signal due to energy transfer to the sensitizer as well as allows sensor emission to be wavelength resolved from dopant emission. The sensor should have a short dopant-sensor energy transfer distance, as this limits the spatial resolution of the sensing measurement. It is also desirable to avoid charge trapping on the sensor molecules to prevent incorporation of the sensing layers affecting charge transport in the device[25,32]. The sensing layers trap triplet excitons, giving red-shifted emission with intensity that is proportional to the local density of excitons. The flux of excitons into the sensor layer at position x can be calculated from the polaron and exciton densities as:

$$\Phi_E = \int_{x-r_c}^{x+r_c} \gamma(x')n(x')p(x')dx' + D_N \frac{\partial N}{\partial x}\bigg|_{x+r_c} - D_N \frac{\partial N}{\partial x}\bigg|_{x-r_c}, \tag{2.8}$$

where r_c is the transfer radius from the dopant to the sensor molecule. The integral accounts for all of the excitons formed directly in the region where emission is dominated by the sensor layer, and the last two terms account for diffusion into this region. The emission intensity is then calculated as $I_{sense}(x) = \Phi_E(x)\eta_{OC}(x)\eta_{QY}(x)E_{ph}$, where η_{OC} is the outcoupling efficiency, η_{QY} is the photoluminescence quantum yield (PLQY) of the sensor, and E_{ph} is the average photon energy emitted by the sensor.

2.3 Fabrication of devices for measurement of charge balance and exciton confinement

A series of devices, denoted A and B, were fabricated having 2 nm thick sensing layers doped with PQIr[32]. The device structure for both is 70 nm thick indium tin oxide (ITO) anode / 10 nm thick HATCN hole injection layer (HIL) / hole transport layer (HTL) / 50 nm thick EML / 5 nm thick mCBP hole and exciton blocking layer (hole blocking layer (HBL)) / 30 nm thick Alq_3 ETL / 1.5 nm thick Liq electron injection layer (electron injection layer (EIL)) / 100 nm thick Al cathode, as shown in Fig. 2.1. Here, the EML consists of the blue emitting 18 vol% $Ir(dmp)_3$ in mCBP at the anode side, linearly graded to 8 vol% at the cathode side. For device A, the HTL is comprised of a 20 nm thick NPD, and for device B, the HTL is a 15 nm thick NPD / 5 nm thick of CZSi mixed with Tris-PCz (3:1 by vol.) which also serves as an electron blocking layer (EBL). The layer thicknesses were measured by a quartz crystal microbalance with error of $\pm 5\%$.

In an effort to reduce errors due to growth-to-growth variation, an in-situ movable shadow mask is used such that each organic layer (except the sensing layers and HTL in devices A and B) is deposited simultaneously without breaking vacuum between

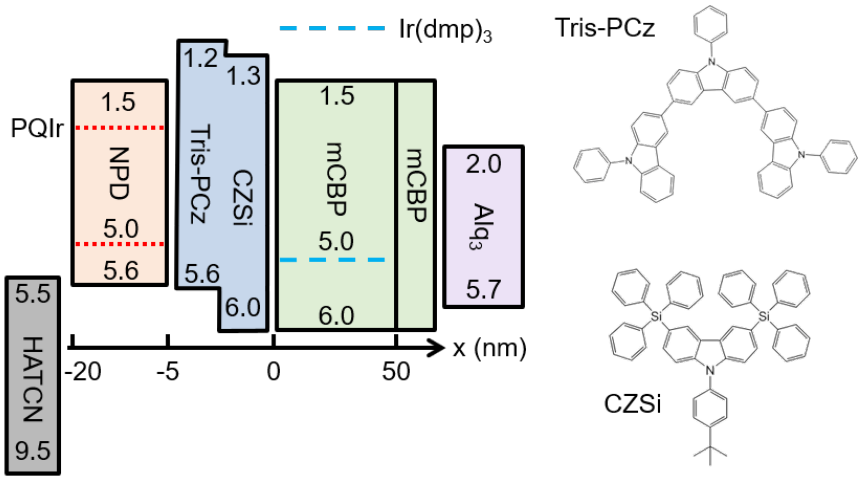

Figure 2.1: **Structure and energy diagram of PHOLEDs for confinement sensing.** Energy level diagram for the materials used in devices A and B. The HOMO and LUMO energies are labeled in eV. The energies for dopants $Ir(dmp)_3$ and PQIr are represented as dashed lines in mCBP and NPD, respectively. The 3:1 CZSi:Tris-PCz mixed layer used in device B are indicated. For device A, $x = -20$ to 0 nm is replaced by neat NPD. The scale bar shows the sensing layer positions. The LUMO energies of mCBP, Tris-PCz, and CZSi are from reduction potential measurements with error of ± 0.3 eV[34] and the remaining energies are from the literature[32,34–36]. The chemical structural formulae of electron and exciton blocking materials Tris-PCz and CZSi are also shown.

organic layers. The device area is 2.00 ± 0.03 mm^2 as defined by the intersection of the metal cathode and pre-patterned ITO anode strips. Following fabrication, the devices were encapsulated with glass cover slides sealed to the substrate with ultraviolet-cured epoxy in a N_2-filled glove box (< 1 ppm water and oxygen).

The sensing layers consist of an additional 2 nm thick layer of the same organics into which the sensor is inserted, doped at 3.0 ± 0.2 vol% with the red-emitting phosphor PQIr, i.e, if the sensor is placed in the electron transport layer (ETL), the sensing layer would be 2 nm NPD doped with 3 vol% PQIr. The sensing layers were placed at $x = -15.0$, -10.0, -5.0, 0.0, 10.0, 20.0, 30.0, 40.0, and 50.0 ±0.1 nm, with $x = 0$ corresponding to the HTL/EML interface, and the positive direction corresponding to the direction of hole transport. Devices were also fabricated with sensing layers placed at $x = -20$ and 55 nm. The value of η_{QY} for 3 vol% PQIr in NPD and mCBP:$Ir(dmp)_3$ was measured in an integrating sphere. Sample films were excited using a 325 nm HeCd laser. Green's function methods[7] were used to calculate η_{OC} at the peak wavelength of PQIr to account for microcavity effects. For sensing layers in the EML, $\eta_{QY} = 92.8 \pm 3.8\%$, and in NPD it was $63.7 \pm 1.7\%$. Additionally, 13 vol% $Ir(dmp)_3$ in Tris-PCz had $\eta_{QY} = 12.9 \pm 0.4\%$.

2.4 Measured exciton distribution and device performance

Measured values for I_{sense} are shown in Fig. 2.2. Results are given for current densities of $J = 0.1, 1.0, 10, 100$ mA/cm^2. At the lowest current density, the exciton density is highest at the interface between the EML and HBL. As the current density increases, the exciton profile shifts toward the anode side of the device. The exciton densities of devices A and B are largely similar, differing significantly only in the HTL and adjacent 10 nm of the EML. For device A, sensor emission from the HTL indicates that the exciton density there is increasing with current density. By contrast, device B shows no significant sensor emission from the HTL embedded sensing layers. Also, for

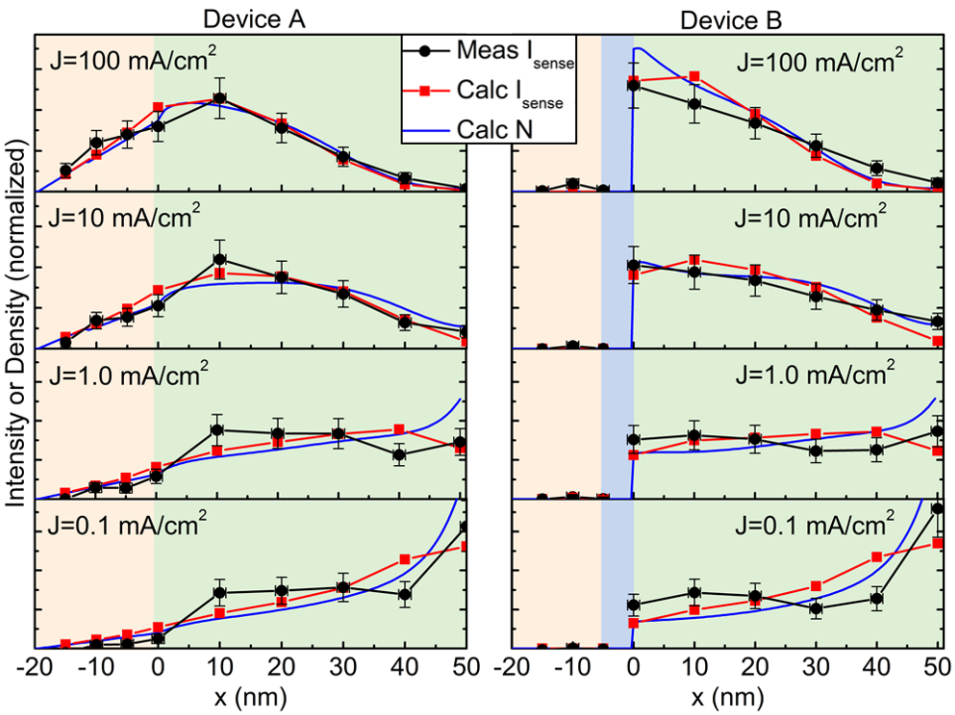

Figure 2.2: **Measured and calculated values for exciton distribution.** Device A is shown on the left and device B on the right for several current densities, J. All curves are normalized for comparison with the measured profiles. As before, the position $x = 0$ nm corresponds to the anode side of the emission layer. For device A, $x = -20$ to 0 nm is the HTL, while for device B, $x = -5$ to 0 nm is replaced by an electron blocking layer. Error bars along the ordinate are the deviation of I_{sense} measured for devices from two different growths as well as error in deconvoluting PQIr and $Ir(dmp)_3$ emission spectra. Error bars along the abscissa represent uncertainty in the measured layer thicknesses.

$J > 10$ mA/cm^2, the exciton density peaks at the EBL/EML interface. Additionally, significant sensor emission was not observed from the HTL of device B even after the device was degraded 50% of its initial luminance after continuous operation. This indicates that the EBL used in device B does not degrade in a manner that allows excitons to leak out of the EML under normal operation.

Sensing layers should not perturb charge transport and exciton density to provide a faithful picture of charge transport in the device being studied. One indicator of this is the deviation in the current-voltage characteristics after incorporating sensing

layers. In this study, the deviation in the voltage for sensing layer devices is $< 10\%$ of the mean voltage at $J = 10$ mA/cm^2. Additionally, the deviations are not correlated with the sensing layer position in the device, which indicates that the incorporation of sensing layers has not dramatically altered the charge transport properties of the device. Additionally, we note that no sensor emission was observed from layers placed adjacent to the HATCN HIL, which is expected because the deep energy levels of HATCN quench excitons[32]. However, the reported diffusion length for triplets in NPD is 87 nm[37], much greater than the thickness of the HTL, and we expect that excitons which leak into the NPD diffuse to the HATCN interface with high efficiency, where they are quenched.

The current density–voltage (J–V) characteristics, electroluminescence (EL) spectra, EQE, and operational lifetime at 3000 cd/m^2 initial luminance are given in Fig. 2.3 for devices A and B. The similarity of the J–V characteristics in Fig. 2.3a for devices A and B indicates that hole injection is the same with and without the blocking layer. The solid blue and black lines in Fig. 2.3b indicate that emission in the devices originates solely from the blue phosphor, despite the significant exciton density measured in the HTL. Examples of spectra from a device containing a sensor layer at $x = 0$ are shown by red dashed lines for different current densities. Fig. 2.3c shows that the EQE of device B is greater than that of device A. The improvement is about 5% at 1 mAcm^2 and 12% for $J > 1$ mAcm^2. Because the operating voltage was unchanged, it follows that the power efficiency is also improved. Finally, Fig. 2.3d shows the operating lifetime of devices A and B for constant current operation with an initial luminance of 3000 cd/m^2. The 50% luminance lifetime of device B is improved compared to device A, as is the voltage rise. Longer lifetimes for a similar device structure, although without an HTL, have been reported[32]. The difference may be due to purity of materials and growth conditions, or the use of the HTL in this study. Despite their lower lifetime performance, devices A and B are useful for

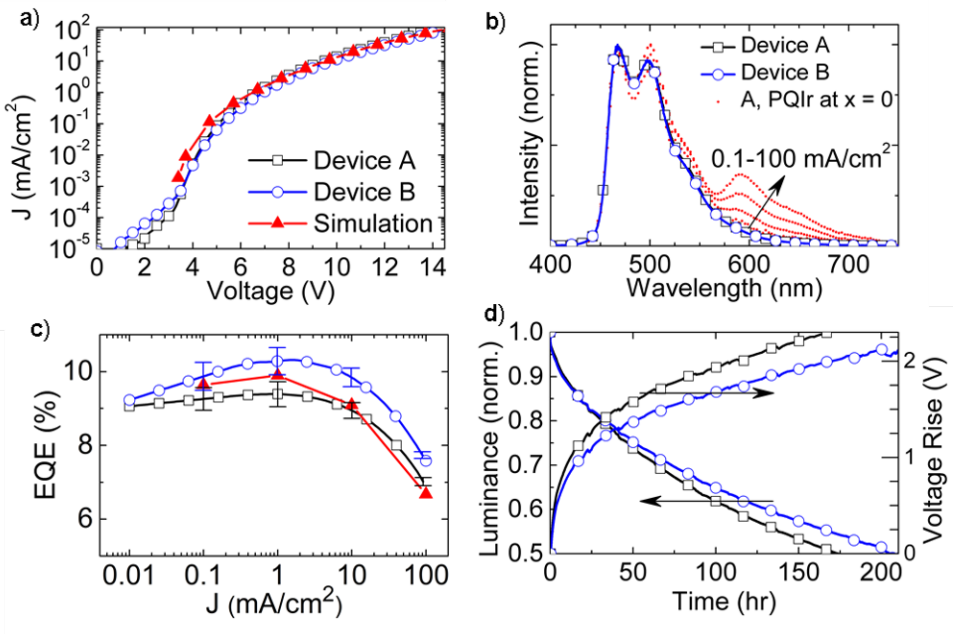

Figure 2.3: **Performance of PHOLEDs for confinement sensing.** (a) Measured and simulated J–V characteristics of devices A and B. (b) The electroluminescence spectra at J = 100 mA/cm^2 for both devices and example data from a device with embedded sensing layer at $x = 0$ nm (dotted lines) for $J = 0.1$, 1.0, 10, and 100 mA/cm^2. (c) Measured external quantum efficiencies for devices A and B. Simulated efficiency of device A is also shown. Error bars represent the standard deviation for > 5 devices. (d) Luminance and voltage characteristics as functions of device operating time at constant current, with an initial luminance of 3000 cd/m^2.

studying the charge balance and exciton confinement, as well as the relative lifetime performance with and without the modifed EBL.

2.5 Modeling and discussion of results

We simulate the charge and exciton transport dynamics using the equations in Section 2.1. Charge injection is treated identically for both devices because the J–V characteristics are the same. The charge mobilities in the transport layers are 2-4 orders of magnitude greater than in the EML[38,39]. Because of this and to simplify the calculation, we neglect the voltage drop over the transport layers. We determine the parameters used for modeling current transport in the EML by fitting the electron

Table 2.1: **Charge transport parameters used in model fits**

	Parameter	Value	Reference
Variable	ϕ (eV)	0.32 ± 0.03	
	μ_{e0} ($cm^2V^{-1}s^{-1}$)	$(5.8 \pm 0.3) \times 10^{-7}$	
	D_N (cm^2s^{-1})	$(2.3 \pm 1.0) \times 10^{-7}$ (EML 8% doping)	
	α ($cm^2V^{-1}s^{-1}$)	$(2.3 \pm 10.0) \times 10^{-}11$	
	β	0.54 ± 0.15	
Fixed	ϵ/ϵ_0	3.1	
	T (K)	297 ± 3	
	τ (µs)	1.1 ± 0.1 (EML), 100 (NPD)	[37,42]
	E_0 (V/cm)	$(1.4 \pm 0.2) \times 10^6$	This work
	D_N (cm^2s^{-1})	7.6×10^{-7} (NPD)	[37]
	V_{bi} (V)	3.0 ± 0.1	[32,35]
	d (cm)	$(1.1 \pm 0.1) \times 10^{-7}$	This work

and hole only device J–V characteristics reported in the supporting information for ref. [32] with the Mott-Gurney expression for space charge limited mobilities. For holes, which are transported on the HOMO of the phosphorescent dopant, the hole mobilities are then fit to the equation $\mu_h = \alpha exp(\beta C)$ $cm^2V^{-1}s^{-1}$, where the fitting parameters α and β are given in Table 2.1 and C is the doping concentration. This is the same functional form for mobility used for graded host EMLs [25,40]. The electrons, on the other hand, are transported on the host and are insensitive to the doping concentration [32], with a fitted mobility similar to that of the reported value for CBP [41]. We note that these fitting parameters are independent and give unique fits to the data.

From Fig. 2.1 we see that the greatest energy barrier charges must overcome to enter the EML is for electrons at the Alq_3/mCBP interface. Electrons entering the

mCBP HBL from Alq_3 must overcome the energy offset between the LUMO energies, $\phi = 0.5 \pm 0.3$ eV, as calculated from the reduction potential of mCBP (-2.77 V), which corresponds to a LUMO energy of 1.5 ± 0.3 eV[34], and IPES measured LUMO of Alq_3 is 1.96 eV. The result for the simulated current density changes significantly as the energy offset is varied across this range, so the value of the offset is adjusted within these bounds to achieve the best fit. The barrier width, $d = 1.1$ nm, approximately corresponds to the molecular spacing. Holes injecting into the EML face no significant energy barriers. The large HOMO offset at the interface between the EML and HBL ($\sim$ 1 V difference between $Ir(dmp)_3$ and mCBP) effectively blocks holes. Finally, ohmic contact is assumed between the electrodes and transport layers[43,44]. With this assumption, the built-in voltage is the potential between the HOMO level of $Ir(dmp)_3$ and the LUMO level of Alq_3.

Because NPD fluorescence between 400-450 nm[45,46] is not observed in the EL spectra of the devices while significant sensor emission is observed from the NPD layer of device A, we conclude that the leaking species are triplet excitons from the EML. Thus, the improvement of device B by incorporating a blocking layer is due to improving exciton confinement rather than charge balance. The energies of the layers are consistent with this conclusion: NPD has a triplet energy of 2.3 eV[47], less than that of $Ir(dmp)_3$ (2.7 eV). This means that exciton transfer into the HTL is exothermic for device A, whereas the NPD LUMO is high enough to provide some barrier to electrons. The EBL of device B comprises Tris-PCz and CZSi, which have triplet levels of 2.8 eV and 3.1 eV, respectively[36,48]. Thus, a mixture of these materials has a sufficiently high triplet energy to block excitons from the EML, as verified by the lack of emission from sensing layers in the HTL of device B. Thus, at the HTL/EML interface, $D = 0$ for device B but $D = D_N$ for device A.

The diffusion constant of the triplets is obtained by fitting it to the ratio of red to blue emission from the sensor layers. As shown in Eq. 2.8, the intensity of sensor

emission increases with the value of D. The fitted value of D yields $L_D = \sqrt{D\tau} = 5 \pm 1$ nm at 8 vol% $Ir(dmp)_3$, which is comparable to the reported value of 6.8 nm for $Ir(ppy)_3$ doped with the same concentration into CBP [49].

The results of the simulation are shown in Fig. 2.2. All parameter values are reported in Table 2.1. The solid blue lines correspond to the calculated exciton density, and the red points represent the emission intensity calculated using the exciton profile and Eq. 2.8. There is good agreement between the fit and the measured results across the full range of measured current densities. From these results, we understand that the decrease in sensor emission intensity at $x = 0$ nm compared to $x = 10$ nm in device A, which is not present for device B, is the result of exciton diffusion into the HBL. The simulated J–V in Fig. 2.3 are in good agreement with experiment in the space charge region, however the trapping that dominates the J–V characteristics at < 5 V were not considered by the model, resulting in deviation of the fit from the data.

The calculated polaron profiles are shown in Fig. 2.4. We find that at low bias, holes are efficiently injected due to the lack of energy barrier. This results in hole accumulation at the EML/HBL interface and a corresponding large density of excitons there. Electrons are injected over the barrier formed by the LUMO offset energy, which separates a large electron density from the holes. Thus, the field is maximum and nearly constant across the 5 nm thick HBL. As the voltage and carrier build up increases, the field across the HBL also increases, lowering the barrier and speeding up electron injection into the EML exponentially. Electrons near the cathode side of the EML have a higher mobility than holes at the same location due to the scarcity of hole-transporting dopant sites there. Thus, with increasing bias the electrons penetrate deeper into the EML as the electron current increases. This shifts the recombination zone towards the HTL, and the polarity of the net space charge on the HBL side becomes negative. This causes the voltage drop over the HBL to increase

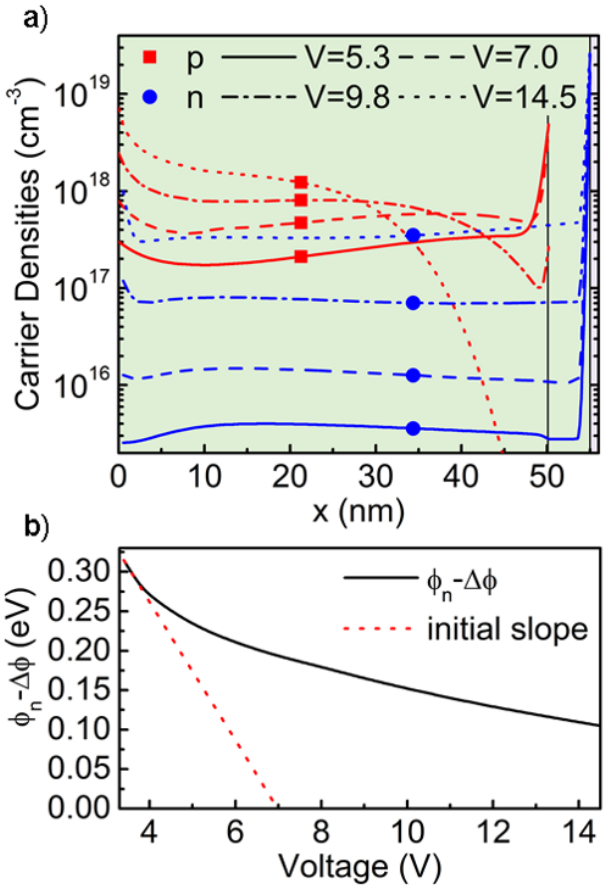

Figure 2.4: **Calculated polaron profiles and electron injection energy barrier reduction.** (a) Simulated hole and electron densities corresponding to the results in Fig. 2.2. Holes are blocked by HBL at $x = 50$ nm and electrons are blocked at the anode side of the EML at $x = 0$ nm. The electron current at is reduced by the energy barrier at the HBL/ETL interface at $x = 55$ nm. At low voltage, holes (solid line, squares) build up at the HBL/ETL interface, while electrons build up at the ETL/HBL interface, with a low injected electron density in the EML. As the applied voltage increases, the barrier height to electron injection into the HBL decreases and electrons penetrate deeper into the EML. (b) Electron injection barrier height $\phi_n - \Delta\phi$ vs. voltage. As electrons are injected into the EML, negative space charge decreases the barrier height. The slope of the dotted line shows the initial rate of barrier reduction for comparison.

more slowly with increasing voltage than it did at lower voltages. The effective barrier height is plotted in Fig. 2.4. At low bias it decreases linearly with voltage (dotted curve), but the decrease becomes sub-linear with increasing bias (solid curve). We note that the asymmetric injection barriers cause holes to outnumber electrons in the EML even when the exciton recombination zone is near the anode side of the EML. Also, we find that an efficient blocking layer material must have energy levels that are inaccessible by thermal excitation to charges and excitons in the EML.

Calculating the loss of EQE due to exciton leakage in device A, we find that $2.3 \pm 0.1\%$ loss is expected at $J = 0.1$ mA/cm^2, which increases to $11.9 \pm 0.1\%$ at 100 mA/cm^2. This is shown in Fig. 2.3b. The simulated efficiency is the measured efficiency of device A plus the calculated exciton loss. The discrepancy between the simulated efficiency and that of device B is likely due to inaccuracy in model parameters.

The relative lack of exciton confinement in the EML of device A is not apparent from the OLED $J - V$, luminance, and EL spectral characteristics and changes with current density. In general, a device may exhibit poor charge balance only in certain regimes, e.g. high or low current, complicating the evaluation of the blockers. In the devices considered here, there is significant leakage of triplets into NPD which does not appear in the PHOLED emission spectrum, and also does not occur at low current density. The sensing layers, therefore, provide an accurate means for determining if charge balance and exciton confinement are achieved using the blocking material of interest. Indeed, a device such as this could achieve maximum theoretical efficiency at low current density, and be erroneously assumed to have unity charge balance and exciton confinement.

Intrinsic degradation in blue PHOLEDs has been attributed to bi-molecular annihilation reactions, such as TPA[6,32,42,50]. The high energy of resulting hot excited states may cause bond rupture in the organic molecules, resulting in molecular frag-

ments[51–53] that trap charges and quench excitons, leading to voltage rise and luminance loss, respectively. Because reactions such as TPA and TTA occur more frequently at high current density, increasing device efficiency will reduce the current required to reach high brightness, improving reliability. Additionally, spreading the exciton density uniformly across the EML will reduce the TPA rate at a given brightness[32]. Another degradation mechanism that has been reported is due to molecular instability of some ionic excited states[42,54]. For example, Alq_3 has been reported to have an unstable cation (i.e. the charge state when carrying holes)[54]. Both of these mechanisms are addressed by improving η_{CB} and η_{EC}. We attribute the improved lifetime performance of device B shown in Fig. 2.3d to the improved efficiency and reduced exciton leakage into the HTL.

2.6 Summary

We have developed a framework for studying and measuring charge and exciton leakage in PHOLEDs using thin luminescent sensing layers. The quantitative model can be used to accurately describe the charge and exciton densities within the device, which is confirmed by the good agreement between the measured results using sensing layers and the calculated values for exciton density. Inserting an appropriate EBL improves exciton confinement in the EML, resulting in an increased EQE and operational lifetime. Sensing layers are particularly useful for characterizing blue PHOLEDs, where large carrier and exciton energies make it difficult to optimize charge balance and exciton confinement in the EML. Further, detailed knowledge of the exciton profile evolution with current density can lead to the engineering of recombination zones with broad, uniform exciton distributions useful for reducing efficiency roll-off[25] and increasing PHOLED lifetime[32]. We find that suitable blockers have LUMO and triplet energies that are inaccessible by thermal excitation from the EML, and that their operational stability can be evaluated using sensing layers em-

bedded within the transport layers. Indeed, the contribution of the blocking layer to device degradation can be evaluated by monitoring the emission from sensing layers embedded into the blocking or transport layers. This separates the effects of blocking layer degradation from other mechanisms, such as intrinsic degradation of dopant or host [32,42,50]. The effects of changes in charge balance and exciton confinement on device reliability will be discussed in greater detail in Ch. III.

CHAPTER III

The effect of charge balance and exciton confinement on phosphorescent organic light emitting device lifetime

In Ch. II, a method for determining charge balance and exciton confinement in PHOLEDs was introduced. Some attention was given to the effect of static values of η_{CB} and η_{EC} on the stability of devices. In this chapter, this study is expanded to measure the effect of changes in η_{CB} and η_{EC} on the operational lifetime of the device.

The usefulness of PHOLEDs in displays and other practical applications depends crucially on their reliability[55,56]. However, the lifetime of blue PHOLEDs is often too short for commercial applications, whereas green and red devices have already been adopted for display and lighting. Thus, detailed understanding of the challenges to be overcome for achieving highly reliable blue PHOLEDs is an important endeavor. Research on blue device reliability has primarily focused on the intrinsic degradation of the host guest system in the EML[6,32,50,54]. While intrinsic degradation of the EML is well established, other mechanisms may also contribute to luminance loss. Particularly, loss of charge balance or exciton confinement would directly affect the

luminance of devices. Thus, degradation of the blocking layers, increased resistance, or changes in the layer morphology can decrease the device reliability. By monitoring the emission of sensing layers embedded in the transport layers of a blue PHOLED, we measure the charge balance and exciton confinement efficiency as a function of operating time. We find that changes in exciton confinement do contribute to luminance loss, but only marginally ($< 5\%$ of total luminance loss). The main conclusions of this chapter were published in *Physical Review Applied* [57].

3.1 Measuring charge balance and exciton confinement in PHOLEDs

As in Ch. II, we employ thin red-emitting phosphorescent sensing layers embedded at strategic locations in the device. In the present study, we employ both fluorescent and phosphorescent red emitters in the sensing layers, which allows us to distinguish charge and exciton leakage. If we assume that the phosphor in the sensing layer efficiently collects all leaked charges and excitons, then the charge balance efficiency η_{CB} and exciton confinement efficiency η_{EC} are related to the measured sensor emission photon flux Φ_P by:

$$\eta_{CB}\eta_{EC} = 1 - \frac{q\Phi_P}{J\eta_{OC}\eta_{EU}\eta_{QY}}. \tag{3.1}$$

Here, q is the electron charge, J is the current density, η_{OC} is the outcoupling efficiency of the sensor emission, $\eta_{EU} = 1$ is the exciton utilization efficiency of the sensor layer, and η_{QY} is the quantum yield of the sensing layer emitter. Charges that recombine in the EML either directly form triplet excitons, or form singlets which rapidly convert to triplet excitons via intersystem crossing (ISC) [1,58]. Because triplets on fluorescent dopants are not emissive at room temperature, fluorescent sensors only emit if singlets are formed by charge recombination in the transport layer or due to Förster transfer

from the EML. Förster transfer can be prevented by spacing the sensing layer a sufficient distance from the EML, thus the fluorescent sensor can be made sensitive only to charge leakage (and recombination) in the transport layer. To quantify this leakage, η_{EC} is set to one and η_{EU} is set to 0.25 in Eq. 3.1. Thus, by measuring emission from both phosphorescent and fluorescent sensing layers in the HTL and ETL, η_{CB} and η_{EC} can be determined individually.

3.1.1 Requirements for sensing molecules

Appropriate emissive sensing materials should have a HOMO energy that is the same or deeper than the HTL, and a LUMO that is the same or shallower than the ETL. These properties prevent the dopant from trapping charge and altering charge transport in the layer. In addition, the exciton energy should be less than that of the hosting material to allow for efficient η_{ET} and emission. This also implies that the sensor emission will be easily spectrally resolvable from the primary emission of the device.

3.2 Fabrication of devices for measurement of charge balance and exciton confinement vs. operating time

Three sensing devices: PtOEP-HTL sensing, PtOEP-ETL sensing, and DCM2-ETL sensing, were grown by vacuum thermal evaporation (VTE) at a base pressure $< 5 \times 10^{-7}$ torr on solvent-cleaned substrates comprising a pre-patterned, 70 nm thick indium tin oxide (ITO, 60 $\pm$ 10 Ω/sq.) layer on glass. The substrates were exposed to UV-ozone for 10 min immediately prior to loading into the VTE chamber. The 2 mm^2 device area is defined by the intersection of the ITO anode and the 100 nm thick Al cathode, the latter patterned by deposition through a shadow mask. The device structure for the PtOEP-ETL sensing device is: ITO anode / 10 nm HATCN HIL /

20 nm NPD HTL / 30 nm mCBP doped 13 vol% with $Ir(dmp)_3$ EML / 6 nm mCBP HBL / 30 nm Alq_3 ETL / 1.5 nm Liq EIL / 100 nm Al cathode. The 2 nm thick Alq_3 layer immediately adjacent to the mCBP HBL is doped with 8 vol% with the red phosphor, PtOEP. The DCM2-ETL sensing device differs only by using a 0.05 nm thick layer of DCM2 located 10 nm distant from the EML rather then the PtOEP layer. The structure for the PtOEP-HTL sensing device is the same as above except that the HTL consists of a 20 nm thick CPD doped with a 0.1 nm thick PtOEP layer located 6 nm from the EML, with no sensor on the ETL side. Device structures are shown schematically in Fig. 3.1(a), along with the approximate transport levels of the materials. Each device has a single sensing layer, and in ETL sensing devices, CPD is replaced with NPD. The sensing layers are located sufficiently far from the EML to avoid direct Förster energy transfer from the blue dopant, $Ir(dmp)_3$. The transfer radii from $Ir(dmp)_3$ to PtOEP and DCM2 are 3.5 nm and 3.9 nm, respectively, calculated using previously reported sensor absorption spectra[59–61].

PtOEP was selected for the phosphorescent sensor material because it has a low triplet energy of 1.9 eV, suitable for hosting by Alq_3, which has a triplet energy of 2.1 ± 0.1 eV[62,63]. Also, its LUMO level is the same or very close to that of Alq_3[64] while the HOMO level is higher than that of Alq_3. Holes are therefore trapped on PtOEP in Alq_3, while electron transport should not be impeded[62,64]. On the HTL side, both NPD and CPD have HOMO levels around 5.5 eV, while NPD has a LUMO of 1.5 eV, with CPD expected to be similar. Thus, the PtOEP HOMO $= 5.3 \pm 0.1$ is within 200 meV of the HTL while its LUMO is about 0.5 eV lower than CPD, thus only electrons are strongly trapped on the phosphorescent sensing layer in the HTL. For the fluorescent layer on the ETL side, both electrons and holes may be trapped on DCM2 in Alq_3. Electron trapping in the ETL is undesirable, however we find no deviation in the J–V characteristic and conclude that the effect is small.

After fabrication the devices are encapsulated under dry nitrogen using a glass

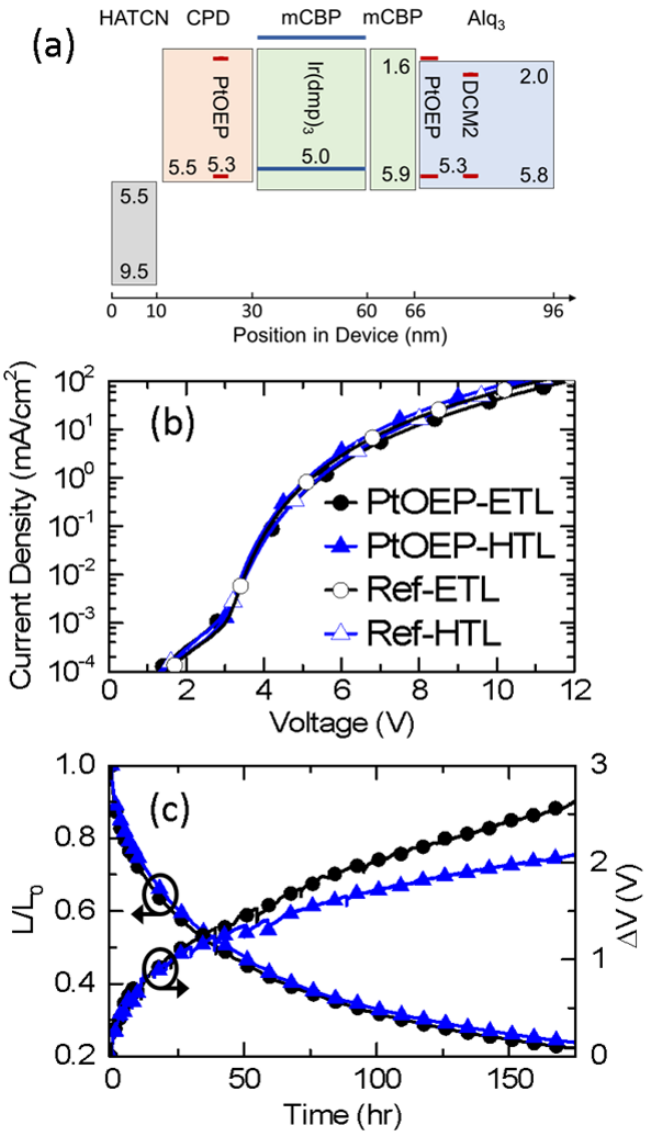

Figure 3.1: **Structure and performance of PHOLEDs for confinement sensing vs operating time.** (a) Schematic representation of devices. The energy levels of the organic layers, including the dopants and sensors are denoted inside the boxes, measured in eV from the vacuum level. Definitions of the acronyms used for each material are defined in text. Note that for the ETL-side sensing devices, the HTL is NPD rather than CPD. Each device contains a single sensing layer. (b) Current-density vs. voltage characteristics of the as-grown devices. Reference devices omit sensing layers but are otherwise unchanged. (c) Luminance (L) normalized to its initial value (L_0), and voltage rise (ΔV) vs. operating time at 30 mA/cm^2 for PtOEP-HTL and -ETL side sensing devices.

cover slide attached by UV curable epoxy at the edges. The current-voltage-luminance characteristics of the device were measured immediately following fabrication. Then, two of each device structure were operated at 30 mA/cm^2, and the EL spectra were measured at 1 and 10 mA/cm^2 every time the luminance dropped by about 5% (i.e. at T100, T95, T90, etc.).

3.3 Experimental results

To measure the quantum yield of the various sensor/host combinations, films with the following structures were fabricated on quartz substrates for measurement of η_{QY}: 25 nm thick Alq_3 doped with 8 vol% PtOEP, 5 nm CPD / 0.1 nm PtOEP / 5 nm CPD / 0.1 nm PtOEP / 5 nm CPD, and 5 nm Alq_3 / 0.05 nm DCM2 / 5 nm Alq_3 / 0.05 nm DCM2 / 5 nm Alq_3. The films were measured in an integrating sphere under nitrogen flow using a 325 nm HeCd laser as an excitation source. The quantum yield of the PtOEP:Alq_3 film was measured to be 14.9 ± 1.6%; PtOEP:CPD film, 28.5 ± 1.9%; and DCM2:Alq_3 film, 50 ± 9%. Green's function methods were used to calculate η_{OC} using optical constants for the various organic films obtained by ellipsometry, yielding $\eta_{OC}\eta_{QY} = 2.3 \pm 0.2\%$ for the PtOEP-ETL sensing layer; $5.1 \pm 0.2\%$ for the PtOEP-HTL sensing layer, and $7.5 \pm 1.4\%$ for the DCM2-ETL sensing layer.

The J–V characteristics of the PtOEP-ETL and PtOEP-HTL sensing devices, together with those for reference devices that do not have sensing layers are shown in Fig. 3.1b. The characteristics are similar for all devices, with slight variations due to different HTL materials and growth-to-growth variations. The DCM2-ETL sensing device, which is not plotted, also shows a similar characteristic to its reference device. The peak EQE of the devices was 8.8%. Luminance loss and voltage rise vs operating time at $J = 30$ mA/cm^2 are plotted in Fig. 3.1c for the PtOEP-HTL and -ETL sensing devices. All devices show the same luminance loss and voltage rise, independent of the sensing layers.

The emission spectra measured as the device degrades are shown in Fig. 3.2. The emission intensity of the PtOEP-ETL sensing layer increases with operation time, despite the overall reduction in intensity from the EML due to degradation. Sensor layer emission from the PtOEP-HTL device decreases over the same period. The sensor intensity is obtained by subtracting the aged reference spectra from the sensing device spectra. The sensor spectrum is plotted in the detail of Fig. 3.2. It is important to avoid saturation of all the sensor molecules present in the sensing layer. The site saturation limit can be estimated as $k_r N \approx \Phi_P/(\eta_{OC}\eta_{EU}\eta_{QY})$, where k_r is the radiative rate and N is the number of sensor molecules. Because the sensing layers are extremely thin (N is small) and the radiative rate of PtOEP is relatively slow ($\sim 10^4$ s^{-1})[65], the site saturation limit is much lower than for the emissive dopant in the EML of a traditional device. However, for this device we estimate that at $J = 10$ mA/cm^2 we are still two orders of magnitude under the excitation density at which all available sensor emitters are excited simultaneously. Interestingly, the sensor emission for the DCM2-ETL device, shown in Fig. 3.2, is unchanged with aging time.

3.4 Analysis of charge and exciton leakage

Using the spectra in Fig. 3.2, together with Eq. 3.1, we can calculate the losses due to charge and exciton leakage in this device. The fractional loss of EQE due to leakage of charges and excitons from the EML, calculated as $1 - \eta_{CB}\eta_{EC}$, is shown in Fig. 3.3. The percentage of leakage into the ETL, shown in Fig. 3.3a, increases nearly linearly as a function of percentage luminance loss. The percent leakage is smaller at higher current density because the exciton density shifts away from the HBL interface with increasing current[26]. Leakage into the HTL side doesn't change over the same range of current density. For clarity, only one current density is plotted for the HTL leakage in Fig. 3.3b because the curves at 1 mA/cm^2 and 10 mA/cm^2

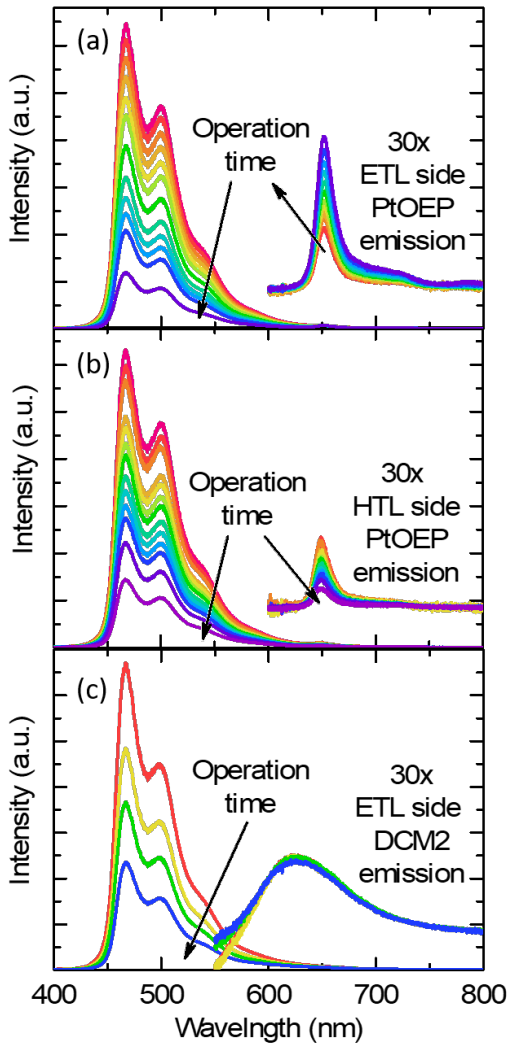

Figure 3.2: **Transport layer sensing device spectra vs. aging time.** (a) PtOEP electron transport layer (ETL) sensing device spectra. The intensity of the blue phosphorescent emission at wavelengths from 450 to 550 nm decreases with time while the sensor emission at 650 nm increases, indicating increasing exciton diffusion into the ETL. Data correspond to operating times of: 0, 0.1, 1.2, 3.3, 6.7, 11.4, 22.6, 39.5, 55.1, 71.7, 95.3, and 214 hours. (b) PtOEP hole transport layer (HTL) sensing device spectra. The sensing layer emission intensity decreases with time, indicating reduced leakage on the HTL side. Data correspond to operating times of: 0, 0.4, 1.5, 3.5, 8.0, 11.0, 16.4, 20.7, 30.1, 39.1, 59.2, 88.9, and 179 hours. (c) DCM2-ETL sensing device spectra. The intensity of the DCM2 emission is constant with time, indicating no change in hole penetration into the ETL. Data correspond to operating times of: 0, 0.3, 42.8, and 109 hrs. Sensor emission magnified by 30 X and vertically offset for clarity, is shown in the detail of (a)-(c).

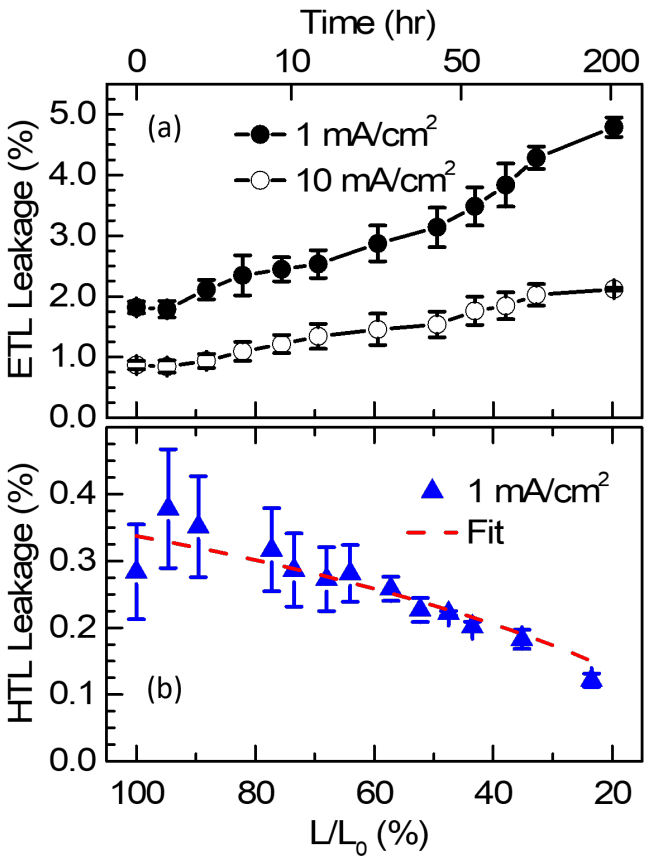

Figure 3.3: **Percentage of charges and excitons lost to transport layers.** Percent leakage, $100\%(1-\eta_{CB}\eta_{EC})$, on (a) the ETL and (b) the HTL side of the blue phosphorescent organic light emitting device at $J = 1$ mA/cm^2 and 10 mA/cm^2, vs. the percent luminance loss, L/L_0. The dashed line is a fit to the HTL side leakage. The HTL leakage decreases with time and is the same at both J=1 and 10 mA/cm^2 (not shown). Error bars represent the differences between two samples of each device type.

are overlapping. Error bars represent the variation between similar devices.

Because DCM2-ETL sensor emission is constant, we conclude that η_{CB} is not changing with device degradation. This is expected, as Alq_3 emission (as well as NPD emission) are absent from the aged spectra of all the devices. This implies that the increased emission from the PtOEP-ETL sensing layer is due to increasing triplet exciton leakage into the ETL.

Triplet exciton blocking at the EML/mCBP interface relies on the high triplet level of mCBP (2.95 eV[36]) relative to that of the phosphor $Ir(dmp)_3$ (2.7±0.1 eV).

One possible explanation for increasing exciton leakage into the EML is the generation of low triplet energy degradation products in the HBL. Several such fragments have been identified in studies of mCBP degradation routes in OLEDs[66,67]. An alternative explanation is morphological changes in the EML, which affects reliability of OLEDs and could play a role here[68]. For example, crystalite formation in the HBL could cause intermixing of the adjacent layers or local uneven film thickness and incomplete coverage.

HTL leakage in analogous devices has been attributed to exciton diffusion[26,69]. This is possible because of the low triplet energy of NPD compared to the EML. We note again that HTL material fluorescence is not observed, indicating electron recombination is not occuring in the HTL.

To understand the decrease in sensor emission from the PtOEP-HTL device, we need to separate two possible effects: First, as the device ages, excitons in the EML are expected to recombine more quickly due to quenching on defect sites, and thus the flux of excitons diffusing into the HTL should decrease. Second, changes in charge conduction with device aging could shift the recombination zone further from the HTL. We investigate these effects by solving the diffusion equation together with a TPA degradation model that considers defect generation, non-radiative recombination on defects, and exciton quenching[6]. Specifically, we solve the set of equations:

$$\frac{d}{dt}p(t,t') = \frac{J}{qd} - \gamma n(t,t')p(t,t') - k_{trap}Q(t')p(t,t') \tag{3.2}$$

$$\frac{d}{dt}n(t,t') = \frac{J}{qd} - \gamma n(t,t')p(t,t') - k_{rec}Q(t')n(t,t') \tag{3.3}$$

$$\begin{aligned}\frac{d}{dt}T(x,t,t') =& \frac{d}{dx}\left[D(x)\frac{d}{dx}T(x,t,t')\right] + \gamma n(t,t')p(t,t') \\ &- \left[\frac{1}{\tau_0} + k_{quench}Q(x,t')\right]T(x,t,t')\end{aligned} \tag{3.4}$$

$$\frac{d}{dt'}Q(x,t') = k_x n(t')T(x,t'), \tag{3.5}$$

Here the independent variables are t, the time on the timescale of generation and transport (on the order of microseconds); t', the time on the timescale of degradation and defect generation (timescale of hours); and x, the position. The independent variables $n(t,t')$, $p(t,t')$, $T(x,t,t')$, and $Q(x,t')$ are the electron, hole, free triplet, and defect densities, respectively. Additionally, $D(x)$ is the diffusivity, J is the current density, q is the electron charge, $d = 30$ nm is the EML width, $\gamma = 1.7 \times 10^{-13}$ cm^3s^{-1} is the Langevin recombination rate, $n(t,t')$ and $p(t,t')$ are the electron and hole densities, respectively, $k_{trap} = 1.4 \times 10^{-13}$ cm^3s^{-1} is the charge trapping rate constant, $Q(x,t')$ is the defect density, $k_{rec} = 4.8 \times 10^{-14}$ cm^3s^{-1} is the trapped charge recombination rate constant, $\tau_0 = 1.1$ µs is the exciton lifetime in the fresh device, $k_{quench} = 5 \times 10^-12$ cm^3s^{-1} is the rate constant for quenching of excitons by traps, and $k_x = 7 \times 10^-24$ cm^3s^{-1} is the defect generation rate constant. The values of the rate constants used here were reported previously for this host/dopant system [6]. The free triplet density is zero at the sensing layer, corresponding to complete trapping on the sensing molecules, and excitons are assumed to be blocked at the HBL. In the HTL, $D = 2.3 \times 10^{-7}$ cm^2s^{-1} and $\tau = 100$ µs [26]. In the EML $D = 7.6 \times 10^{-7}$ cm^2s^{-1}, while τ ranges from 1.1 µs in the pristine device to 0.5 µs at $L/L_0 = 0.16$ [6], with intermediate values obtained by linear interpolation. The exciton flux at the sensing layer is $D(x)\frac{dT(x,\infty,t')}{dx}$, evaluated at the position of the sensing layer.

To solve this equation set, we first solve Eq. 3.3-3.4 in steady state ($\frac{d}{dt} \to 0$) for the charge and exciton densities as functions of Q. We then solve Eq. 3.5 for the time evolution of $Q(x,t')$. Finally, the diffusive flux of excitons into the HTL is taken from the solution to Eq. 3.4. This predicts a trend for the rate of exciton leakage vs luminence loss, which is then fit to the data in Fig. 3.3b. The good agreement between the intrinsic degradation model and measured reduction in sensor emission

indicates that the measured effect is fully accounted for by the reduction in exciton density and the exciton diffusion length due to the generation of defects as the device ages.

The contribution of loss of charge balance and exciton confinement to luminance loss is:

$$\Delta L_{CB}(t') = \frac{1 - [\eta_{CB}(t')\eta_{EC}(t') - \eta_{CB}(0)\eta_{EC}(0)])}{1 - L/L_0}. \tag{3.6}$$

The result for $\Delta L_{CB}(t')$, calculated using PtOEP-HTL and PtOEP-ETL data, is shown in Fig. 3.4. Error bars are the difference in $\Delta L_{CB}(t')$ calculated for similar devices. Thus, we find that loss of exciton confinement accounts for approximately 3% of luminance loss at $J = 1$ mA/cm^2, and 1-2% at $J = 10$ mA/cm^2. This implies that intrinsic degradation of the EML is responsible for $\sim$97% of luminance loss, validating the assumption of dominant intrinsic degradation in previous work on the lifetime of blue PHOLEDs[6,32,42].

3.5 Summary

In conclusion, we have developed a technique for quantifying charge and exciton leakage into transport layers of OLEDs, which is particularly useful for evaluating phosphorescent devices to the nonradiative nature of leaked triplet excitons. We find that for a test blue PHOLED structure the charge balance is unchanged with lifetime, while exciton confinement efficiency degrades so slowly as to be almost negligible compared to intrinsic degradation. These results may vary greatly based on the device structure being evaluated, and the effect of charge balance and exciton confinement should be evaluated on a case by case basis. However, it is likely that significant improvement in the reliability of blue PHOLEDs will require more robust host and dopant molecules. This may be accomplished by judicious molecular de-

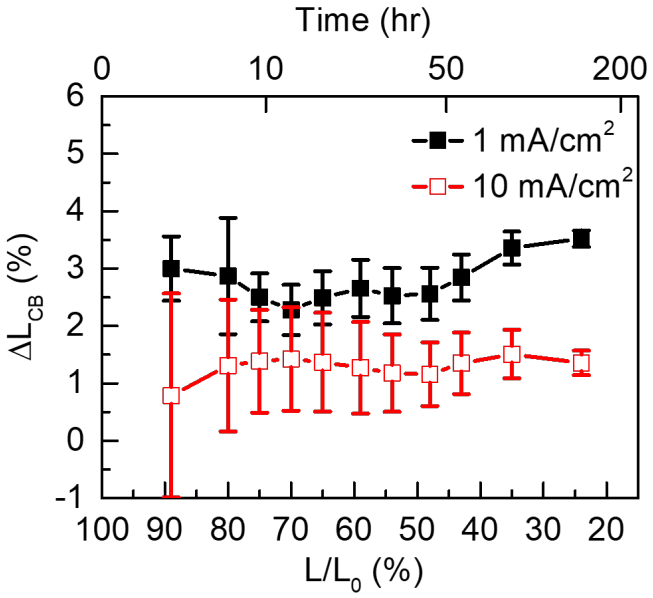

Figure 3.4: **Contribution of loss of charge balance and exciton confinement to PHOLED degradation.** Percentage contribution of loss of charge balance and exciton confinement to luminance loss, $\Delta L_{CB}(t')$, vs. the percentage of luminance loss, L/L_0, and operating time (top axis). Luminance loss is attributed to exciton leakage into the ETL, which accounts for 3% of the total loss in luminance of the blue electrophosphorescent device. At $J = 1$ mA/cm^2, the leakage is larger and increases more quickly than at 10 mA/cm^2.

sign to reduce coupling to the degradation pathways of the molecules or structural strategies[25,32,70,71].

CHAPTER IV

Stacked white organic light emitting devices for reliable solid state lighting sources

While the primary commercial success of OLED technology has been in information display, it is also a good candidate for high efficiency SSL. It was estimated that 232 billion kWh were used for lighting in the United States in 2015, with an average source efficiency of 50 lm/W[72], while incandescent light bulbs provide only 14 lm/W. OLEDs are suited to making white light sources due to their high power efficiency (over 150 lm/W is achievable[73]), broad tunable spectra, lambertian emission profiles, large-area rather than point source emission, and potentially very high reliability. In addition, they are compatible with flexible and rigid substrates and offer unique aesthetics that would be difficult to achieve with other technologies.

As discussed in Sec. 1.2.1, white light sources are characterized by their CCT and CRI. For context, an incandescent light bulb has a CCT $\approx 2400 - 2700$K with CRI $= 100$ because it is a true black body emitter, while a sodium lamp has a CRI of about 0. Lighting sources used in living spaces typically have CRI of 70 or better, while sources with CRI > 85 are regarded as having excellent color rendering. In this chapter we describe the fabrication of warm white PHOLEDs with a high CRI and reliability. This is done using all phosphorescent emitters incorporated into series

stacked devices to achieve high operational stability. The main conclusions of this chapter were published in *ACS Photonics*[74].

4.1 Determining the spectrum for a white light source

As discussed in Ch. I, the human eye is only sensitive to light in the wavelength range 400-700 nm. Therefore, to maximize power efficiency while maintaining good color rendering, it is desirable to achieve a spectrum similar to that of a black body source of the same CCT in the visible, but with no intensity outside visible wavelengths. Typical Ir based phosphors, such as FIrpic and $Ir(ppy)_3$ have full width at half maximum (FWHM) of about 60-100 nm. Thus, good coverage of the full visible spectrum can be achieved with three emitters, typically a blue, green, and red. Two-emitter[75–77] and even single-emitter[78] schemes are also possible, however the CRI suffers as a result of poor spectral adaptability. Here, we choose $Ir(dmp)_3$ as the blue emitter, $Ir(5'\text{-Ph-ppy})_3$ as the green emitter, and PQIr as the red emitter. The individual emitter EL spectra are shown in Fig. 4.1. By evaluating the CCT and CRI of a linear combination of the individual spectra, we find a target spectrum with CCT = 2815 and CRI = 88. The positions of the emitters on the 1931 CIE colorspace are also shown in Fig. 4.1. The coordinate of the calculated white spectrum is within one seven-step MacAdam's ellipse of the Plankian locus[79].

We choose to use a stacked OLED structure[80,81] for achieving the desired emission spectrum. This has two major benefits. First, the current required to achieve high brightness is reduced because multiple EML layers are series connected in an organic stack. This results in longer lifetime compared to a single stack device at the same brightness[32]. Second, it provides a natural way to incorporate the different emitters into the device, i.e, by incorporating a blue EML stacked with multiple green and red ones.

From the linear combination, we calculate the target spectrum is achieved for

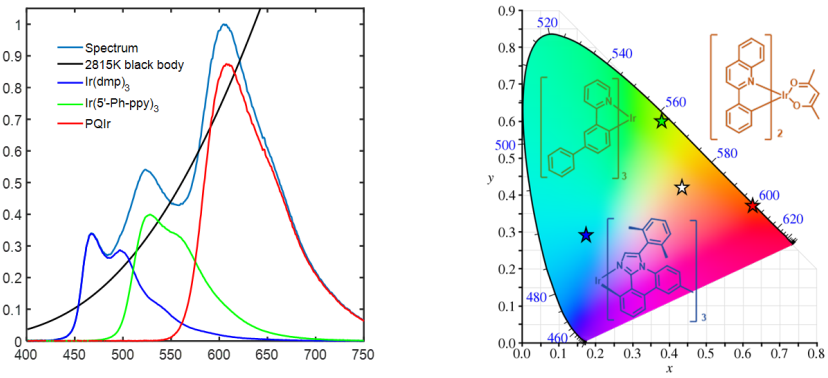

Figure 4.1: **Single emitter and target white spectra.** (left) Individual emitter EL spectra. Also shown is a black body spectrum with CCT = 2815 K and a linear combination of the emitter spectra approximating the black body spectrum. (right) The 1931 CIE colorspace coordinates of the emitters, target white spectrum, and the molecular structures of the blue ($Ir(dmp)_3$), green ($Ir(5'\text{-Ph-ppy})_3$, and red (PQIr) emitters.

emission rates from the various color emitters of 4.2 red photons and 1.5 green photons per blue photon. Considering that the blue phosphor $Ir(dmp)_3$ has $\eta_{QY} \approx 0.5$ while for $Ir(5'\text{-Ph-ppy})_3$ and PQIr $\eta_{QY} > 0.9$, we expect that this requires at least three red-green stacks blue stack if the outcoupling efficiency of each is the same. The task of constructing a SWOLED can therefore be broken down into the design of its constituent parts, i.e. the red and green emitting stack, the blue emitting stack, an organic series connector, called a charge generation layer (CGL), then combining the elements in a way that considers the optical cavity of the device to maximize outcoupling and minimize resistive losses in connecting layers.

4.2 The red-green emitting structure

Efficient, long lived red and green OLEDs have been successfully developed and are used commercially in displays. However, much of the technology involved (materials and structures) have not been disclosed. Red and green structures with high efficiency are routinely fabricated, but simultaneously achieving long lifetime can still

be challenging. The HBL is particularly important for the reliability of green and red devices based on CBP or mCBP hosts, however one of the best performing reported HBL materials, BAlq, has a triplet energy that is too low to confine green triplet excitons, resulting in poor *EQE* in structures geared toward reliability[82]. The triplet energy of BAlq is high enough to act as either a host or efficient blocking layer for the red emitter PQIr, however. Inspired by the work in previous chapters, where sensor emission from red emitting layers embedded in the transport layers was used to quantify exciton leakage, a structure was designed whereby triplet excitons which leak from the green doped EML layer into the low triplet energy BAlq HBL lead to emission from PQIr doped into the blocking layer. This strategy avoids the efficiency loss associated with poor exciton confinement, although it does incur a loss to power efficiency due to the thermalization of the energy difference between the red and green excitons.

4.2.1 Red-green emitting structure fabrication and optimization

Single stack OLEDs were fabricated using the same methods as previously described to evaluate the red-green emitting stack red to green ratio, efficiency, and lifetime. The structure was glass substrate / 150 nm ITO / 10 nm HATCN / 20 nm NPD / 10 nm CBP : 8 vol% Ir(5'-Ph-ppy)$_3$: 10 vol% PQIr / X nm mCBP:9 vol% Ir(5'-Ph-ppy)$_3$ / 3 nm BAlq / 5 nm BAlq:10 vol% PQIr / 5 nm BAlq / 45 nm BPyTP2 / 1.5 nm Liq / 100 nm Al. Here, the thickness of the green doped EML thickness, X, is either 20, 25, or 30 nm. The current density-voltage, *EQE*, and spectra of the devices are given in Fig. 4.2. Thinner green EML layers give lower operating voltage at the same current density. Peak *EQE* values reach 18.8%, without outcoupling enhancement, indicating that losses due to leaked triplet excitons are successfully avoided. Because the position of the exciton formation zone dependence on current density, the ratio of red to green emission also changes with

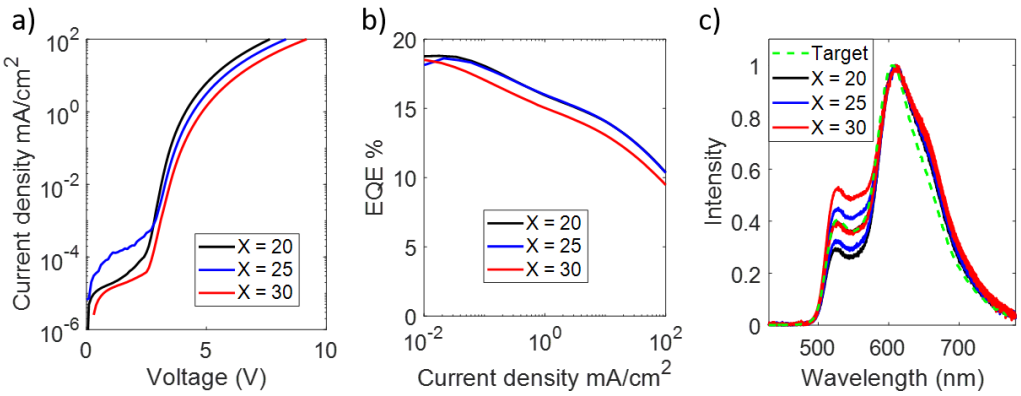

Figure 4.2: **Performance of red-green single element devices.** (a) Current density-voltage characteristics for a series of red-green devices with structures described in text. Current density decreases with increasing X (green emitting layer thickness). (b) The EQE decreases slightly with increasing X. (c) Electroluminescence spectra of the devices at 1 mA/cm^2. Here, the dashed green target line represents the calculated target red-green emission spectrum. In each case, the spectrum with larger intensity around 520 nm corresponds to 10 mA/cm^2, while the spectrum lower intensity at 520 nm is measured at 1 mA/cm^2.

current. This is mitigated to some extent by placing another codoping PQIr into the 10 nm of EML adjacent to the hole transport layer, which compensates for lowered red emission as the exciton formation zone shifts towards the HTL. This layer serves the dual purpose of preventing exciton leakage into the HTL because the triplet level of PQIr is lower than that of NPD. Other structures were tested to optimize the layers and choice of materials. Device performance was found to be insensitive to the thickness of the neat BAlq layer separating the green EML from the PQIr doped BAlq in the range from 3-5 nm, indicating that Förster transfer is avoided. Replacing the BPyTP2 ETL with Alq_3 resulted in over 1 V increase at 1 mA/cm^2 due to its lower charge mobility, demonstrating that power efficiency is significantly higher for the BPyTP2 ETL device.

The devices were aged with a constant 10 mA/cm^2 driving current, which is equivalent to about 2650 cd/m^2. The resulting luminance loss and voltage rise as a function of time are shown in Fig. 4.3. We find that of all the measured performance

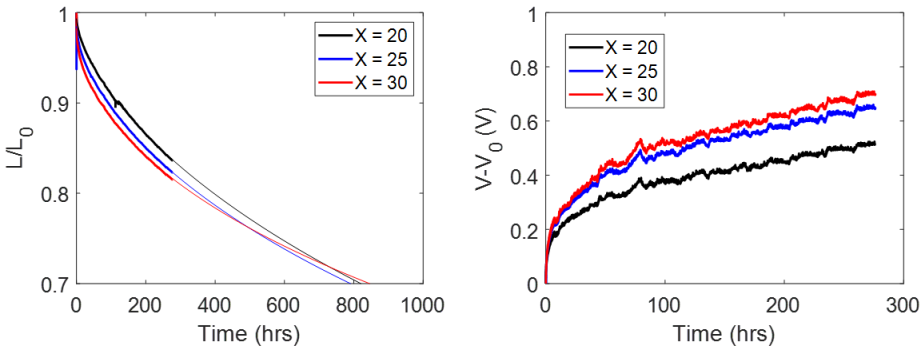

Figure 4.3: **Lifetime of red-green single element devices.** (left) Luminance over time, normalized to the initial luminance. Extrapolated lifetime using the stretched exponential decay model, (i.e. $L/L_0 = exp[-(t/\tau)^{\beta}]$) are shown as thin lines. (right) Voltage rise over time. Voltage rises faster for larger X.

characteristics, the red-to-green emission ratio was the strongest function of X. We therefore set X = 25 nm in the red-green element for the SWOLED to most closely match the target emission spectrum.

4.3 The blue emitting structure

The lifetime of the blue element is important to prevent color shift and a rapid decrease in luminance with aging. We maximize blue device lifetime by using a graded dopant profile and hot excited state management [32,83]. Dopant grading balances hole and electron transport in the EML, resulting in a broadened exciton recombination profile and reduced bi-molecular annihilation rates, compared to a similar device with constant doping at the same brightness. Also, it was found that including the deep blue phosphor mer-Ir(pmp)$_3$ can 'manage' hot excited states, that is, reduce the probability of a hot excited state degrading the host or emitter molecules [83]. The blue element only accounts for 15% of the initial luminance, so its degradation impacts color shift more strongly than luminance loss. Increasing the lifetime of the red-green element without increasing the blue element lifetime would accelerate color shift with aging. The maximum allowable color shift depends on the application [84],

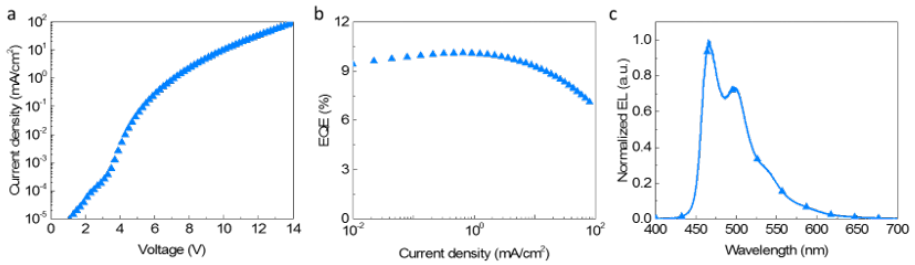

Figure 4.4: **Performance of blue single element devices.** (a) Current density-voltage characteristics. The blue device operating voltage is several volts higher than for the red-green device. (b) The EQE characteristic for the blue PHOLEDs. Due to its low η_{QY}, Ir(dmp)$_3$ based devices are limited to $\sim 10\%$ EQE. (c) Electroluminescence spectra of the devices.

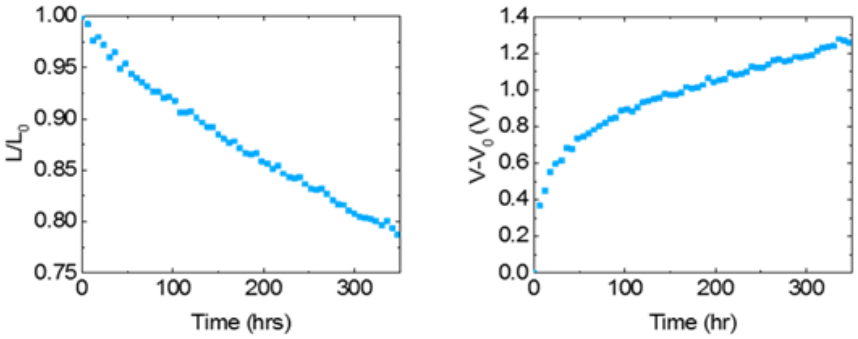

Figure 4.5: **Lifetime of blue single element devices.** (left) Luminance over time, normalized to the initial luminance of 1000 cd/m^2. The extrapolated T70 lifetime is about 600 hrs. (b) Voltage rise over the same period.

and can also limit the useful device lifetime.

The optimized structure for a blue device incorporating graded doping and excited state managers was reported in *Nature Materials* [83]. The single element blue device structure was 70 nm ITO / 5 nm HATCN / 10 nm CPD / 20 nm mCBP:18→14 vol% Ir(dmp)$_3$ / 10 nm mCBP:11→19 vol% Ir(dmp)$_3$:3 vol% mer-Ir(pmp)$_3$ / 20 nm mCBP:12→8 vol% Ir(dmp)$_3$ / 5 nm mCBP:8 vol% Ir(dmp)$_3$ / 5 nm mCBP / 25 nm Alq$_3$ / 1.5 nm Liq / 100 nm Al. The performance of this structure is shown in Figs. 4.4 and 4.5.

4.4 The charge generation layer

To series stack devices, there must be an intermediate point between them where the polarity of the current carrier changes. This requires charge generation, i.e, a process leading to a free hole moving into one device and a free electron moving in the opposite direction towards the other device. Here, we interface HATCN and NPD to form a charge generation point. Because HATCN has a LUMO level nearly degenerate with the NPD HOMO, there is not an energy barrier for an electron in the NPD HOMO to hop into the HATCN LUMO, which results in an electron and hole, or charge generation. This is shown in Fig. 4.6. However, due to the low lying HATCN LUMO compared to that of the BPyTP2 ETL, there is a large energy barrier for electron injection into the ETL, which would incur a large voltage penalty. This can be overcome by n-doping the ETL. The resulting ionized charges in the n-doped ETL can transfer to the HATCN LUMO at the interface, setting up a large interface dipole that reduces the injection barrier[85].

Because of optical design considerations which are discussed in the next section, it is desirable to be able to stack devices as closely as possible. To test the charge generation voltage dependence of the thickness of the HATCN and e-ETL layers, CGL test devices with the following structure were grown: 150 nm ITO / 10 nm HATCN / 30 nm NPD / Y nm HATCN / Y nm 3 vol% Li:BPyTP2 / 30 nm BPyTP2 / 1.5 nm Liq / 100 nm Al. The voltage required for charge generation is approximately equal to the difference between the forward (ITO positive) and reverse bias voltages at the same current density. The CGL test device performance is shown in Fig. 4.7. The voltage required to operate the CGL is small compared to the single element operating voltage, and the voltage rise of the CGL is negligible compared to the single element device voltage rise. For the operating voltage test and the CGL in the SWOLED, the thickness Y was increased to 12 nm.

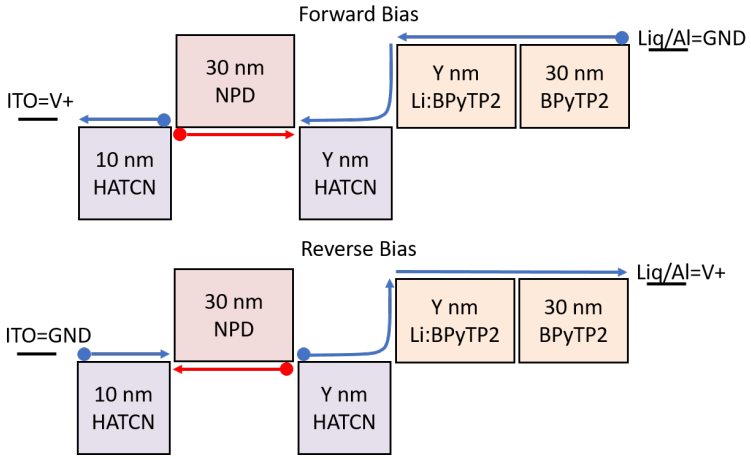

Figure 4.6: **Schematic operation of a charge generation test device.** (Top) Forward bias operation ($V_{anode} > V_{cathode}$) injects charges from the contacts and results in charge recombination at the interior interface between NPD and HATCN. (bottom) Reverse bias operation ($V_{anode} < V_{cathode}$) results in charge generation at the interior interface between NPD and HATCN. The voltage difference to reach the same current density between forward and reverse bias is approximately the voltage required to generate the current. Energy levels are drawn assuming a flat vacuum level.

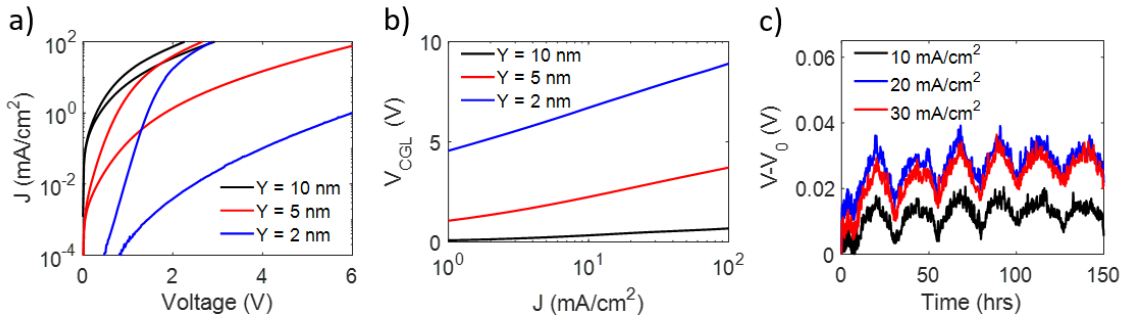

Figure 4.7: **Operating voltage and lifetime of charge generation test devices.** (a) Forward and reverse current density-voltage characteristics for different values of Y. Forward and reverse characteristics are shown in the same color, with reverse having lower current density at the same voltage. (b) Reverse minus forward voltage as a function of current. For Y = 10 nm, the CGL operating voltage at 1 mA/cm^2 is less than 0.2 V. (c) Operating voltage rise of the CGL devices under constant current load (reverse bias).

4.5 Outcoupling considerations

As discussed in Sec. 1.2.2, the position of light generation in the organic material impacts the coupling of light to the various modes. Using a Green's function method, we calculate the outcoupling efficiency vs position at wavelengths of 460, 520, 560, and 600 nm, see Fig. 4.8. Because substrate modes are relatively easy to outcouple using microlens arrays or similar strategies, we also calculate the sum of power coupled to air and substrate modes. At the first antinode, around 50 nm from the cathode, the outcoupling maxima at different visible wavelengths are largely overlapping due to the shared node at the cathode. However, at the second antinode, maxima for the 460 nm and 600 nm wavelengths are spatially separated by about 70 nm. Thus, by placing a red-green element at the first antinode, then the single blue element at its second antinode, there is room to position a second red-green element near its second antinode. Beyond this, wavelength dispersion causes the broad spectrum of the red-green emitting element to no longer have a well defined antinode, especially when considering both air and substrate modes.

4.6 Full SWOLED: structure and performance

The full structure of the SWOLED devices incorporating the red-green emitting, blue emitting, and charge generation elements, is shown in Fig. 4.9. Devices having three, four, or five total emissive elements are denoted D3-D5. Each device has a single blue element combined with a varying number of red-green elements.

The J-V-luminance characterization used a semiconductor parameter analyzer and a calibrated large area photodiode that collected all light exiting the bottom of the glass substrate. For substrate-mode outcoupling measurements, IMF was placed between the photodiode and substrate. The device output spectra were measured using an integrating sphere coupled to a spectrometer. The J–V characteristics are

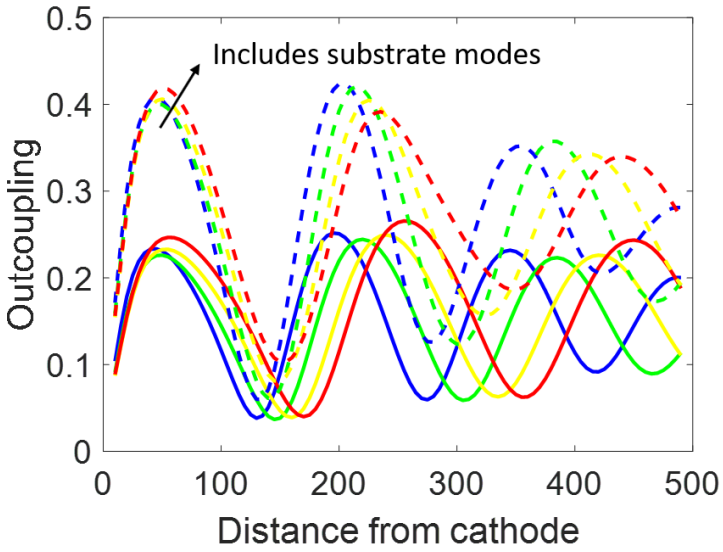

Figure 4.8: **Outcoupling efficiency vs emission position for selected visible wavelengths.** Outcoupling efficiency is shown for wavelengths of 460 nm (blue line), 520 nm (green line), 560 nm (yellow line), and 600 nm (red line). Solid lines indicate coupling to air modes. Dashed lines indicate coupling to air and substrate modes. Substrates modes can be extracted using IMF or lens systems. The total thickness of the organic layers in the calculation was 500 nm, with refractive index $n = 1.75$. An ITO anode is located at 500 nm from the cathode.

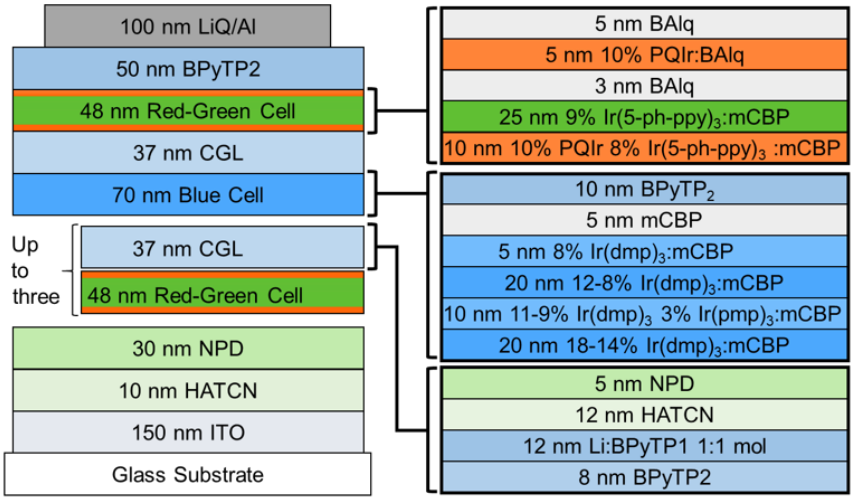

Figure 4.9: **Full structure of stacked white OLED devices.** (left) Stacked, all-phosphorescent white device structure. SWOLEDs D3, D4, and D5 have one, two, and three CGL/red-green element pairs below the blue emitting element, respectively. The total number of layers in D5 is 48. (right) Detailed layer structure of the red-green emitting element, blue element, and CGL.

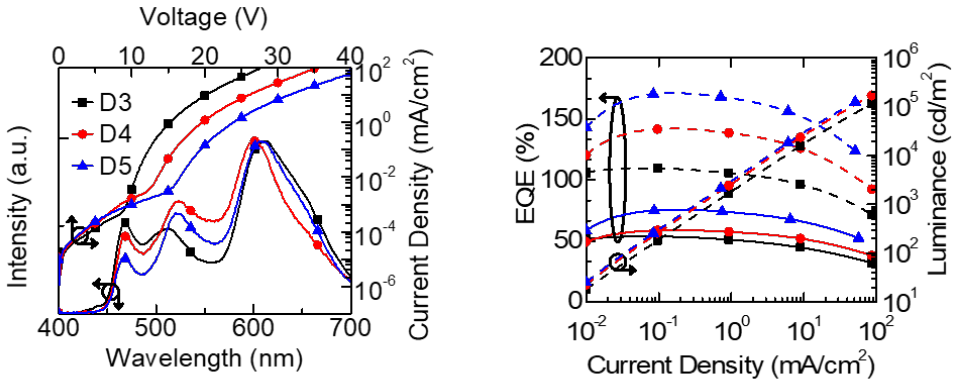

Figure 4.10: **SWOLED J–V and efficiency characteristics.** (left) The spectrum and current-density voltage characteristics of D3-D5. The voltage increases in regular steps with the number of red-green emitting elements. (right) EQE and luminance as functions of current density. Dashed lines represent quantities measured using IMF to outcouple all substrate modes.

given in Fig. 4.10(left). In the range J = 1-50 mA/cm^2, the voltage increase when adding additional red-green elements is 0.1-0.5 V less than the voltage of the red-green test device (Fig. 4.2) at the same current-density. We conclude that the voltage drop across the CGL is less than over the transport layers and contacts of the single EML test devices. The EL spectrum of each device is also shown in Fig. 4.10. Devices D4 and D5 exhibit balanced red, green, and blue emission. The peak near 520 nm in the D3 spectrum is blue-shifted by 10 ± 1 nm compared to D4 and D5. There is also some position and width variation in the peak near 610 nm. These differences are due to changes in the cavity and the different outcoupling vs wavelength characteristics for the different red-green element positions. The CCT, CRI, and 1931 CIE coordinates of the spectra of fresh devices, as well as after aging to T70 are summarized in Table 4.1.

The EQE and luminance for D3-D5 are shown vs. J in Fig. 4.10(right). Here, dashed lines were obtained by outcoupling substrate modes using IMF between the device substrate and photodetector during the EQE measurement [86], leading to an outcoupling improvement of 2.2±0.2 times over substrate emission without any out-

Table 4.1: **Performance characteristics of SWOLEDs**

	CCT[(a)] (K)	**CRI**[(a)]	**CIE**[(a)]	$J^{(b)}$ ($\frac{mA}{cm^2}$)	$V^{(b)}$ (V)	$EQE^{(b)}$ (%)	$LPE^{(b)}$ (lm/W)	$T70^{(b)}$ (10^3 h)
D3	2978	78.7	(0.44,0.40)	1.1	15.3	50.8	18.5	9 ± 2
	/2518	/81.2	/(0.47,0.41)	/0.5	/14.2	/107	/40.6	26 ± 7
D4	3300	85.1	(0.43,0.44)	0.9	19.3	57.7	19.1	15 ± 4
	/2890	/85.2	/(0.46,0.43)	/0.4	/17.8	/141	/47.2	50 ± 15
D5	2780	88.6	(0.46,0.43)	0.7	23.0	74.3	19.5	24 ± 5
	/2420	/89.4	/(0.49,0.43)	/0.3	/21.5	/170	/44.7	80 ± 20

(a) Measured at T100 / T70 and $J = 10$ mA/cm^2
(b) Measured with no outcoupling / outcoupling at $L_0 = 1{,}000$ cd/m^2

coupling scheme. While simple outcoupling schemes such as microlens arrays give smaller improvement factors ($\sim$1.5)[87], similar improvements to that measured here using IMF are achievable with other, deployable, wavelength independent outcoupling schemes[86,88–91]. The EQE increases with the number of stacks, and assuming EQE = 10% for the blue element without outcoupling[6,32], the average red-green element EQE in D5 is 16.4$\pm$0.1%, which is slightly lower than for the single element red-green test structure ($18.0 \pm 0.3\%$). Using IMF for substrate optical mode outcoupling, D5 reaches a maximum $EQE = 171 \pm 1\%$ (averaging 34.2% EQE per stacked element) and a luminance $> 200,000$ cd/m^2. The luminous power efficiency rolls off from $LPE = 50 \pm 3$ to 30 ± 2 lm/W (24 ± 2 lm/W to 13 ± 1 lm/W without IMF) as the current-density increases from 0.1 to 10 mA/cm^2, with an increasing number of stacks tending to slightly increase the power efficiency.

Example spectra for D4, both fresh and aged to T70, are shown in Fig. 4.11. The spectrum red shifts with aging due to the more rapid decrease in blue and green emission relative to red. The angular emission intensity is shown in Fig. 4.11(left),

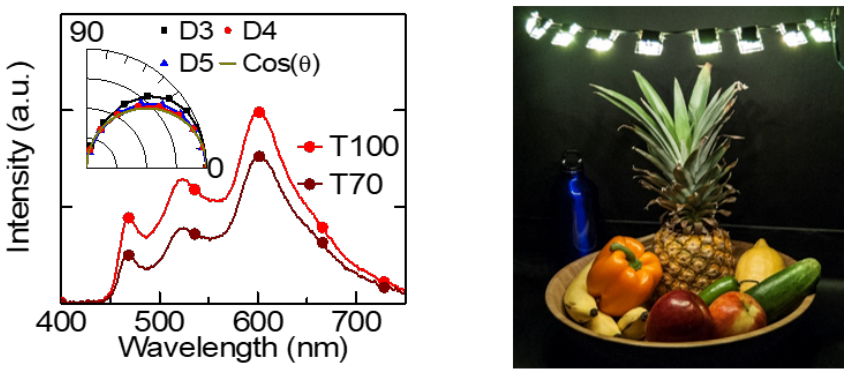

Figure 4.11: **Spectral characteristics of the SWOLEDs.** (left) Spectrum of D4 before and after aging. Inset: Angular emission intensity for D3-D5. The gray line without symbols represents a Lambertian profile. (right) Photograph of a bowl of fruit and blue bottle illuminated by a luminaire comprising 36, 2 mm^2 packaged SWOLED sources (12 each of D3, D4 and D5). The intensity of each element is 50,000-100,000 cd/m^2. The visibility of the range of hues in the photograph, including deep red and blue, demonstrates the high color rendering of the sources.

inset. The angle-dependent spectra were measured with a spectrometer using a lens-coupled fiber on a rotation stage that collected light in a 5° cone. Devices D4 and D5 have nearly Lambertian emission profiles, while the stronger cavity effects of D3 result in a higher intensity at ∼45° than expected for a Lambertian source. The devices exhibit color shifts with angle and brightness: as the current density increases from 1 to 10 mA/cm^2, the color temperature increases by 338 ± 1 K. The spectral dependence on viewing angle is characterized by a standard deviation in color temperature of < 340 K from 0 to 60°. The color rendering fidelity provided by the SWOLEDs is demonstrated by the photograph in Fig. 4.11b. The luminaire comprises 36, 2 mm^2 test coupons (12 each of D3-D5), each driven at 50,000-100,000 cd/m^2.

Luminance loss vs time for D3-D5 are shown in Fig. 4.12a. Luminance and voltage at constant current vs. operation time of a population of > 6 devices for each of D3-D5 was measured using source-meters and photodiodes multiplexed with a digital multimeter. These data are used to extrapolate the lifetime at an initial luminance of

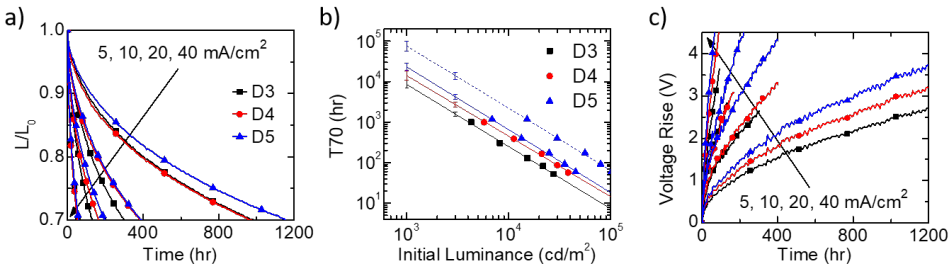

Figure 4.12: **Lifetime characteristics of the SWOLEDs.** (a) Normalized luminance loss vs. time at current densities of $J = 5$, 10, 20, and 40 mA/cm^2. At the same currents, luminance losses are reduced for devices with increasing numbers of stacked elements, which also have higher initial luminances. (b) Extrapolation of T70 vs. initial brightness. Error bars represent one standard deviation from a fit to the data using the relation: $T70 \times L_0^n = const$, with $n = 1.50 - 1.54$. The dashed line corresponds to the initial luminance obtained using substrate mode outcoupling. (c) Operating voltage rise versus time at $J = 5$, 10, 20, and 40 mA/cm^2. The voltage rises by 10-15% between T100 and T70.

1000 cd/m^2 using the relationship $T70 \times L_0^n = const$, shown in Fig. 4.12b. The fitted value of the exponent n is 1.50-1.54, and L_0 is the initial brightness[92,93]. Because outcoupling schemes result in higher luminance at the same current density, they also result in longer lifetime at the same luminance, as shown by the dotted line for D5 in Fig. 4.12b. At $L_0 = 1000$ cd/m^2, T70 $= 26 \pm 7$ khr, 50 ± 15 khr, and 80 ± 20 khr, for D3, D4, and D5, respectively. Error bars represent one standard deviation in the extrapolated lifetime determined from the least squares fit. At the increased luminance of $L_0 = 3000$ cd/m^2, $T70 = 5 \pm 1$ khr, 10 ± 2 khr, and 14 ± 3 khr, for D3, D4, and D5. Voltage rise data are shown in Fig. 4.12c. The 2.5 V to 4.5 V increase in $T70$ for the devices represents 10-15% of the initial driving voltages. The constant current testing of the CGL-only device (see Fig. 4.7), which shows that the voltage rise contribution from the CGL is < 30 mV after > 250 hr at 30 mA/cm^2, which is longer than $T70$ of the device at the same drive current. This indicates that over 95% of the voltage rise is due to aging of the layers comprising the SWOLEDs other than the CGL. Device performance is summarized in Table 4.1.

4.7 Analysis of SWOLED performance

Stacking multiple elements lowers the current density required to reach a given luminance, increasing the SWOLED lifetime and maximum brightness. Combining red and green emitters into a single element improves the spectral control compared to stacking separate red and green EMLs. Stacking also simplifies the design by allowing for separate optimization of each emitting element. Large numbers of stacked elements result in high voltage, low operating current devices. This is beneficial to lifetime, which improves dramatically as current density is reduced (Fig. 4.12a). The maximum number of stacks is determined by the allowable driving voltage or efficiency considerations for a particular application. Indeed, we find that the maximum LPE increases slightly with the number of stacks. Additionally, the lower current required to achieve a given brightness reduces the efficiency roll-off, increasing power efficiency at high luminance. The slight increase in power efficiency from D3 to D5 indicates it is possible to further increase the number of stacks before resistive and absorption losses significantly reduce the LPE.

The primary performance metrics for solid state lighting devices are the color quality (CCT and CRI), power efficiency, and lifetime. The CRI is > 85 for both D4 and D5, with warm white CCTs. The power efficiency is 30-50 lm/W, which may be improved by reducing operating voltage or better outcoupling. Ideally, this could also be improved by using a high η_{QY} blue emitter, however we are limited by the relatively poor reliability of most such molecules. Methods for decreasing operating voltage include higher mobility hosts/dopants with smaller energy gap differences, electron and hole conducting cohosts, and reducing the EML thickness. Also, separate red and green EMLs can improve outcoupling, however more reliable structures are required to realize these improvements without sacrificing lifetime.

To our knowledge, device lifetime of $T70 = 80 \pm 20$ khr with $L_0 = 1000$ cd/m^2 is the longest for white PHOLEDs with reported materials and structures. Lifetimes of

white PHOLEDs have been limited by rapid degradation of the blue EML, with $T70 <$ 1 khr [83]. Blue fluorophores are therefore often used for their reliability in hybrid fluorescent/phosphorescent white OLEDs [33]. However, the longest fully reported hybrid fluorescent/phosphorescent device lifetime under the same test conditions of which we are aware is 31 khr [94], which is less than half that of the PHOLEDs reported here. This indicates that blue PHOLED lifetime, when increased by excited state management, is sufficient for many lighting applications. Additionally, using CGLs to stack EMLs and red-emissive blocking layers are crucial to achieving the long SWOLED lifetimes reported here.

The small color shift of these devices with aging, shown in Fig. 4.11(left) and Table 4.1, is achieved by the balanced degradation rates of the emitting elements. The spectrum red-shifts slightly with time, due to the lower operational stability of the blue element: when D5 reaches T70 the blue emission is decreased by 50%. At the SWOLED T70, the blue cell loses about 5% more luminance without the hot excited state manager, and 40% more luminance without either grading or hot excited state manager.

4.8 Summary

In conclusion, we have demonstrated all-phosphorescent warm white, stacked PHOLEDs with lifetime of $T70 = 80$ khr and a high CRI of 89. This is achieved using three phosphors in five stacked EMLs comprising a device with a total of 48 layers. The device features red emissive blocking layers in the red-green element, graded doping and hot excited state management in the blue element, and stable, low voltage CGLs. These devices demonstrate the potential of white PHOLEDs for solid state light sources. The design principles and strategies employed will undoubtedly lead to the further improvement of long lived SWOLEDs.

CHAPTER V

Centimeter-scale electron diffusion in photoactive organic heterostructures

The unique properties of organic semiconductors are of fundamental interest while being increasingly important to information displays, lighting, and energy generation. However, organics suffer from both static and dynamic disorder that can lead to charge conduction via variable-range carrier hopping[95,96]. This results in notoriously poor electrical properties with electron and hole mobilities typically $\mu < 1$ cm^2/V-s and correspondingly short charge diffusion lengths ($L_D = \sqrt{D\tau} < 1$ µm), where D and τ are the diffusivity and lifetime, respectively)[97,98]. These properties often constrain organic optoelectronic devices which must be thin ($\sim$ 100 nm), with continuous top and bottom electrodes to avoid charge recombination and high resistance to lateral transport within the organic layers. Here, we demonstrate an organic heterostructure comprising a thin fullerene channel with significant photocurrent response to light absorbed > 1 cm beyond its collecting contact. The channel is sandwiched between an electron blocking layer and a blended donor:C_{70} HJ that generates charges by dissociating excitons. The energy barrier between the channel and HJ confines electrons to the fullerene layer, spatially separating them from photogenerated holes in the HJ. As a result of this energetic confinement and exceptionally low trap densi-

ties within the channel and along its interfaces, centimeter-scale diffusion of electrons is observed in the fullerene channel that can be fit with a simple electron diffusion model. Our experiments enable the direct measurement of charge diffusivity in organic semiconductors, which is as high as $D = 0.83 \pm 0.07$ cm^2/s in a C_{60} channel at room temperature. The high diffusivity of the fullerene combined with the extraordinarily long charge recombination time yield $L_D > 3.5$ cm, which is orders of magnitude larger than expected for an organic system. The main conclusions of this chapter were published in *Nature*[99].

5.1 Device fabrication

A series of devices was fabricated on 5 cm × 5 cm glass substrates containing four pre-patterned indium tin oxide (ITO) strips (150 nm × 1 cm × 2.3 cm) as bottom electrodes. Substrates were cleaned by sequential sonications in tergitol, deionized water, acetone, and isopropanol followed by snow-cleaning[100] on a 100°C hot plate with a stream of gaseous CO_2 and a 10 min UV-ozone exposure. The photoactive device structure was 150 nm ITO / 10 nm MoO_x / 80 nm donor:C_{70} 1:1 / fullerene / electron blocking layer / 100 nm Ag. The donor in the HJ was DTDCPB, DTDCTB, SubPc, or DBP. The fullerene is either C_{60} or C_{70}, and the electron blocker is either an 8 nm thick layer of BPhen or a 10 nm thick layer of 1:1 BPhen:C_{60} with a 5 nm thick BPhen cap. Mixed blocking layers are commonly used in OPVs to improve stability and electron extraction efficiency[101,102].

Organic materials, metals, and MoO_x were deposited at rates of 0.5-1 Å/s through shadow masks in a vacuum thermal evaporator at 10^{-7} Torr. Organics and MoO_x were deposited through a large square mask, leaving 1 mm of the substrate uncoated around the periphery for electrical contacts to the ITO. Using a separate shadow mask, 1 mm wide strips of 100 nm thick Ag films, were deposited across the organics to form the cathode, with 0.1 cm^2 of intersection perpendicular to the ITO bottom

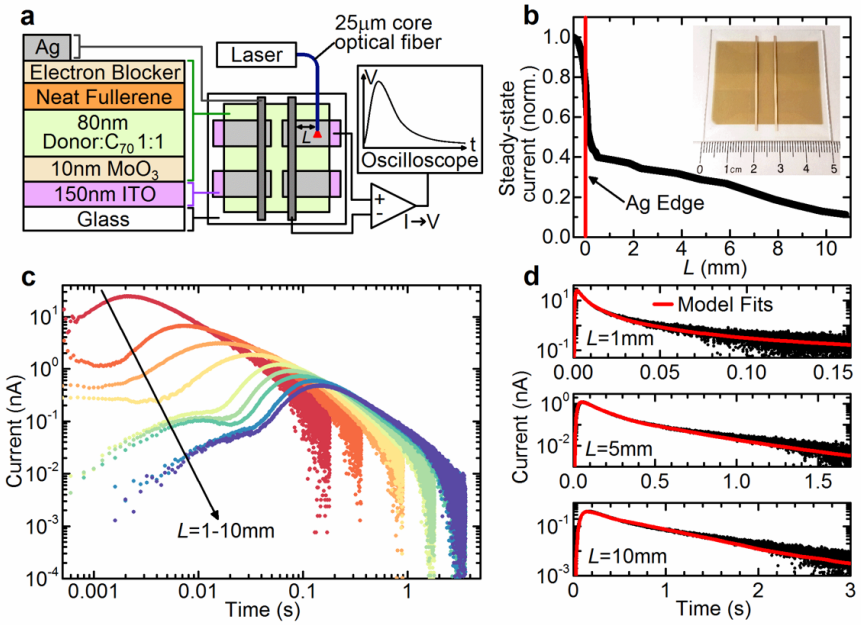

Figure 5.1: **Device structure, experimental setup, and distance dependent photocurrent.** (a) Device structure (left) and schematic of the substrate design with experimental setup for transient photocurrent measurements (right), where L is the distance between the fiber illumination position and the edge of the Ag cathode. (b) Normalized steady-state current of a DTDCPB-(10 nm C_{60})-Neat device due to constant 633 nm illumination at position L. Inset: photograph of the device prior to encapsulation. (c) Room temperature photocurrent transients of a DTDCPB-(10 nm C_{60})-Neat device illuminated with 500 μs pulses at 405 nm wavelength for L = 1-10 mm. (d) Charge diffusion model simulations (lines) and corresponding transient photocurrent data (points) at L = 1, 5, and 10 mm.

contact, as shown in 5.1a. The steady-state photocurrent device was encapsulated using a glass cover sealed to the substrate with a bead of UV cured epoxy around its periphery.

The device structure is shown in Fig. 5.1a, with a device photograph shown in Fig. 5.1b, inset. Devices are identified following the convention: (Donor in the HJ)-(Type and thickness of the neat fullerene channel)-(Electron blocking layer, i.e. Neat or Mixed). The devices share a common architecture with planar-mixed donor/acceptor (D-A) HJ organic photovoltaic cells (OPVs) [101,103] whose power conversion efficiencies are $> 9\%$ [104].

5.2 Measurement of lateral photocurrent

Using the experimental setup and device illustrated in Fig. 5.1a, the steady-state photocurrent response of an OPV comprising the d-a-a' DTDCTB blended with C_{60} was measured as a function of the excitation position under ~ 0.15 mW/cm^2 continuous illumination at 633 nm through the substrate from a fiber-coupled He-Ne laser, with results in Fig. 5.1b. In contrast to typical OPVs that exhibit no photoresponse to light incident outside the area of overlap of their anode and cathode, the DTDCTB-(10 nm C_{60})-Neat device generated a significant photoresponse to such illumination. The magnitude of the steady-state photocurrent just outside the cathode was 40% of the peak within the device, decreasing approximately linearly to 12% at $L = 10$ mm away from the cathode edge, likely due to recombination or trapping at the film edge where it contacted the encapsulation epoxy. The large drop in signal intensity at the edge of the cathode originates from a decrease in light absorption due to the lack of cathode reflection as well as a decrease in charge generation/collection efficiency due to the lack of a built-in field outside of the contact area. The photocurrent generated outside the contact overlap, henceforth called "channel current," can cause a significant overestimation of the short-circuit current in an OPV when it is overfilled by the illumination source[105]. Devices with DTDCPB as the donor also exhibited channel currents, while those with SubPc or DBP as the donor had no response to light outside the cathode edge.

Transient photocurrent measurements were performed under vacuum in an open-loop liquid N_2 cryostat with four vacuum feedthroughs for electrical contacts, optical fiber, and micrometer fiber positioning arm. The 25 µm diameter core fiber with a numerical aperture of 0.1, and a measured Gaussian output width of < 40 µm was positioned normal to the device surface. Pulses (duration of 0.5 ms to 2 ms and delays of 1 s to 100 s between pulses) from diode lasers (wavelengths 405 nm and 637 nm) were focused into the fiber for temporal measurements. The position of the fiber was

controlled with an x-y-z micrometer positioning stage. A 99% optically absorptive black foil was placed beneath the device to minimize light scattering. The current response was amplified with a low-noise current amplifier at 10^8 V/A, and recorded with a digital oscilloscope. Rise time filters between 10 µs and 10 ms were used on the current amplifier to minimize noise, and all spectra were averaged over at least 10 pulses. The steady-state dark current was subtracted, leaving only the transient response to the light pulses.

The transient behavior of channel currents in all device architectures was investigated, with 500 µs pulses of 405 nm wavelength light as the illumination source. Figure 5.1c shows the transient channel current from the DTDCPB-(10 nm C_{60})-Neat device illuminated at $L = 1 - 10$ mm. As L increased, the amplitude and arrival time of the channel current varied by nearly two orders of magnitude, though the standard deviation of the integrated charge collected for each transient was $< 10\%$ of the mean for all transients. That is, we observe no measurable loss in the total number of charges collected, independent of the position of excitation, indicating the charge L_D in the structure is considerably greater than the 1 cm device length. In devices with C_{70} channels, the integrated signal decreased by 50% over 5 mm, suggesting that L_D is small compared with C_{60}. The EQE (in this context, EQE = electrons collected per incident photon) decreased as a function of pump pulse energy and duration, presumably due to increased recombination at higher polaron concentrations. In the DTDCTB-(10 nm C_{60})-Neat device at $L = 2$ mm, the EQE decreased from 30% to 15% as the pump pulse energy increased from 0.11 to 1.7 nJ at a wavelength of 637 nm, and EQE decreased by 72% as the pulse length was increased from 0.1 to 100 ms. The collection efficiency of channel currents was wavelength independent, i.e. it tracked the absorption spectrum of the blended HJ. Channel currents were only observed when illuminating the organic area above the ITO anode, which was needed to collect the photogenerated holes, thus preventing sample charging and reducing

recombination.

5.2.1 Fitting data with electron diffusion model

Charge dynamics were simulated from a solution to the diffusion equation,

$$\frac{d}{dt}N(x,y,t) = D\nabla^2 N(x,,y,t) - kN(x,y,t) + G(x,y,t), \tag{5.1}$$

subject to blocking boundary conditions along the edges of the organic film and a quenching boundary condition at the edge of the Ag cathode. Here, N is the electron density, x is the distance from the cathode, y is the lateral position, t is the time, D is the diffusivity, k is the sum of the trapping and recombination rates, and G is the generation rate. Initially, $N(x,y,0) = 0$. The generation term is given by

$$G(x,y,t) = \frac{Q}{qt_{pulse}}\frac{1}{2\pi\sigma^2}\left[\frac{(x-x_0)^2+(y-y_0)^2}{2\sigma^2}\right], \tag{5.2}$$

where Q is the charge injected into the fullerene transport layer, $\sigma = 40$ µm is the laser beam diameter, (x_0, y_0) and t_{pulse} are the position and length of the excitation, respectively. The intrinsic carrier density in the fullerene layer is typically $< 10^8$ cm^{-3}, depending on the purity[106], which is many orders of magnitude below the optically excited and electrically injected charge densities.

The current transient is given by the diffusion current into the cathode as a function of t:

$$I(t) = q\int D\,\frac{d}{dx}N(x,y,t)\bigg|_{x\to 0} dy. \tag{5.3}$$

Equations 5.1-5.3 are solved numerically, and Eq. 5.3 is fit to the data with parameters D, k, and Q. The diffusivity primarily determines the arrival time of the current pulse and the slope of the falling edge, k determines the slope at long times, and Q scales linearly with amplitude.

Due to the device symmetry and the blocking conditions on the perimeter of the

Table 5.1: **Room temperature charge diffusion parameters extracted from distance-dependent transient current measurements**

Device	D (cm^2/s)	k (s^{-1})	μ^* $cm^2/V\text{-}s$	Q (nC)
DTDCPB-(10 nm C_{60})-Neat	0.83 ± 0.07	0.9 ± 0.6	32 ± 3	2.2 ± 0.8
DTDCTB-(10 nm C_{60})-Neat	0.67 ± 0.06	1 ± 1	26 ± 2	0.32 ± 0.02
DTDCPB-(5 nm C_{60})-Neat	0.53 ± 0.03	0.4 ± 0.4	20 ± 1	0.35 ± 0.02
DTDCPB-(2 nm C_{60})-Neat	0.16 ± 0.02	0.7 ± 0.7	6 ± 1	0.29 ± 0.03
DTDCPB-(10 nm C_{60})-Mixed	0.37 ± 0.08	0.3 ± 0.2	14 ± 3	3.2 ± 0.8
DTDCPB-(10 nm C_{70})-Neat	0.16 ± 0.01	2.4 ± 0.8	6 ± 1	0.21 ± 0.02

*Estimated using the Einstein relation

organic films, diffusion parallel to the cathode interface does not affect the arrival time of electrons at the cathode except in the case of diffusion around a cut in the organic film. The simulated geometry is therefore one-dimensional in most cases, simplifying computation.

This model was used to fit all transient currents as a function of L. Detailed transients (points) from Fig. 5.1c plotted on a log-linear scale are shown for the DTDCTB-(10 nm C_{60})-Neat device in Fig. 5.1d at L = 1, 5, and 10 mm. The parameters extracted from the fits (lines) are given in Table 1. Among devices grown in the same batch, DTDCTB and DTDCPB devices with 10 nm thick C_{60} channel and neat electron blocking layers had comparable diffusivities, which were reduced by replacing the C_{60} with C_{70}, and by replacing the neat electron blocking layer with a mixed layer. This reduction is presumably due to electron diffusion into the mixed layer where D is relatively low. Decreasing the C_{60} channel thickness in the DTDCTB-C_{60}-Neat devices from 10 nm to 2 nm also decreased D and the amount of total charge injected into the fullerene layer, Q. The peak-to-peak roughness of the films grown on ITO is typically several nanometers as measured by atomic force microscopy[107], thus the thin fullerene channels likely have discontinuities and

thickness variations that disrupt electron diffusion in thinner channels. The upper bound for the rate of charge trapping and recombination, k, was about five times larger in C_{70} compared with C_{60} channels. There were batch-to-batch variations in D, k, and Q, but the relative performance between architectures was consistent, i.e. devices with neat blockers or neat C_{60} always had considerably higher D than devices with mixed blockers or C_{70} grown in the same batch.

5.2.2 Electron diffusion around a cut in the film

Room temperature transient currents were measured on a DTDCTB-(10 nm C_{60})-Mixed device at $L = 3$ mm before and after a series of razor blade cuts was made to the organic layers, as shown in the inset of Fig. 5.2. The peak height of the current pulse was significantly reduced and the peak arrival time was delayed for devices with a "partial cut" that was transverse to, and spanned the width of the ITO anode between the illumination position and the Ag cathode, compared with the pristine, uncut device. These results are shown in Fig. 5.2. Charge diffusion simulations were performed for both geometries, where the only difference was a blocking boundary condition at the position of the partial cut. We find that charge diffusion around the cut accounts for the differences between the cut and uncut device transients, as demonstrated by the remarkable agreement between fits (lines) and the data. The partial cut was also extended such that there was no continuous organic path between the illumination position and the cathode, called a 'full cut' device. This eliminated the response except for a residual current at time, $t < 200$ ms arising from scattered light absorbed in the organic layers between the cathode and cut. This effect was observed in all devices exhibiting channel currents.

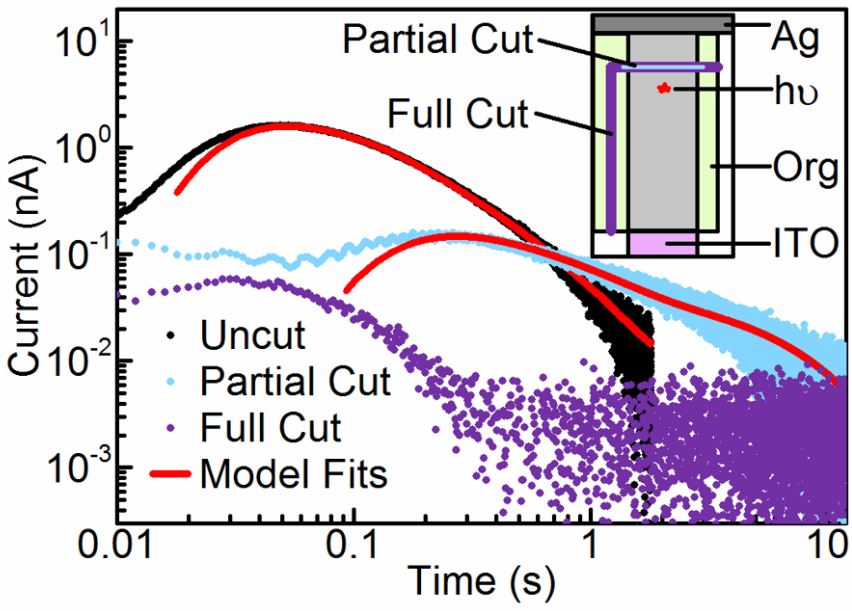

Figure 5.2: **Impact of channel disruption on channel currents.** Current transients at $L = 3$ mm with a series of cuts, as shown in the inset. Diffusion model fits are shown for the uncut and partial cut geometries.

5.3 Frontier orbital energies of HJ and channel materials

UPS data were measured for donor:C_{70} blends both with and without a 5 nm C_{60} cap. The HOMO energies were measured under high vacuum (10^{-8} Torr) with a 21.2 eV photon source. Organic thin films were grown on conductive ITO substrates as described above. The LUMO energies were estimated using the low energy optical absorption edge of the material. The energy barrier between C_{70} in the donor:C_{70} blend and the neat C_{60} layer on top was estimated by measuring the binding energy of the C_{70} HOMO in a 10 nm thick donor:C_{70} blend with a 5 nm thick C_{60} cap, measuring the binding energy of the C_{60} HOMO and taking the difference between these energies.

With the DTDCPB donor, we observe a 0.42 ± 0.1 eV difference between the highest occupied molecular orbital (HOMO) energy (E_{HOMO}) of the blended C_{70} and neat C_{60} cap, whereas the difference in E_{HOMO} between neat C_{60} and C_{70} is ~ 0.1 eV. The difference in E_{HOMO} between DBP:C_{70} blends with and without a 5 nm C_{60}

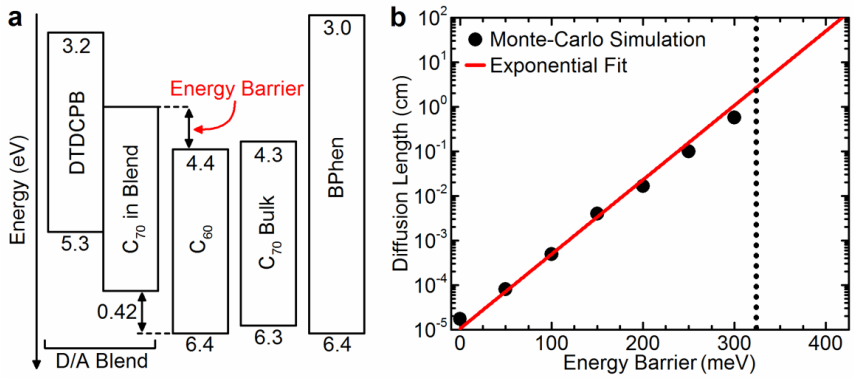

Figure 5.3: **Energetics of materials employed in devices.** (a) Energy level diagram extracted from ultraviolet photoelectron spectroscopy measurements on a 10 nm thick C_{70} and a 10 nm thick DTDCPB:C_{70} blended film with and without a 5 nm thick C_{60} film grown on its surface. (b) Monte Carlo simulations of the hopping diffusion length as a function of the energy barrier height for electrons between the neat channel layer and the donor-acceptor heterojunction. The dotted line indicates the lower bound of the energy barrier measured via UPS.

cap was < 100 meV, indicating that DBP does not significantly shift E_{HOMO} of C_{70} when the two constituents are blended. The energy levels are shown in Fig. 5.3.

To quantify the impact of the energy barrier between the fullerene channel and HJ, we performed Monte Carlo simulations of the carrier transport within the device structure to calculate L_D, with results shown in Fig. 5.3b. Monte Carlo simulations of charge diffusion were performed on a simple cubic lattice that contained $200 \times 7 \times 100$ sites in the x, y, and z dimensions, respectively, with lattice constant $a = 1$ nm. Here, x and y are the directions parallel to the substrate, while z extends vertically from the substrate. Sites with $z < 90a$ were designated as the donor:C_{70} blend, while the top 10 sites represented the neat fullerene channel. The blend was randomly generated, with 50% of the sites occupied by fullerenes, corresponding to a 1:1 blend. Periodic boundary conditions in y were used, with blocking interfaces at $x = 0$ (the periphery of the organic films) and $z = 100a$ (the interface between the fullerene channel and the electron blocking layer). Quenching boundary conditions were assumed at $z = 0$ (the MoO_x/HJ interface) and $x = 200a$ to collect electrons. Charges originating at $(1, 1, 1)$

were allowed to diffuse using the Miller Abrahams hopping rate, as follows: during each step of the computation, a random direction was chosen for an electron hopping attempt, with the probability of success given by $p = exp(-E/k_BT)$, where E is the energy difference between the two sites. We let $E = E_B$ for hops from the channel to the blend, $E = \infty$ for hops onto donors, and $E = 0$ otherwise. This assumes the barrier for intermolecular hopping can be neglected in the lateral diffusion efficiency calculations as it does not affect the relative probability of hopping over the barrier vs laterally. Energetic disorder, which may decrease the calculated value of L_D, is also assumed to be small compared to the E_B. The charge diffusion efficiency over the length of the simulated lattice, η'_D, is given by the ratio of charges quenched at $x = 200a$ vs. at $z = 0$. Thus, the diffusion efficiency over a distance, x, is given by: $\eta_D(x) = (\eta_D)^{x/d})$, where d is the length of the simulated lattice and the charge diffusion length is: $L_D = -d/ln(\eta'_D)$. We find that L_D is thermally activated as a function of barrier height following: $L_D(\mu m) = (0.1 \pm 0.03)exp(E_a/k_BT)$, where k_B is Boltzmann's constant and T is the temperature. The fit is indicated by the solid line in Fig. 5.3b. The pre-factor is the diffusion length at $E_B = 0$. The lower bound of L_D is 2.2 cm at 320 meV (dotted line, Fig. 5.3b), which corresponds to the lower bound of the measured energy barrier in the DTDCPB:C_{70} film with a C_{60} cap. The L_D inferred from the measured $E_B = 0.42$ eV is two orders of magnitude larger than this lower bound.

5.4 Temperature dependent transient photocurrent measurements

The temperature dependence of the current transients in DTDCTB-(10 nm C_{60})-Neat and DTDCTB-(10 nm C_{70})-Neat devices was obtained at 20K intervals in the range: 300K $\geq T \geq$ 120K. Temperature was controlled by the liquid N_2 flow rate and

a resistive heater, and monitored with a thermocouple. The results are shown in Figs. 5.4a and 5.4b at $L = 2$ mm and $L = 1$ mm, respectively. Each current transient was fit using the charge diffusion model as shown by solid lines in Figs. 5.4c and 5.4d, with the extracted values of D and k plotted vs. $1000/T$ in Figs. 5.4e and 5.4f.

Diffusion simulations successfully fit the data in Fig. 5.1 and 5.4 except at the leading edge of the current transient. During measurement, some scattered light is absorbed along the channel between the Ag edge and the intended point of photoexcitation, generating a prompt current response that is not accounted for by the model. This response is delayed with increasing L, as can be seen in Fig. 5.1b, since the scattered light is absorbed farther from the cathode, and bandwidth filters were used to reduce noise on the low-amplitude spectra at larger L. Scattered light effects were significantly suppressed by placing a highly absorptive foil beneath the device during all measurements. The resistance-capacitance time constant of the measurement circuit was < 100 ns and the amplifier rise-time was < 2 µs; both many orders of magnitude shorter than the current response from the samples.

5.5 Electrically injected lateral diffusion device

As a check on the current measurements performed optically, electrically injected lateral current devices were fabricated. The electrical injection device had the structure: p-type Si (20 Ω/□) / 500 nm SiO_2 / 10 nm BPhen / 50 nm C_{60} / 50 nm Ag / 20 nm DTDCPB:C_{70} 1:1 / 8 nm BPhen / 100 nm Ag. The 50 nm thick Ag layer (collecting contact), and the 100 nm thick Ag layer (injecting contact) were patterned into 1 mm × 18 mm parallel strips using a shadow mask, separated by 1 cm. The substrate oxide was etched in a small area away from the device to allow contact with the Si using buffered HF. For alignment purposes, two electrically inactive Ag strips positioned above the collecting contact were deposited simultaneously with the injecting contact. We used the same HJ / channel / electron blocking layer structure

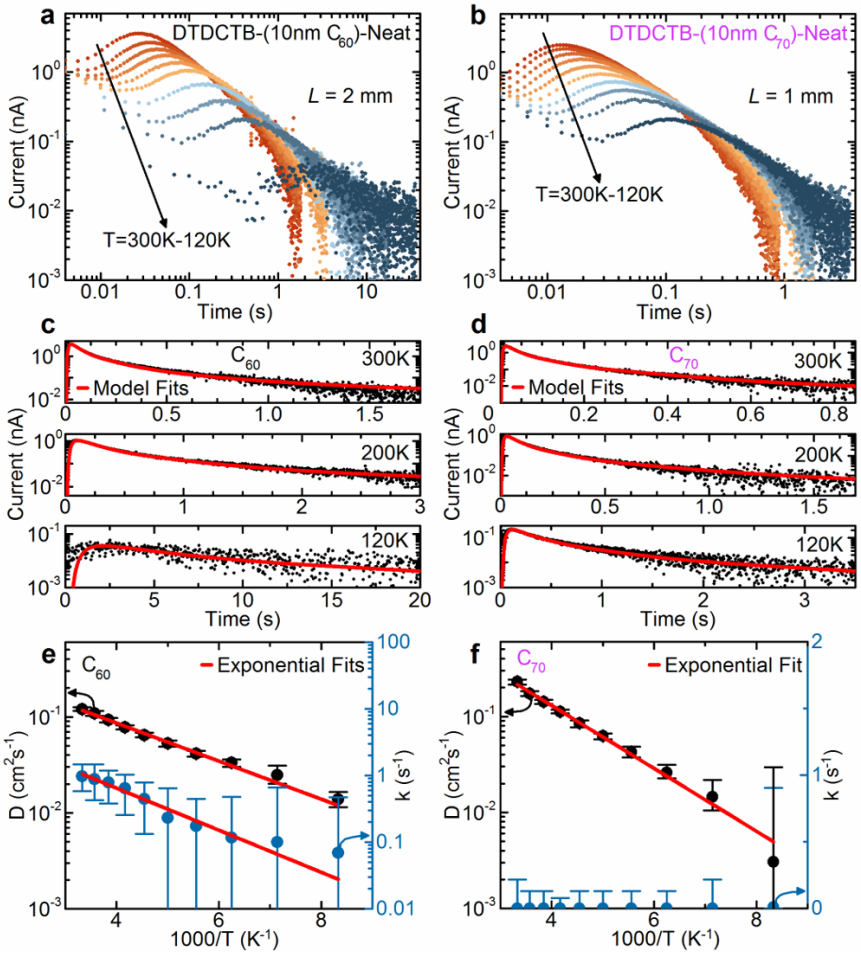

Figure 5.4: **Temperature dependence of channel currents.** Temperature dependent transient photocurrent data at 20K intervals from 300K to 120K in response to 2 ms pulses of 637 nm wavelength illumination on a (a) DTDCTB-(10 nm C_{60})-Neat device at $L = 2$ mm and a (b) DTDCTB-(10 nm C_{70})-Neat device at $L = 1$ mm. Data (points) and corresponding charge diffusion model fits (lines) at 300K, 200K, and 120K for the (c) DTDCTB-(10 nm C_{60})-Neat and (d) DTDCTB-(10 nm C_{70})-Neat device. Diffusivity, D, and (f) k, vs. temperature (T) extracted from the simulations in (c) and (d) for the (e) DTDCTB-(10 nm C_{60})-Neat, and (f) DTDCTB-(10 nm C_{70})-Neat device. Lines show fits to the parameters.

to enable a direct comparison between the electrical and optical devices, although long-range diffusion is expected with any trap-free blocking interface. This structure is shown schematically in Fig. 5.5a, with a photograph of the device in Fig. 5.5b, inset.

Transient current measurements of the electrical injection device were performed in the dark, under vacuum, and at room temperature. The Si substrate was grounded, the injecting contact was connected to a pulse generator, and the current transient at the collecting contact was measured with a current amplifier (10^7 V/A, 10 ms rise-time filter) and digital oscilloscope. The results are shown in Fig. 5.5b. The falling edge of the electrical injection device transient was also simulated using the same diffusion model as above, where electrons were generated at a constant rate beneath the injecting contact until a steady-state current was reached at the collecting electrode. The collecting contact was placed at $x = 0$, with the edge of the injecting contact at $x = 1$ cm. The parameters D and k measured for DTDCPB-(10 nm C_{60})-Neat device in Table 5.1 were used in the calculation.

5.6 Analysis of results

The rates of trapping/recombination at defects and thermal emission into the HJ where recombination can occur determine the lifetime of electrons in the channel. A sufficiently high HJ energy barrier and low defect densities are therefore required to enable transport over macroscopic distances. In devices with d-a-a' donors, the energy levels of C_{70} undergo a polarization shift due to the high dipole moments of DTDCTB and DTDCPB (14.5 and 12.0 Debye, respectively)[104,108]. This shift forms the required energy barrier at the C_{60} channel/HJ interface (0.42 ± 0.1 eV for DTDCPB, as shown in Fig. 5.3a) that confines electrons within the channel. Monte Carlo simulations confirm that this barrier supports centimeter-scale diffusion, whereas in DBP or SubPc donor devices with barrier heights < 100 meV have a much smaller

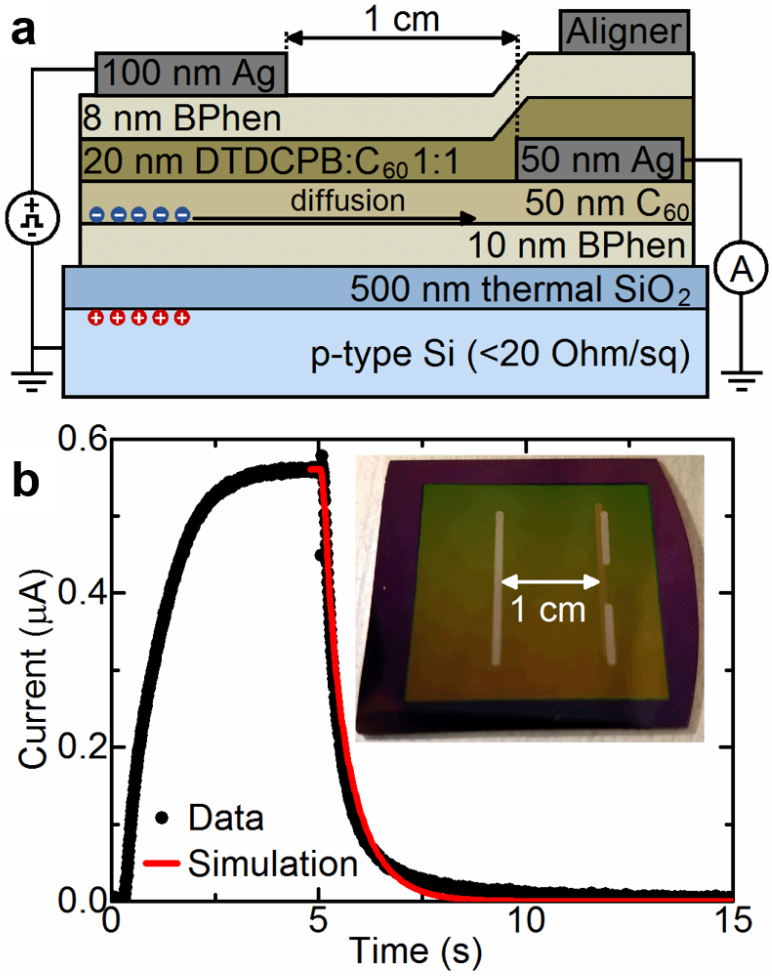

Figure 5.5: **Electron diffusion in an electrical injection device.** A device was fabricated to characterize charge diffusion in an electron-only electrically injected channel, with the structure shown in (a). Charges were injected into the C_{60} channel by applying a 50 V pulse between the injecting contact and the Si substrate for 5 s. The transient current collected at the buried contact is shown in (b). A steady state current of 0.56 μA is observed approximately 3 s after the start of the pulse, with an exponential decay time of about 400 ms. A simulation of the turn-off transient using the same optically measured parameters for D and k in Table 5.1 for the DTDCPB-(10 nm C_{60})-Neat device, is also shown in (b) (solid line). The small deviations of the fits to the electrical data are likely due to slow de-trapping of charges in the BPhen and SiO2 that are injected during the 50 V pulse. Inset: Photograph of the device with 1 cm scale bar.

$L_D < 5$ µm. The centimeter-scale L_D observed in devices with d-a-a' donors suggests that in addition to the large E_B, the channel and its interfaces have a remarkably low density of deep electron traps and recombination centers. This is surprising for fullerenes, which, despite their unusually high mobility and diffusivity among molecular solids[109–111], form disordered and phase-separated amorphous and crystalline domains[112]. Long-range electron diffusion was also observed to circumvent barriers introduced by physical cuts to the channel (Fig. 5.2), as well as in an electron-only charge injecting sample (Fig. 5.5). Indeed, measurements of D and k in these experiments are completely consistent with values obtained via photogeneration in Figs. 5.1 and 5.4. We note that drift-dominated charge lateral spreading drift of charges over long time periods has been observed in single-carrier devices at organic/insulator interfaces due to the lack of recombination[113]. Our results are inherently different since the electron transport in our case is entirely diffusive. Here the surprising phenomena is associated with the bulk, and is observed despite the presence of optically generated minority carrier holes.

Replacing the 10 nm C_{60} layer with C_{70} reduces D from 0.67 ± 0.06 cm^2/s to 0.16 ± 0.01 cm^2/s at room temperature. The Einstein relation, $D = \mu k_B T/q$, where q is the electron charge, suggests that the larger D observed in the C_{60} devices is consistent with its higher mobility[114,115]. This relation can also be used to estimate the electron mobility of each device, as listed in Table 5.1, although we note that D/μ in some organic systems has been shown to be larger than that predicted by the Einstein relation due to disorder in the conduction site energies[116]. We find that the room temperature mobilities, $\mu = 26 \pm 3$ cm^2/V-s for C_{60} and 6 ± 1 cm^2/V-s for C_{70}, are 2-5 times higher than those previously reported for fullerenes in transistors[109,110]. In general, mobilities in bulk semiconductors are larger than those at interfaces due to interfacial traps[117,118], while mobilities and diffusivities in disordered semiconductors typically increase with charge density due to filling of shallow traps and low-energy

states in the conduction band tail[119]. The devices measured here are therefore nearly ideal for achieving high mobility, as charge transport occurs in the bulk of the channel with electron densities $> 10^{17}$ cm^{-3}.

The diffusivities of DTDCTB-(10 nm C_{60})-Neat and DTDCTB-(10 nm C_{70})-Neat devices are thermally activated with $E_A = 70 \pm 8$ meV and $E_A = 36 \pm 3$ meV respectively (see Fig. 5.4e and 5.4f). The exponential decrease in D with temperature is confirmation that conduction is limited by intermolecular hopping[120] even though mobilities as high as those measured here are often attributed to band-like transport. In the C_{70} device, k decreases as a function of temperature ($E_A = 50 \pm 11$ meV) with nearly the same E_A as D, suggesting that its L_d is approximately the mean free path between collisions with sparsely distributed defects. In the C_{60} devices, best fits give $k < 0.1$ s^{-1}, which suggests that the electron lifetime is longer than the timescale of the transient measurements. The values of D and k for C_{60} devices, therefore, cannot be used to accurately predict L_D. This is consistent with the fact that the total charge collected in the transient measurements does not decrease systematically with distance. However, we estimate an error of $\sim 25\%$ in the amount of total charge collected, thus a lower bound on diffusion length can be calculated using $exp(-1/L_D) = 0.75$, which yields $L_D > 3.5$ cm.

5.7 Summary

Centimeter-scale electron diffusion is demonstrated in a photoactive, fullerene-based heterostructure, with room temperature diffusivities of $D = 0.67 \pm 0.06$ cm^2/s for C_{60} and $D = 0.16 \pm 0.01$ cm^2/s for C_{70}, with thermal activation energies of $E_A = 70 \pm 8$ meV and $E_A = 36 \pm 3$ meV, respectively. Among the structures explored, long-range diffusion was only observed when using d-a-a' dipolar donors in the photoactive D-A HJ adjacent to the electron conducting channel. The highly dipolar donors destabilize the HOMO energy of C_{70} by 0.42 ± 0.1 eV in the blends, thereby

providing energetic confinement of electrons in the channel. Monte Carlo simulations aided in understanding these results by confirming that even the lower bound of this measured energy barrier (0.32 eV) is sufficient to support centimeter-scale diffusion in the channel. The surprisingly long diffusion lengths suggest the nearly total absence of recombination centers at interfaces or within the conducting fullerene channels, even though the materials form disordered films. These results may prove useful when applied in devices where long range charge transport is required. For example, channel currents may open the possibility for organic optoelectronic devices with unique properties, such as semi-transparent photovoltaics with large-period metal grid cathodes, organic field effect transistors[121], and lateral photovoltaics[122]. Additionally, energetically confined channels suggest that Hall-effect and lateral time-of-flight experiments are possible for the accurate characterization of organic materials. However, the presence of such channels can also result in anomalously high short-circuit currents during photovoltaic operation. In this circumstance, care must be taken to prevent the overestimation of solar cell efficiency, particularly for small area devices if the active area is overfilled by the illumination source.

CHAPTER VI

Organic charged-coupled devices

The demonstration of centimeter-scale lateral transport makes new types of organic devices possible. Perhaps the most common thin film lateral transport inorganic semiconductor device is the CCD, which manipulates charge packets near a semiconductor-insulator interface, allowing the charge packets to be passed between closely spaced metal-oxide-semiconductor (MOS) capacitors. Since their conception in 1970[123,124], CCDs have been successfully applied to high sensitivity optical imaging, and are valued for their excellent signal-to-noise ratio, high quantum efficiency, linearity, and speed[125,126]. Because practical sensors require charges to transport laterally across millimeter-to-centimeter distances for imaging, CCDs based on organic semiconductors have not been practical due to their typically low charge diffusivities and short carrier lifetimes. However, the recent demonstration of efficient charge transport across distances of several centimeters in organic thin film heterostructures using energetic barriers to physically separate electron and hole polarons[99], as described in Ch. V, opens the possibility for realizing organic charge-coupled devices (OCCDs).

Here, we demonstrate an OCCD that transfers photogenerated electron packets across a 1.78 cm long, linear, three-phase shift register. Reaching the end of the reg-

ister, the packets are read out, providing information about the intensity and spatial distribution of the incident light. In contrast to the operation of conventional CCDs that attract minority carriers to depletion regions at the semiconductor-insulator interface, the electrodes of the n-type organic semiconductor shift register are negatively biased to manipulate charge via repulsive potential barriers that extend through the thin film semiconductor.

6.1 Charge manipulation in lateral channels

Single pixel devices, with layer dimensions shown in Fig. 6.1, were fabricated to test the ability to confine, and subsequently release photogenerated charge packets using a bias applied to the guard electrode. Glass substrates having a strip of 11 mm wide, 70 nm thick prepatterned ITO in the center were cleaned via sequential sonication in tergitol, deionized water, acetone, and isopropanol. A stripe of 50 nm thick Al was deposited by vacuum thermal evaporation (VTE) to form the guard electrode, positioned parallel to the ITO. An 50 nm thick Al_2O_3 grown by atomic layer deposition (ALD) using sequential gas pulse/purge cycles of trimethylaluminum and H_2O at 100°C in a chamber with less than 25 mTorr base pressure. The Al_2O_3 layer was patterned via lift-off photolithography, exposing a 1.8 mm diameter circular area of ITO, with the edge of the circle intersecting the patterned edge of the ITO strip. Following patterning of the resist, the oxide layers were deposited and the resist removed by soaking in Remover PG for $>$ 3 hrs at 80°C. All subsequent layers were deposited by VTE and patterned with shadow masks. Circular layers of 10 nm MoO_x and 50 nm HJ were patterned centered on and overfilling the exposed ITO. Here, the HJ is 1:1 DTDCPB:C_{70}. A buffer layer of 20 nm thick TPBi / 5 nm thick BPhen, was deposited in a rectangular region to prevent contact of the channel with Al_2O_3, but not covering the HJ over the exposed ITO. A channel patterned layer of 20 nm thick C_{60} and buffer of 5 nm thick BPhen / 3 nm TPBi was deposited through a shadow

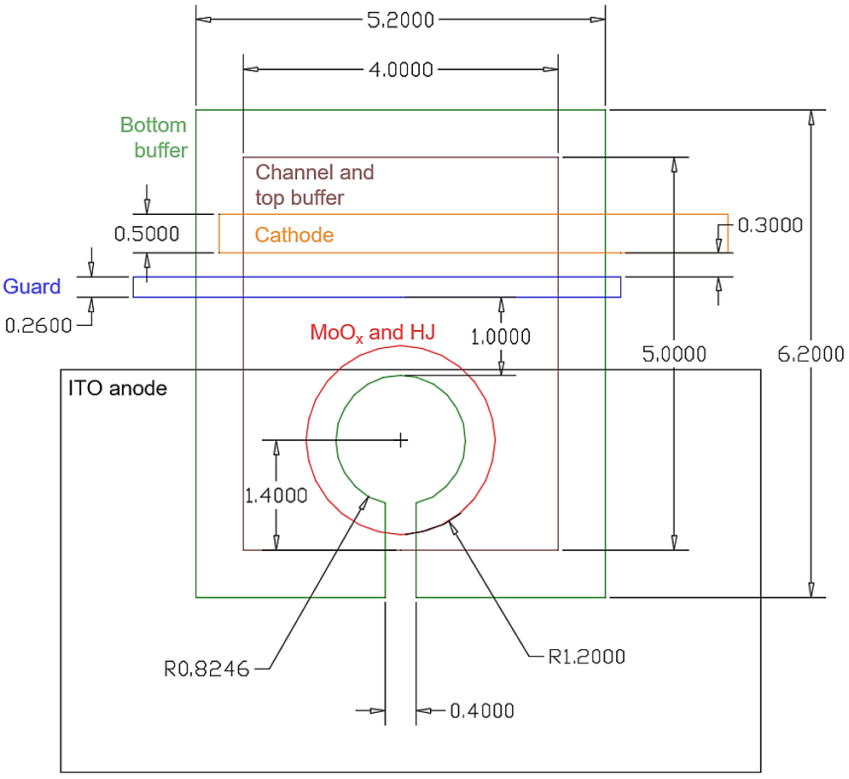

Figure 6.1: **Single pixel device dimensions.** The ITO is prepatterned (extent of the ITO is not shown to scale). Subsequent layer deposition order is Al guard, Al_2O_3 (not shown, it covers everywhere except the circular area of the bottom buffer), MoO_x and HJ, bottom buffer, channel and top buffer, then cathode. All units are in mm.

mask. Finally, a 50 nm thick, 0.5 mm wide stripe Ag cathode was deposited parallel to and spaced 0.3 mm from the insulated guard electrode, on the side opposite the ITO. Devices were encapsulated using a glass cover slide sealed to the substrate with a bead of UV cured epoxy around its periphery in a N_2 environment with < 1 ppm water and O_2. A desiccant (CaO) was included inside device packages.

These devices are shown schematically in Fig. 6.2a. As with the devices in Ch. V, which have a similar organic layer structure, charges are generated at the HJ when illuminated, with holes collected at the anode. The generated electrons are energetically confined to the C_{60} channel, where they laterally diffuse to the Ag cathode, which is connected to a transimpedance amplifier and are subsequently detected by

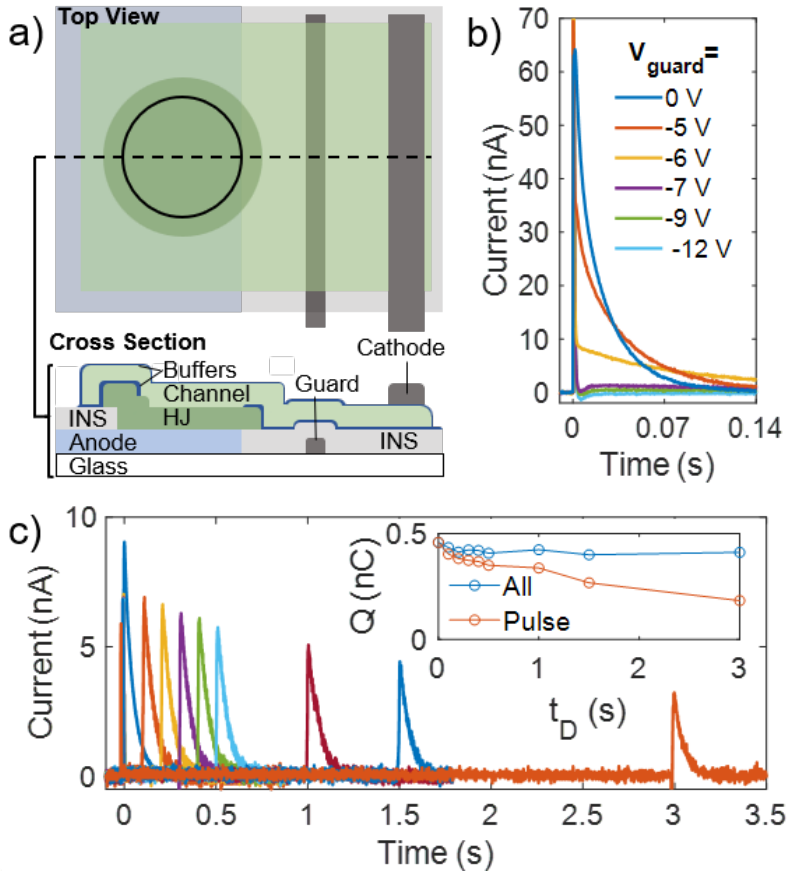

Figure 6.2: **Lateral charge confinement device structure and performance.** (a) Top and cross sectional schematic views of the device structure. (b) Transient photocurrent collected between the anode and cathode with different guard electrode voltages. There is a small displacement current spike at $t = 0$. (c) Transient photocurrent for different storage times. The guard electrode is biased to -7 V prior to the measurement and is switched to 0 V after a delay, t_D, releasing charge generated by a laser pulse at $t = 0$. Current is plotted as the difference between light and dark transients. Inset: Collected charge, Q, vs storage time, integrated over the full trace or for 300 ms after t_D.

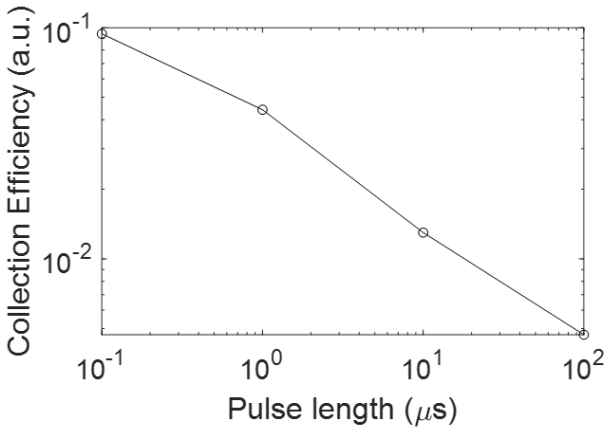

Figure 6.3: **Charge collection efficiency versus pulse length.** Calculated as the number of collected charges divided by the number of incident photons, without blocking potentials applied to the guard electrode. The efficiency rolls off with increasing pulse length due to increased recombination as more light is incident on the heterojunction, because charges are generated faster than they can be extracted laterally through the channel.

an oscilloscope. The efficiency of lateral charge collection decreases with the light intensity on the HJ[99], as shown in Fig. 6.3. This is due to increased recombination in the HJ when the charge generation rate exceeds the collection rate, saturating the channel lying above the generation area. Figure 6.2b shows photocurrent transients stimulated by a laser pulse at $t = 0$ as a function of guard electrode bias. As the guard voltage is changed from $V_{guard} = 0$ to -12 V, the current transient is blocked from reaching the cathode.

Two key observations are made: First, the guard potential required to block electrons (6-10 V) is much higher than would be needed to block electron diffusion if the organic channel contained a negligible amount of free background charge. In the absence of free charge, the electric potential in the channel above the guard approximately equals V_{guard}, because of the proximity of the electrode to the channel relative to other fixed potentials. Blocking is expected at $V_{guard} \leq -1$ V, which is the maximum expected in the channel based on the open circuit voltage of organic

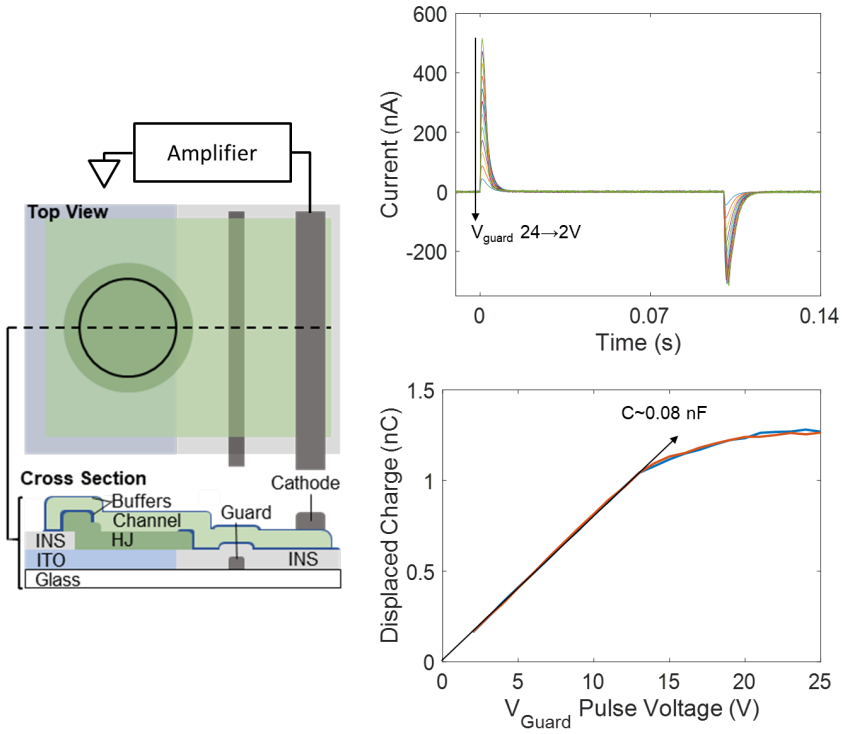

Figure 6.4: **Background charge transients.** (Left) Device schematic and detection circuit. (Top right) Displaced background charge signal. (Bottom right) Total displaced charge versus V_{guard}. The amount of charge displaced rolls off with the onset of photocurrent blocking, which for this sample occurred between 12-14 V.

photovoltaic devices using the same HJ materials[127]. Large displacement current transients due to the capacitance between the channel and guard electrode are measured when switching V_{guard}, shown in Fig. 6.4 together with the measurement circuit and displaced channel. These transients saturate with the onset of charge blocking. They are due to background mobile charge in the channel. Integrating the displaced charge when switching V_{guard} from 0 to -7 V gives 2 ± 1 nC, corresponding to a background charge density of $1.2 \pm 0.6 \times 10^{12}$ cm^{-2} if the area above the electrode is fully depleted under bias.

Second, the measurement should be taken promptly after switching to $V_{guard} < 0$ V. This bias condition attracts positive charge that accumulates at the organic-insulator interface, shielding the C_{60} channel from the guard potential, see Fig. 6.5.

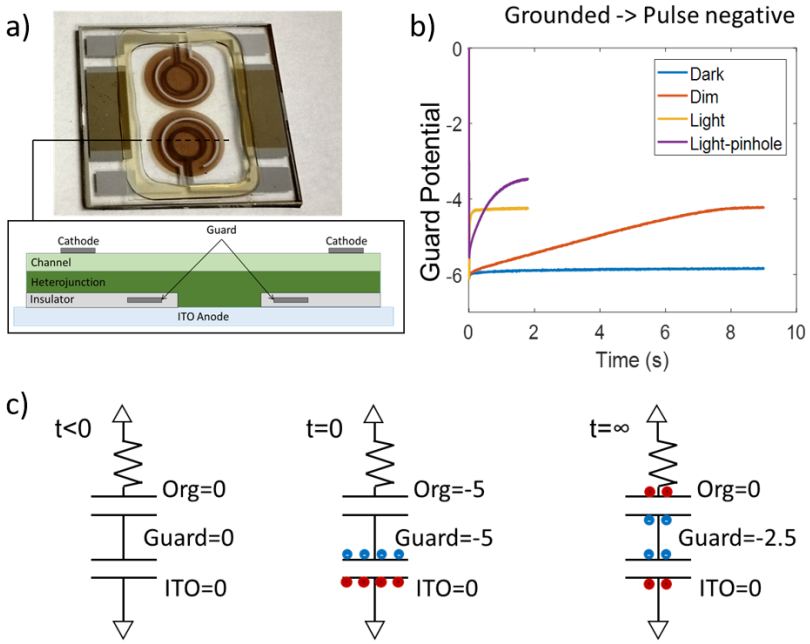

Figure 6.5: **Positive charge accumulation.** (a) Photograph and cross sectional schematic of a modified single pixel device. (B) Transient guard voltage. The potential on the guard ring relaxes to roughly half its initial value on a timescale determined by the light level and exposure area. (C) Equivalent circuit model.

The data in Fig. 6.5 is taken using a modified single pixel device, pictured in Fig. 6.5a. Here, the guard electrode forms a ring surrounding the exposed ITO area, and is insulated on the top and bottom by 50 nm ALD Al_2O_3 layers. The MoO_x / HJ layers were deposited through the same mask as the channel, and the top Ag cathode forms a partial ring enclosing the guard electrode. The HJ, buffer, and channel layer compositions are unchanged from those described above. The guard electrode was left floating, with its voltage measured using a high impedance buffer amplifier (> 1 TΩ). At $t = 0$ the guard voltage was briefly (< 20 ms contact time) set to -6 V. This was carried out in the dark, at two different ambient light levels, and in the light with a mask that confined exposure to the center of the guard ring.

The measurement result can be explained using the equivalent circuit shown in Fig. 6.5c. The guard electrode capacitance is composed of two parts, the capacitance

across the bottom oxide to the ITO and across the top oxide to the organic channel. Before $t = 0$ the guard is uncharged. When the guard is set to -6 V at $t = 0$, the capacitor formed with the ITO is fully charged while the organic channel remains nearly uncharged because of the large impedance between the grounded cathode and the guard. Then, as time progresses, positive charge in the channel collects over the guard, and the guard potential relaxes to approximately 3 V. Light exposure generates free charges in the HJ, and increases the rate of positive charge accumulation, indicated by the faster change in guard voltage at higher light levels. When illuminating only the exposed ITO area, less charge accumulates in the organics during the brief contact with the -6 V potential, causing the final voltage to be closer to -3 V than for the unmasked measurements. Subsequent experiments confirmed that confining the HJ such that it does not overlap the guard electrode reduces the rate of photogenerated positive charge accumulation to negligible levels on the time scale of the measurements (< 20 s).

To determine if photogenerated charges are stored or recombine when blocked, we measured the difference between current transients with and without a laser pulse. Here, V_{guard} swings from 0 V to -7 V, and the resulting current transient from displaced background charge is allowed to dissipate. A pulse of light then illuminates the HJ at $t = 0$, and V_{guard} is returned to 0 V after a delay, t_D. The difference between current in the presence or absence of the pulsed illumination is shown in Fig. 6.2c. Figure 6.6 shows individual light and dark transients. Photogenerated transient current pulses are visible even for $t_D = 3$ s, where the peak intensity decreases with increasing charge storage time. Integrating the collected charge, Q, (see Fig. 6.2c, inset) for the full transient shows that Q is relatively unchanged up to 3 s. The magnitude of the pulse is reduced by charge leakage across the guard electrode rather than recombination, which can be avoided by applying a larger guard bias.

Metal electrodes (5 nm Ti / 50 nm Al) for the shift register, shutter, and guard

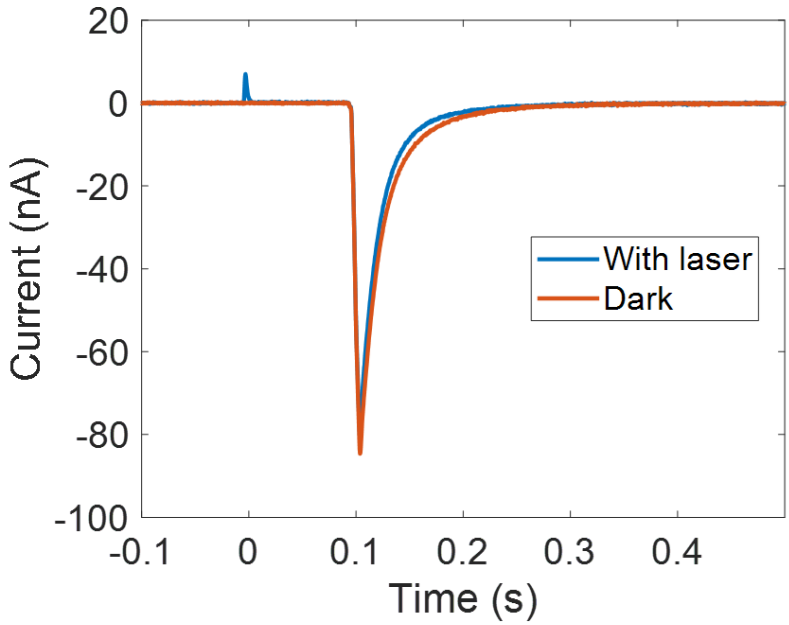

Figure 6.6: **Light and dark pixel transients.** The guard electrode of the single pixel device is initially biased to $V_{guard} = -7$ V. Data is shown both in the dark and for a laser pulse focused onto the heterojunction at $t = 0$. At $t = 1$ s, V_{guard} is switched to 0 V. A large current pulse is observed as background charge flows back into the channel over the guard electrode. When the laser pulse is used, stored charge reduces the amount of charge injected back into the channel from the cathode.

were patterned on a glass substrate by photolithography and covered with 50 nm ALD Al_2O_3 (masking contact pad areas using a gel strip). Next, the Ag anode (as with all subsequent layers) was patterned with a shadow mask and deposited by VTE. Then MoO_x and HJ layers were patterned into four squares over the anode, aligned with every third shift register electrode. Next, a bottom buffer of 20 nm TPBi / 5 nm BPhen was deposited covering the periphery of the heterojunction and the full shift register. Then, a 20 nm C_{60} channel and 5 nm BPhen / 3 nm TPBi top buffer layers were deposited, slightly underfilling the shift register and covering the HJs, with 1 mm wide interconnects between each HJ and the shift register area. The Ag cathode was deposited over the channel and top buffer layers where they extend past the guard electrode. Mask dimensions are given in Fig. 6.7.

The four-pixel OCCD is shown schematically in Fig. 6.8a. Of the 13 insulated electrodes, 11 define the shift register and one each forms the guard and shutter electrodes. A Ag anode runs parallel to the shutter electrode on the side opposite the shift register. The three shift register phases are denoted $\Phi_1 - \Phi_3$. The electrode nearest the guard electrode is Φ_1, followed by Φ_2, Φ_3, Φ_1, etc. (see Fig. 6.8a). A photograph of the device is shown in Fig 6.8b.

Photocurrent is collected between the anode and cathode in response to illumination of the HJ without biasing the electrodes. This current can be cut off by biasing any one of the shutter, guard, or Φ_1 electrodes (at < -8 V), since they completely bisect the channel connecting the HJs to the cathode. We demonstrate charge coupled transport by first biasing Φ_2, Φ_3, and shutter electrodes to -10 V, and $V_{guard} = -8.75$ V. This expels charge from the channel above the biased electrodes, leaving background charge packets confined above Φ_1. The shift register is clocked using a three-phase scheme shown in Fig. 6.9a-b, advancing the charge packets toward the cathode. The first few steps of this process are shown schematically in Fig. 6.9a. Because $V_{guard} > -10$ V, charges diffuse towards the cathode when expelled

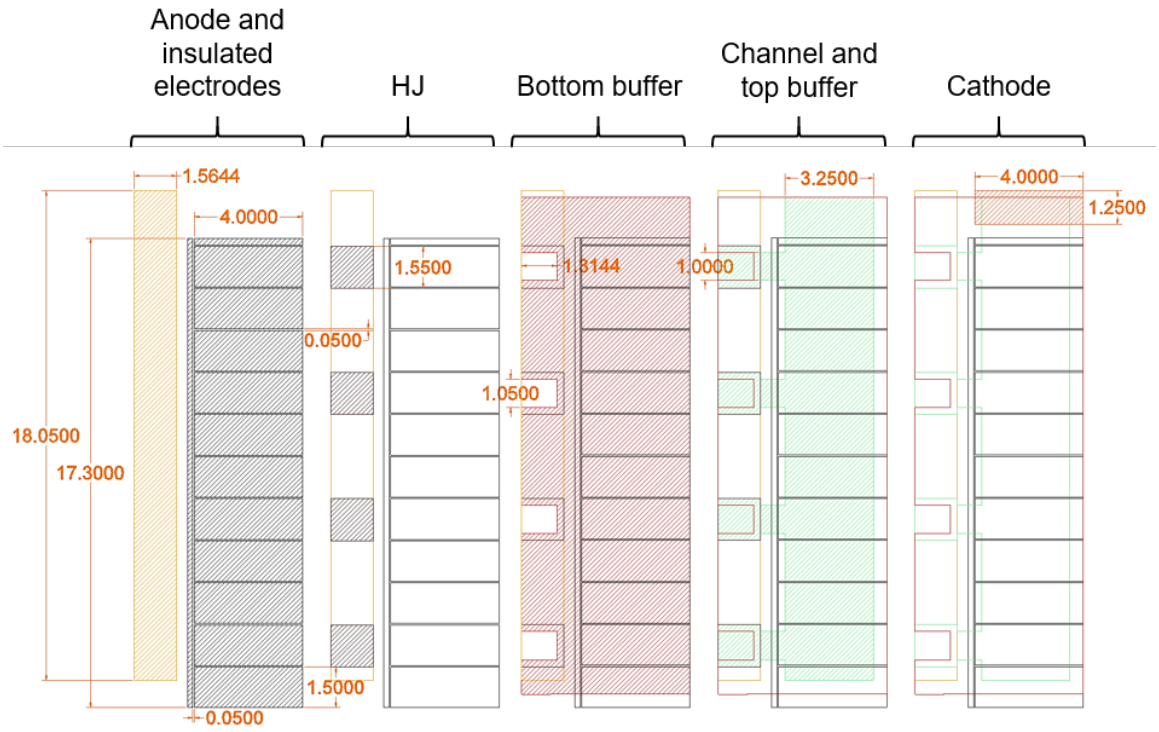

Figure 6.7: **OCCD mask dimensions.** Mask patterns are shown sequentially from left to right: First the insulated electrodes are patterned by photolithography and coated with Al_2O_3. The anode (gold hashed area, left) is the patterned via deposition through a shadow mask. All subsequent areas are also patterned by shadow mask. First, the HJ, then bottom buffer, channel and top buffer, and finally the cathode. All dimensions are in mm. Contact traces and alignment marks are omitted for clarity.

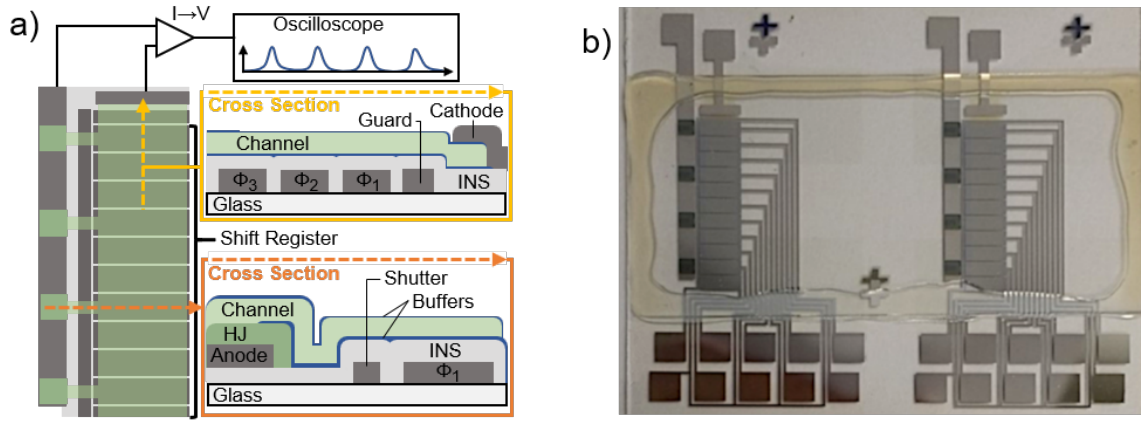

Figure 6.8: **OCCD Structure and device photograph.** (a) Top and cross sectional schematic views of the OCCD and measurement circuit. (B) Photograph of OCCD. Two devices are patterned side by side on one substrate. The guard, shutter, and Φ_3 have a single contact pad each, while Φ_1 and Φ_2 electrodes have multiple pads that are connected externally. Also visible in the picture are the contact pads and traces, alignment marks, and encapsulation cover slide attached to the substrate using UV cured epoxy.

from above the adjacent Φ_1 electrode, preventing charge from flowing back into the shift register.

The current measured during this procedure and the electrode potentials vs time are shown in Fig 6.9b. Here, $t = 0$ corresponds to the first clock cycle when Φ_1 is negatively biased. Current pulses are measured when Φ_1 swings negative with each subsequent clock cycle. The first four pulses reach > 43 nA peak current compared to < 7 nA for subsequent pulses, which decrease with continued clocking. If $V_{guard} = 0$ V while clocking, negative current pulses are observed each time Φ_1 is switched to ground, drawing background charge into the shift register. Similarly, if the shutter potential $V_{shutter} = 0$ V, pulses following the fourth clock cycle do not decrease because charge packets are replenished through the channels connecting the HJs and Φ_1.

The photogenerated charge measurement begins by expelling background charge as explained above, then pausing for exposure with $\Phi_1 = 0$ V and Φ_2, $\Phi_3 = -12$ V. Next, $V_{shutter}$ swings to -9.6 V, which is just sufficient to block background charge

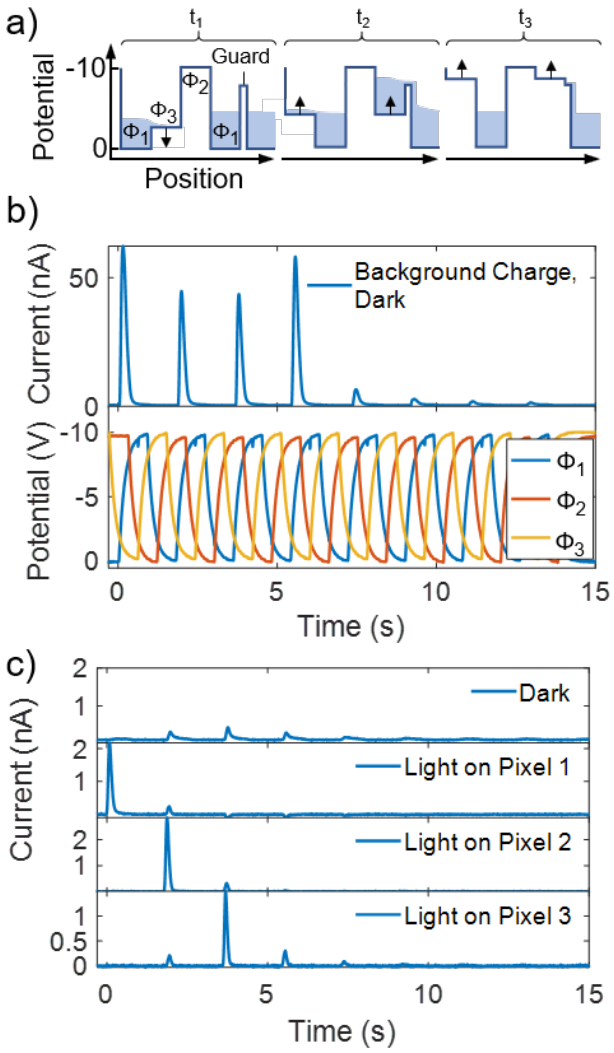

Figure 6.9: **OCCD readout scheme and signal.** (a) Schematic diagram of potential sequence for electrodes at the end of the shift register. Here, sequential snapshots of the electrode potentials are shown at times $t_1 - t_3$. High potentials repel the electron charge packets, indicated as shaded areas. (b) Top: Measured signal from expulsion of background charge, as described in the text. Bottom: voltage vs time for Φ_1-Φ_3 during the measurement. Current pulses are measured each time Φ_1 swings negative. (b) Measured signal for dark and single pixel illumination exposures. Here, $t = 0$ corresponds to the first time Φ_1 swings negative following exposure.

from leaking into the shift register during a single clock cycle in the dark. Then, one HJ is illuminated with a $\lambda = 637$ nm wavelength laser, generating charges and raising the potential of electrons in the channel. This increases the rate of electrons leaking from the illuminated HJ over the shutter. Following exposure, $V_{shutter}$ is switched back to -12 V and the shift register is emptied by a series of eight clock cycles. Figure 6.9c shows the measured current in the dark, and with illumination focused onto one pixel per measurement, resulting in a distinct current pulse observed at a time delay corresponding to the illuminated pixel.

Using majority carrier electrons to store information represents a significant difference from conventional CCD architectures that transfer minority carriers. Using majority carriers precludes using attractive potentials (positive electrode bias, in the case of electrons) to confine charge packets because no depletion region would form. Additionally, the shift register and photoactive regions are spatially separated, since extracting photogenerated holes from the HJ requires circuit connectivity that prevents depletion. This scheme is general and is also applicable to inorganic devices. Conventional CCD architectures are also suitable for OCCDs provided they use long-range lateral diffusion structures for minority carriers or charge depleted channels.

Vacuum deposited films of pre-purified C_{60} have been reported to be weakly n-type, with background charge densities ranging from $10^7 - 10^{11}$ cm^{-3} [128–130] and estimated donor densities of 10^{14} cm^{-3} [128]. The charge density measured here corresponds to $4 \pm 2 \times 10^{17}$ cm^{-3} if the background charge is confined within the channel, and likely includes effects from unintentional bulk [128–130] or interface doping [131,132]. Blocking via repulsive potentials is achieved once the channel above the electrode is depleted of background charge. Reducing the background charge density, for example by further purification of the materials, is therefore expected to reduce the voltage required to block the lateral current. The minimum blocking voltage may be limited by energetic disorder leading to tail states in the distribution of transport sites, which likely plays

a role in the charge leakage over the blocking potentials, as shown in Fig. 6.2c.

The four large current pulses in Fig. 6.9b correspond to the four charge packets over the Φ_1 electrodes. The small subsequent pulses are due to residual background charges in the regions between electrodes as well as imperfect transfer of the photo-generated charge. These parasitic signal pulses can be reduced by overlapping the electrodes to eliminate the intervening spaces, and optimization of phase potential waveforms. Variations in the magnitude of the first four pulses is likely a result of nonuniformities in fabrication, the transfer process at the first and last pixel, and the phase waveforms. The reduction in pulse magnitude after the fourth pulse confirms charge coupled transport.

The transfer rate between adjacent electrodes is approximated from the solution to the drift-diffusion equation, $n(x,t) = D\nabla^2 n(x,t) - \mu F_x \nabla n(x,t)$, subject to boundary conditions $\delta_x n(L,t) = \mu F_x n(L,t)$ and $n(0,t) = 0$, which correspond to perfect charge blocking and extraction, respectively. Here, n is the charge density, $D = 0.8$ cm^{2}s^{-1} is the electron diffusivity and $\mu = 30.8$ cm^2/v-s the mobility (obtained from the Einstein relation at room temperature)[99], and L is the pixel width. Also, F_x is the lateral electric field in the channel that we assume is constant for simplicity, i.e. we neglect self-repulsion and the spatial dependence of fringe fields[133]. The time required for 99.99% charge transfer between adjacent electrodes, t_{CT}, is shown in Fig. 6.10 as a function of electric field. The readout time for an $N \times N$ matrix of pixels ($N \gg 1$) using a three-phase clock scheme is $t_{RO} \approx t_{CT}(3 \times N)^2/N_{amp}$, where N_{amp} is the number of readout amplifiers. In the diffusion limit, a 500×500 pixel sensor with $N_{amp} = 4$ requires 6-7 micron pixels to achieve $t_{RO} < 1$ s, while 10 micron pixels and $N_{amp} = 500$ (1 per column) yields $t_{RO} < 20ms$. Introducing drift transport significantly decreases t_{RO}, for example by fringing fields as shown in Fig. 6.10, inset. This analysis neglects charges trapped at defects or in the tail of the transport density of states, which may reduce the charge transfer speed and collection efficiency.

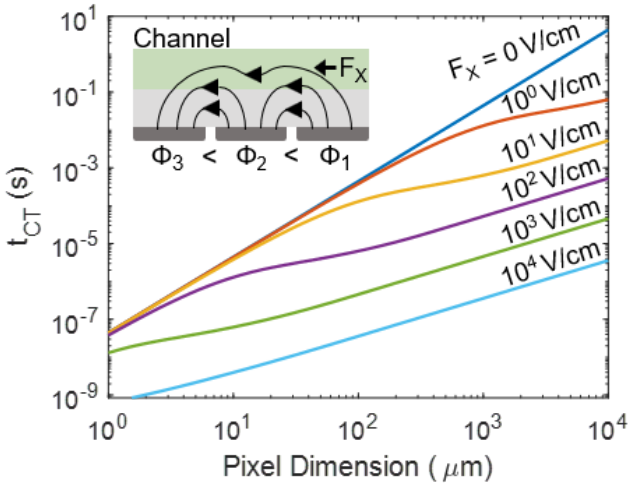

Figure 6.10: **Simulated charge transfer time versus pixel dimension.** The transfer time, t_{CT}, is calculated from the solution to the drift-diffusion equation using $D = 0.8$ cm^{-1} and $\mu = 30.8$ cm^{-1}s^{-1} as the time at which 99.99% of the initial uniform charge distribution has transferred to the adjacent electrode. Blocking and zero density boundary conditions, as well as a uniform electric field, are assumed. The inset shows the concept of drift-inducing fringing fields and direction of the lateral field.

Despite the inherently lower charge mobility in organic compared to inorganic semiconductors, OCCDs have the advantage of being potentially less difficult to manufacture in flexible, ultralight, and large area form factors, which could potentially be of use in simplifying complex optical systems. Organic CCDs may be especially compelling for space applications, where their low weight [134,135], low sensitivity to cosmic radiation [136,137], and reduced requirements for encapsulation are advantageous. They can function as an element in ultralight optical imaging systems when used with thin film Fresnel lenses [138], or as lightweight memory devices. Additionally, stacked, semi-transparent OCCDs with spectrally resolved absorption characteristics could have near 100% pixel fill factor in each color and generate color images without color filters.

6.2 Summary

We have demonstrated a charge coupled device comprising an organic semiconductor thin film deposited on a series of closely spaced, insulated electrodes. Charge coupled transport is demonstrated for both thermally and photogenerated charge packets. The packets are confined using repulsive potentials, which contrasts with conventional inorganic semiconductor CCDs that transport minority carriers using a staircase of attractive potentials. This work demonstrates the versatility of organic semiconductors and paves the way for further development of high performance OCCDs. These may find use is imaging applications where their flexible, ultralight form factors and other attributes of organic semiconductors (e.g. radiation hardness) are required.

CHAPTER VII

Future work

7.1 Future work: OLEDs

7.1.1 Reliability

Important areas for the further development of OLED technology include increasing their power efficiency and reliability. Of these, reliability was the primary focus of the work presented in this thesis. The reliability of blue PHOLEDs is one of the most important remaining challenges. Based on studies of blue phosphorescent device degradation[6,42,67], and including Ch III of this work, intrinsic degradation of the emissive layer materials in blue emitting devices limits their useful lifetime. Strategies involving device structure[32] and reducing the intrinsic degradation due to hot states[83] have proven effective for improving blue lifetime. However, substantial further progress will likely require new chemicals for both host and dopant, incorporating strong intra-molecular bonds and appropriate energy levels to reduce molecular dissociation. Growth methods for reducing morphological changes during operation, such as aggregate formation and crystallization, may also yield reliability improvements.

7.1.2 Power efficiency

One promising route for reaching the thermodynamic limit for power efficiency is the use of exciplex-forming cohost systems[139–141]. This strategy avoids energy loss due to difference between the transport level offset and the exciton energy. Energy transfer from exciplexes directly to phosphors additionally avoids exchange energy losses, or the difference in the singlet and triplet exciton energies. One example device using this scheme is shown in Fig. 7.1. In this device, a single electron transporting, exciplex forming cohost material and three sequentially layered hole transporting, exciplex forming cohost materials form the host structure for the EML. The HOMO-LUMO offset of each pairing of the electron transporting host with the hole-transporting hosts is matched to the triplet energy of a red, green, or blue phosphor. Thus, injected carriers which recombine in red, green, or blue emitting regions have transport gaps nearly equal to the emission energy of the dopants in those regions. Cohosts are ordered such that no carrier has an exothermic hopping step when transporting through the device to avoid thermalization losses. Because it avoids energy loss from exciton relaxation, this structure has a theoretical power efficiency higher than hybrid fluorescent/phosphorescent white devices and traditional all-phosphorescent devices, such as those presented in Ch. IV. Devices employing a single hole transporting host with multiple electron transporting hosts, other permutations of host combinations, and stacked single-color exciplex-cohost devices are also possible. Additionally, conductivity-doped transport layers and injection or blocking layers may be used with this scheme to realize an OLED near the thermodynamic limit for power efficiency.

7.1.3 Charge balance and exciton confinement

There are additional areas to be explored using the methods for understanding charge balance presented in Ch. II-III. New chemicals and architectures will likely

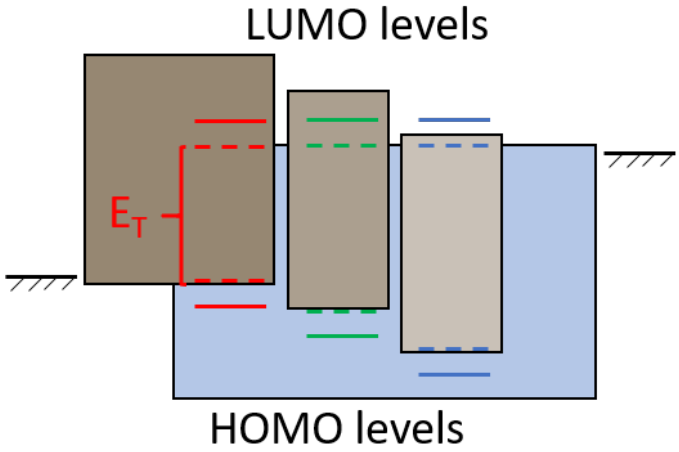

Figure 7.1: **Proposed high power efficiency white OLED energy level diagram.** Energy level diagram showing HOMO and LUMO levels (horizontal solid lines) and triplet levels of phosphors (dashed lines). Exciplex-forming cohosts have HOMO-LUMO gaps matched to the triplet levels of the emitters, with one hole transporting cohost material per emitter type.

demonstrate very different behaviors for charge balance and exciton confinement vs. current density and operating time, which will need to be tested as they are developed. In addition to being useful tools for maximizing the performance of new device architectures and chemicals, these methods may also be useful for improving our understanding of fundamental processes in OLEDs. For example, classic experiments investigating efficiency roll-off in PHOLEDs[142] assume that charge balance does not change with current, which may not be accurate at high current density where roll-off is significant. Quantitative measurements of charge balance vs current density coupled with roll-off analyses may be a powerful tool for understanding the role of TTA and TPA in both roll-off and lifetime.

7.2 Future work: OCCDs

Like the first demonstrations of Si CCDs, the concept of the OCCD presented in Ch. VI requires significant improvements and development to bring the technology

to a mature stage. Developing OCCDs has the advantage of using the development of conventional CCDs as a road map, however new and unique challenges specific to the organic devices will require innovation. Important areas for the further development of OCCDs, listed in a suggested order of priority, include: control over background charge density through doping and material purification, pixel-scaling, integrated readout circuitry, drift-transport schemes, and stacked semitransparent arrays. Each of these is addressed briefly below.

7.2.1 Controlling background charge density

Control over doping density for both electrons and holes in silicon CCDs has been essential to their success. For example, the doping density is directly related to the charge capacity-per-area of the pixels, and both n and p-type dopants are needed for buried-channel devices[125]. The electrode voltages and device structure in the OCCD demonstrated in Ch. VI were in large part dictated by the background charge density. Understanding the origin of and controlling the background charge density will be important to making higher performance devices. Experiments of interest include measuring the background charge density vs. material purity (or number of thermal gradient sublimation steps), intentional channel doping using n and p-dopants (for example lithium and MoO_x), as well as material surveys to test alternative buffer layers that may contribute to the the background charge density via interfacial doping. Additionally, hole conducting channels should be possible, and might be of use in OCCDs if the mobilities are comparable or higher than for electrons. Materials combinations for p-type channels should have similar energetics to n-type channels, i.e, the channel HOMO should be shallow compared to the HOMO levels in the HJ and buffer layers. Channel mobility might be best determined using electrical injection structures such as in Fig. 5.5.

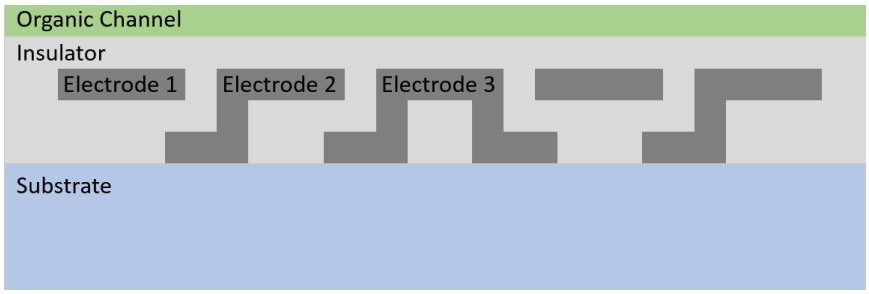

Figure 7.2: **Diagram of OCCD electrodes.** Electrodes are separated from the organic channel by an insulator layer of uniform thickness. Insulator layers of a similar thickness prevent shorting between adjacent electrodes, which are overlapping. Note that the drawing is not to scale: electrode widths are micron-scale while organic and insulator layer thicknesses are nanometer-scale.

7.2.2 Pixel-scaling

There are a number of considerations when scaling OCCD pixel size and number. First, micron-scale gaps between adjacent shift register electrodes are not acceptable in high performance devices, especially with pixel dimensions < 100 microns. Indeed, practical devices require electrode spacings on the order of the insulator thickness, as shown in Fig. 7.2. This scheme of overlaping adjacent electrodes significantly reduces potential wells and barriers between electrodes, and should improve charge transfer efficiency.

Additionally, high charge transfer efficiency becomes increasingly important as the number of pixels (and therefore transfer steps) increases. The amount of charge remaining in a charge packet after n transfers scales as $(\eta_{CTE})^n$. The fractional amount of charge remaining in a charge packet after n transfer steps is shown in Fig. 7.3 for various values of η_{CTE}. Extremely high charge transfer efficiency is required to maintain signal intensity over the millions of transfers required for a megapixel sensor. Energetic disorder of transport sites and interface or bulk traps pose a serious concern– no electron may be left behind when transferring charge packets. This may place an upper limit on both readout speed and the number of pixels OCCDs can

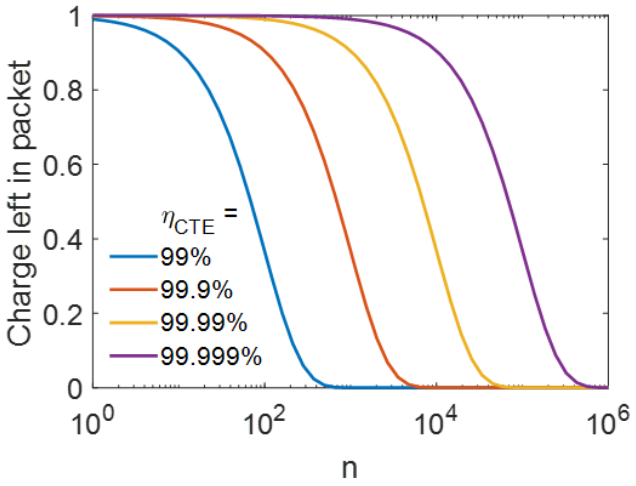

Figure 7.3: **Charge packet integrity vs number of transfers.** The amount of charge remaining in the original charge packet decreases with each transfer when $\eta_{CTE} < 1$. Lost charge is smeared out behind the original packet, degrading the signal integrity of subsequent charge packets.

achieve. It is therefore necessary that η_{CTE} be well characterized for practical OCCDs.

7.2.3 Integrated readout circuitry

In Ch VI, charge packets were measured using a current amplifier. While this is adequate for the large (mm) pixel sizes and slow (ms) transfer times, high performance devices require special purpose, integrated readout circuitry. Indeed, a significant portion of the research and development of Si CCDs has been devoted to low noise, low capacitance readout structures. Two styles of readout sensors used for conventional inorganic CCDs, floating diffusion and floating gate amplifiers, are pictured in Fig. 7.4. Both styles amplify a voltage shift at the gate of the transistor connected in series with a gain resistor R_{gain}, producing a signal at V_{out}. A constant V_{DD} is applied to the drain of the readout transistor to power the amplifier. In the case of the floating gate (Fig. 7.4a), charge diffusing out of the shift register is directly collected onto the (temporarily floating) electrode, causing a voltage shift. After measurement, the electrode bias is reset to V_{-} by pulsing V_{reset} to briefly turn on the reset

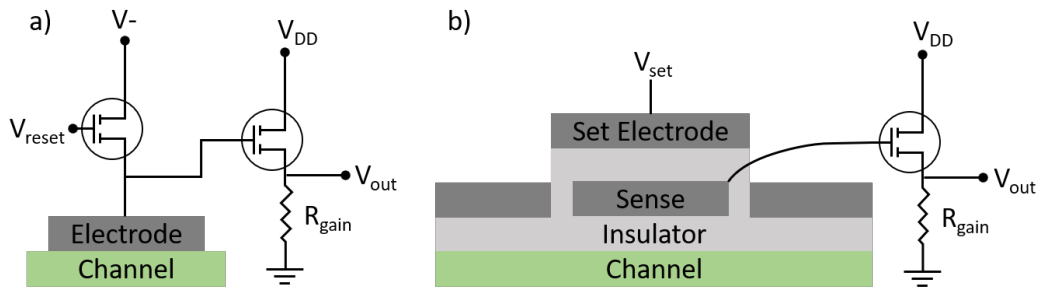

Figure 7.4: **Readout amplifiers styles.** (a) A floating diffusion amplifier. Here, the electrode is biased at V_{-} to attract signal charge. The reset transistor is then turned off and a charge packet is released from the shift register, which diffuses to the electrode. The amount of charge and the capacitance of the electrode determine the voltage shift after collecting the charge packet. The voltage shift is measured by a second transistor in series with a gain resistor. Finally, V_{reset} is pulsed to turn the reset transistor on briefly to reset the electrode potential in preparation for reading the next charge packet. (b) A floating gate amplifier. Biasing the set electrode to V_{set} capacitively biases the sense electrode. The sense electrode is patterned in the out-of-page direction and connected to the insulated gate of the transistor. Charge packets passing under the sense electrode cause its potential to decrease, producing an amplified signal at V_{out}.

transistor, preparing the amplifier for the next charge packet. Rather than coming at the end of the shift register, the floating gate amplifier[143] (Fig. 7.4b) replaces one of the shift register electrodes. The set electrode is biased to V_{set}, which capacitively couples to the sense electrode. Charge packets passing through the channel near the sense electrode change its potential, generating a signal. Because the transistor gate is insulated, the sense electrode is always floating, and its potential is modified capacitively, without a change in net charge. Unlike the destructive measurement by the floating diffusion method, the floating gate amplifier preserves the charge packet after measurement, allowing a single charge packet to be measured multiple times.

The capacitance of the amplifier input is inversely related to the voltage change per signal electron, requiring fF scale amplifier capacitance for high gain ($\sim$µV/e). Organic thin film transistors are process compatible with OCCD fabrication steps and may find use in these readout circuits.

7.2.4 Drift-transport schemes

Charge transfer speed can be increased compared to a purely diffusive system by introducing a lateral field and drift transport. Shift register electrode structures for applying lateral fields in OCCDs include thick insulator, many electrode, and resistive-sheet electrode structures. Each is described below.

7.2.4.1 Thick insulator scheme

Increasing the insulator thickness relative to the electrode dimension causes the potential of a charge-neutral channel to deviate from the underlying electrode potentials. This introduces lateral field across the channel over an electrode when the adjacent electrodes have different potentials. An example of this is shown in Fig. 7.5. To calculate the channel potential, Laplace's equation $\nabla^2 V = 0$ is solved in two dimensions on a rectangular area. The potential on the side of interest, which corresponds to the electrodes of the shift register, is a stepwise function determined by the electrode biases along the length of the shift register, while the remaining three boundaries are set to 0 V and placed $\gg L = 5$ µm away from the region of interest, where L is the length of an electrode. For this example, a single 5 µm electrode is placed symmetrically about $x = 0$, with very wide ($\gg 5$ µm) electrodes on either side. The leftmost electrode is biased at 1 V, the central electrode is biased at 0.5 V, and the right electrode is set to 0 V. The channel potential in the absence of free charge is taken as the potential along a line parallel to electrode boundary, offset by a variable insulator thickness. For insulators $\ll 5$ µm, the channel potential approximates the electrode potential at the same lateral position. As the oxide thickness increases, the channel potential blurs and the potential slope (lateral field) over the center of the 5 µm pixel increases. This scheme has the disadvantage of reduced charge capacity-per-area due to the thick insulator layer.

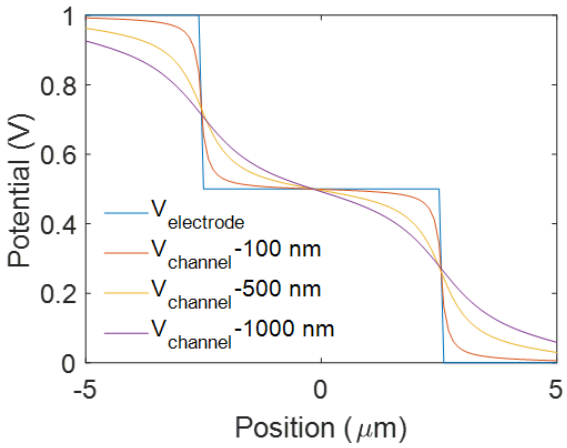

Figure 7.5: **Thick insulator scheme.** Electrode and channel potential as a function of lateral position for different insulator thicknesses. As the insulator thickness increases from 100 nm to 1000 nm, the potential in the channel deviates more from the electrode potential, causing significant potential slope at the center of the 5 µm pixel when it is biased at a value intermediate to the potentials of the neighboring electrodes.

7.2.4.2 Many electrode scheme

The many electrode scheme is a simple extension of the thick insulator scheme: if the electrode dimension is reduced, the oxide thickness required to achieve lateral field is also reduced. In this scheme, many electrodes are used to confine a single charge packet, allowing the potential in the channel to be shaped with a lateral resolution determined by the electrode size and insulator thickness. This is shown in Fig 7.6. Here, the same dimensions are used as for Fig. 7.5, except that the central electrode is subdivided into five electrodes. This scheme allows a thinner insulator at the cost of increased fabrication and operational complexity.

7.2.4.3 Resistive-sheet electrode scheme

An alternative to subdividing the electrodes is to use a thin film sheet resistor to connect a series of very thin conductive electrodes. In this scheme, shown schematically in Fig. 7.7, lateral field in the channel arises when two adjacent electrodes have different potentials. A simple four-phase transport scheme for charge packets in a

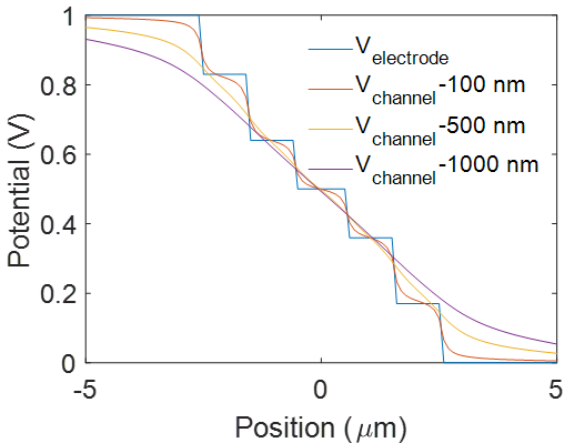

Figure 7.6: **Many electrode scheme.** Electrode and channel potential as a function of lateral position for different insulator thicknesses. Reducing the electrode width and increasing the number of electrodes per pixel allows uniform potential slope in the channel to be realized with a much thinner insulator.

resistive-sheet electrode shift register is also shown in Fig. 7.7, which is analogous to a three-phase conventional shift register scheme. Adding more phases will improve the charge capacity per area of the pixels. The resistive-sheet electrode scheme has the advantage of simplifying processing, since the shift register electrodes can be patterned in a single step without having gaps between pixels. It also improves charge capacity-per-area compared to the previous drift-transport schemes because the insulator thickness can be minimized without negatively affecting the lateral field strength. However, it will dissipate power in the resistive-sheets even without switching, resulting in a trade-off between power draw, switching speed, and charge capacity.

7.2.5 Stacked semitransparent arrays

Organic photoactive structures are well suited to semitransparent or flexible devices. One possibility for a high performance OCCD is a stacked structure having multiple semitransparent OCCDs layered on top of each other on a single substrate. The absorption spectra of the photoactive regions of the devices could be chosen individually, for example one each having absorption in the red, green, and blue por-

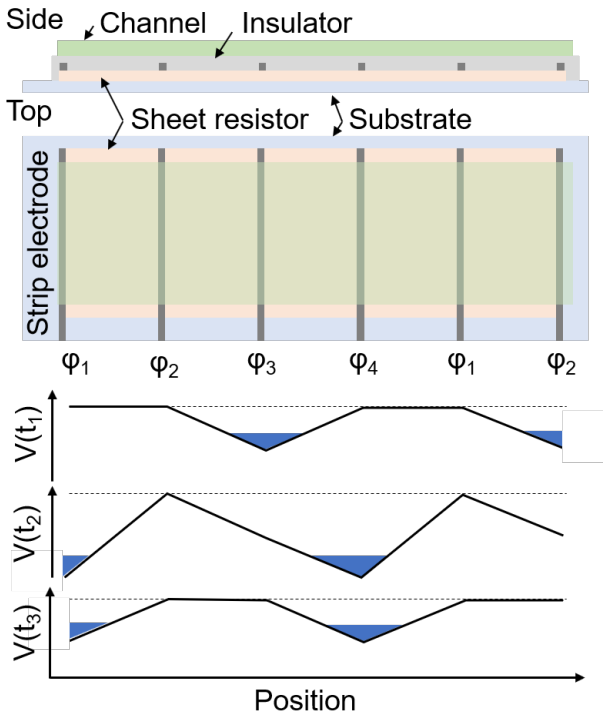

Figure 7.7: **Resistive-sheet electrode scheme.** (Top) Schematic of a resistive-sheet electrode shift register. Thin patterned electrodes are deposited on a strip of thin film sheet resistor. (Bottom) Diagram of a charge packet being transported along the shift register using a four phase scheme.

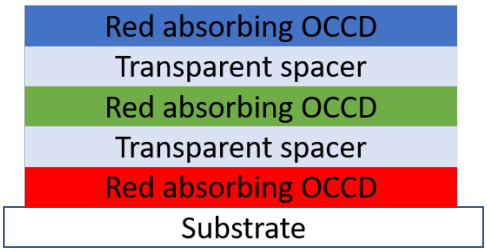

Figure 7.8: **Stacked semitransparent OCCD diagram.** Concept diagram for a stacked OCCD. Semitransparent OCCDs having separate wavelength response are stacked on a single substrate, separated by transparent spacers.

tions of the visible spectrum. Such a device could produce a high resolution color image without the need for color filters. High resolution is possible because different color-absorbing pixels could be stacked vertically rather than patterned laterally. Transparent spacer regions, possibly incorporating transparent ground planes could be employed to prevent electrical interference between OCCDs. The substrate could be flexible or rigid, transparent or opaque. All electrodes would be transparent.

APPENDIX

APPENDIX A

List of published work

JOURNAL PUBLICATIONS

[1] Coburn, C., Fan, D., Forrest, S.R., An organic charge-coupled device. *Manuscript in preparation* (2019).

[2] Coburn, C., Burlingame, Q., Che, X., Panda, A., Qu, Y., Forrest, S.R., Centimetre-scale electron diffusion in photoactive organic heterostructures. *Nature* **554**, 77–80 (2018).

[3] Coburn, C., Jeong, C., Forrest, S.R., Reliable, all-phosphorescent stackled white organic light emitting devices with a high color rendering index. *ACS Photonics* **5**, 630–635 (2017).

[4] Coburn, C., Forrest, S.R., Effects of charge balance and exciton confinement on the operational lifetime of blue phosphorescent organic light-emitting diodes. *ACS Photonics* **7**, 041002 (2017).

[5] Coburn, C., Lee, J., Forrest, S.R., Charge balance and exciton confinement in phosphorescent organic light emitting diodes. *Advanced Optical Materials* **4**, 889-895 (2016).

[6] Shi, S., Jung, M.C., Coburn, C., Tadle, L., Sylvinson, M.R., Djurovich, P., Forrest, S.R., Thompson, M.E., Highly efficient photo-and electroluminescence from two-Coordinate Cu (I) complexes featuring nonconventional N-heterocyclic carbenes. *Journal of the American Chemistry Society* **141**, 3576–3588 (2019).

[7] Idris, M., Coburn, C., Fleetham, T., Milam-Guerrero, J., Djurovich, P., Forrest, S.R., Thompson, M.E., Phenanthro [9, 10-d] triazole and imidazole derivatives: High triplet energy host materials for blue phosphorescent organic light emitting devices. *Material Horizons*, DOI: 10.1039/C9MH00195F (2019).

[8] Fan, D., Lee, B., Coburn, C., Forrest, S.R., From 2D to 3D: Strain-and elongation-free topological transformations of optoelectronic circuits. *Proceedings of the National Academy of Sciences* **116**, 3968–3973 (2019).

[9] Jeong, C., Coburn, C., Idris, M., Li, Y., Djurovich, P., Thompson, M.E., Forrest, S.R., Understanding molecular fragmentation in blue phosphorescent organic light-emitting devices. *Organic Electronics* **64**, 15–21 (2019).

[10] Kim, J., Qu, Y., Coburn, C., Forrest, S.R., Efficient outcoupling of organic light-emitting devices using a light-scattering dielectric layer. *ACS Photonics* **5**, 3315–3321 (2018).

[11] Qu, Y., Kim, J., Coburn, C., Forrest, S.R., Efficient, nonintrusive outcoupling in organic light emitting devices using embedded microlens arrays. *ACS Photonics* **5**, 2453–2458 (2018).

[12] Lee, J., Jeong, C., Batagoda, T., Coburn, C., Thompson, M.E., Forrest, S.R., Hot excited state management for long-lived blue phosphorescent organic light-emitting diodes. *Nature Communications* **8**, 15566 (2017).

[13] Qu, Y., Coburn, C., Fan, D., Forrest, S.R., Elimination of plasmon losses and enhanced light extraction of top-emitting organic light-emitting devices using a reflective subelectrode grid. *ACS Photonics* **4**, 363–368 (2017).

[14] Lee, J., Chen, H.F., Coburn, C., Djurovich, P., Thompson, M.E., Forrest, S.R., Deep blue phosphorescent organic light-emitting diodes with very high brightness and efficiency. *Nature Materials* **15**, 92 (2016).

[15] Kwon, M.S., Yu, Y., Coburn, C., Phillips, A., Chung, K., Shanker, A., Jung, J., Kim, G., Pipe, K., Forrest, S.R., Youk, Y., Gierschner, J., Kim, J., Suppressing molecular motions for enhanced room-temperature phosphorescence of metal-free organic materials. *Nature Communications* **6**, 8947 (2015).

CONFERENCE PRESENTATIONS

[1] Coburn, C., Jeong, C., Forrest, S.R., Reliable, all-phosphorescent stacked white organic light emitting devices with a high color rendering index. *Spring MRS*, Pheonix, AZ (2018)

[2] Coburn, C., Jeong, C., Forrest, S.R., Reliable, all-phosphorescent stacked white organic light emitting devices with a high color rendering index. *Engineering Graduate Symposium*, Ann Arbor, MI (2017)

[3] Coburn, C., Jeong, C., Forrest, S.R., Stable, high efficiency white electrophosphorescent organic light emitting diodes by reduced molecular dissociation. *Department of Energy Workshop*, San Diego, CA (2017)

[4] Coburn, C., Lee, J., Forrest, S.R., Measurement of charge balance and its effect on blue electrophosphorescent organic light emitting diode lifetime *SPIE Optics and Photonics*, San Diego, CA (2015)

PATENTS & DISCLOSURES

[1] Charge coupled device using repulsive electrodes, Caleb Coburn, Dejiu Fan, Stephen Forrest (UM 2019-242), filed 2019

[2] Organic PV device having a lateral transport channel, Caleb Coburn, Quinn Burlingame, Stephen Forrest, disclosed 2017

[3] Stacked white organic light emitting device (UM7829), Caleb Coburn, Changyeong Jeong, Stephen Forrest, filed 2017

[4] ITO/MoO_3 cathode for top-emitting or transparent OLEDs (UM6962), Yue Qu, Caleb Coburn, Stephen Forrest, filed 2016

[5] Organic light emitting diode having a mixed blocking layer, (UM6808), Caleb Coburn, Jaesang Lee, Stephen Forrest, filed 2016

BIBLIOGRAPHY

[1] Baldo, M. A., Lamansky, S., Burrows, P. E., Thompson, M. E. & Forrest, S. R. Very high-efficiency green organic light-emitting devices based on electrophosphorescence. *Applied Physics Letters* **75**, 4–6 (1999).

[2] Adachi, C., Baldo, M. A., Thompson, M. E. & Forrest, S. R. Nearly 100% internal phosphorescence efficiency in an organic light-emitting device. *Journal of Applied Physics* **90**, 5048 (2001).

[3] Förster, T. Zwischenmolekulare energiewanderung und fluoreszenz. *Annalen der Physik* **437**, 55–75 (1948).

[4] Dexter, D. L. A theory of sensitized luminescence in solids. *The Journal of Chemical Physics* **21**, 836–850 (1953).

[5] Baldo, M. A., Adachi, C. & Forrest, S. R. Transient analysis of organic electrophosphorescence. II. Transient analysis of triplet-triplet annihilation. *Physical Review B - Condensed Matter and Materials Physics* **62**, 10967–10977 (2000).

[6] Giebink, N. C. *et al.* Intrinsic luminance loss in phosphorescent small-molecule organic light emitting devices due to bimolecular annihilation reactions. *Journal of Applied Physics* **103**, 044509 (2008).

[7] Celebi, K., Heidel, T. D. & Baldo, M. A. Simplified calculation of dipole energy transport in a multilayer stack using dyadic Green's functions. *Optics Express* **15**, 1762 (2007).

[8] Möller, S. & Forrest, S. R. Improved light out-coupling in organic light emitting diodes employing ordered microlens arrays. *Journal of Applied Physics* **91**, 3324–3327 (2002).

[9] Qu, Y., Coburn, C., Fan, D. & Forrest, S. R. Elimination of plasmon losses and enhanced light extraction of top-emitting organic light-emitting devices using a reflective subelectrode grid. *ACS Photonics* **4**, 363–368 (2017).

[10] Qu, Y., Kim, J., Coburn, C. & Forrest, S. R. Efficient, nonintrusive outcoupling in organic light emitting devices using embedded microlens arrays. *ACS Photonics* **5**, 2453–2458 (2018).

[11] Kim, J., Qu, Y., Coburn, C. & Forrest, S. R. Efficient outcoupling of organic light-emitting devices using a light-scattering dielectric layer. *ACS Photonics* **5**, 3315–3321 (2018).

[12] Wright, W. D. A re-determination of the trichromatic coefficients of the spectral colours. *Transactions of the Optical Society* **30**, 141–164 (1929).

[13] Guild, J.; Petavel, J. E. The colorimetric properties of the spectrum. *Philosophical Transactions of the Royal Society A: Mathematical, Physical and Engineering Sciences* **230**, 149–187 (1932).

[14] CIE (Commission Internationale de l'Eclairage). *Method of measuring and specifying colour rendering properties of light sources*, vol. 20 (Commission internationale de l'eclairage, CIE Central Bureau, 1995).

[15] Forrest, S. R., Bradley, D. D. C. & Thompson, M. E. Measuring the efficiency of organic light-emitting devices. *Advanced Materials* **15**, 1043–1048 (2003).

[16] Rajagopal, A., Wu, C. I. & Kahn, A. Energy level offset at organic semiconductor heterojunctions. *Journal of Applied Physics* **83**, 2649–2655 (1998).

[17] Peumans, P., Yakimov, A. & Forrest, S. R. Small molecular weight organic thin-film photodetectors and solar cells. *Journal of Applied Physics* **93**, 3693–3723 (2003).

[18] Liu, X., Li, Y., Ding, K. & Forrest, S. Energy loss in organic photovoltaics: Nonfullerene versus fullerene acceptors. *Physical Review Applied* **11**, 024060 (2019).

[19] Giebink, N. C., Wiederrecht, G. P., Wasielewski, M. R. & Forrest, S. R. Ideal diode equation for organic heterojunctions. I. Derivation and application. *Physical Review B* **82**, 155305 (2010).

[20] Giebink, N. C., Lassiter, B. E., Wiederrecht, G. P., Wasielewski, M. R. & Forrest, S. R. Ideal diode equation for organic heterojunctions. II. The role of polaron pair recombination. *Physical Review B* **82**, 155306 (2010).

[21] Chopra, N. *et al.* Effect of the charge balance on high-efficiency blue-phosphorescent organic light-emitting diodes. *ACS Applied Materials & Interfaces* **1**, 1169–72 (2009).

[22] Ikai, M., Tokito, S., Sakamoto, Y., Suzuki, T. & Taga, Y. Highly efficient phosphorescence from organic light-emitting devices with an exciton-block layer. *Applied Physics Letters* **79**, 156 (2001).

[23] O'Brien, D. F., Baldo, M. A., Thompson, M. E. & Forrest, S. R. Improved energy transfer in electrophosphorescent devices. *Applied Physics Letters* **74**, 442 (1999).

[24] Meerheim, R. *et al.* Influence of charge balance and exciton distribution on efficiency and lifetime of phosphorescent organic light-emitting devices. *Journal of Applied Physics* **104**, 014510 (2008).

[25] Erickson, N. C. & Holmes, R. J. Investigating the role of emissive layer architecture on the exciton recombination zone in organic light-emitting devices. *Advanced Functional Materials* **23**, 5190–5198 (2013).

[26] Coburn, C., Lee, J. & Forrest, S. R. Charge balance and exciton confinement in phosphorescent organic light emitting diodes. *Advanced Optical Materials* **4**, 889–895 (2016).

[27] Park, I.-S. *et al.* Modeling and simulation of electronic and excitonic emission properties in organic host–guest systems. *Organic Electronics* **11**, 218–226 (2010).

[28] Staudigel, J., Stobel, M., Steuber, F. & Simmerer, J. A quantitative numerical model of multilayer vapor-deposited organic light emitting diodes. *Journal of Applied Physics* **86**, 3895 (1999).

[29] Horowitz, G. Organic field-effect transistors. *Advanced Materials* **10**, 365–377 (1998).

[30] Malliaras, G. G. & Scott, J. C. Numerical simulations of the electrical characteristics and the efficiencies of single-layer organic light emitting diodes. *Journal of Applied Physics* **85**, 7426 (1999).

[31] Zhang, Y. & Forrest, S. R. Triplet diffusion leads to triplet–triplet annihilation in organic phosphorescent emitters. *Chemical Physics Letters* **590**, 106–110 (2013).

[32] Zhang, Y., Lee, J. & Forrest, S. R. Tenfold increase in the lifetime of blue phosphorescent organic light-emitting diodes. *Nature Communications* **5**, 5008 (2014).

[33] Sun, Y. *et al.* Management of singlet and triplet excitons for efficient white organic light-emitting devices. *Nature* **440**, 908–912 (2006).

[34] Djurovich, P. I., Mayo, E. I., Forrest, S. R. & Thompson, M. E. Measurement of the lowest unoccupied molecular orbital energies of molecular organic semiconductors. *Organic Electronics* **10**, 515–520 (2009).

[35] Hill, I. G., Kahn, A., Cornil, J., dos Santos, D. A. & Bredas, J. L. Occupied and unoccupied electronic levels in organic pi-conjugated molecules: comparison between experiment and theory. *Chemical Physics Letters* **317**, 444–450 (2000).

[36] Nakanotani, H., Masui, K., Nishide, J., Shibata, T. & Adachi, C. Promising operational stability of high-efficiency organic light-emitting diodes based on thermally activated delayed fluorescence. *Scientific Reports* **3**, 2127 (2013).

[37] Mikhnenko, O. V., Ruiter, R., Blom, P. W. M. & Loi, M. A. Direct Measurement of the Triplet Exciton Diffusion Length in Organic Semiconductors. *Physical Review Letters* **108**, 137401 (2012).

[38] Nguyen, N. D., Schmeits, M. & Loebl, H. P. Determination of charge-carrier transport in organic devices by admittance spectroscopy: Application to hole mobility in α -NPD. *Physical Review B* **75**, 075307 (2007).

[39] Hosokawa, C., Tokailin, H., Higashi, H. & Kusumoto, T. Transient behavior of organic thin film electroluminescence. *Applied Physics Letters* **60**, 1220 (1992).

[40] Matsusue, N., Ikame, S., Suzuki, Y. & Naito, H. Charge carrier transport in an emissive layer of green electrophosphorescent devices. *Applied Physics Letters* **85**, 4046 (2004).

[41] Lee, S.-B., Yasuda, T., Yang, M.-J., Fujita, K. & Tsutsui, T. Charge carrier mobility in vacuum-sublimed dye films for light-emitting diodes studied by the time-of-flight technique. *Molecular Crystals and Liquid Crystals* **405**, 67–73 (2003).

[42] Giebink, N. C., D'Andrade, B. W., Weaver, M. S., Brown, J. J. & Forrest, S. R. Direct evidence for degradation of polaron excited states in organic light emitting diodes. *Journal of Applied Physics* **105**, 4 (2009).

[43] Lin, H. W., Lin, W. C., Chang, J. H. & Wu, C. I. Solution-processed hexaazatriphenylene hexacarbonitrile as a universal hole-injection layer for organic light-emitting diodes. *Organic Electronics* **14**, 1204–1210 (2013).

[44] Staudigel, J., Stossel, M., Steuber, F., Blassing, J. & Simmerer, J. Activation energies in organic light emitting diodes comprising ohmic contacts both for electron and hole injection. *Synthetic Metals* **111**, 69–73 (2000).

[45] Yang, Y. X. *et al.* Ultraviolet-violet electroluminescence from highly fluorescent purines. *Journal of Materials Chemistry C* **1**, 2867–2874 (2013).

[46] Kijima, Y., Asai, N. & Tamura, S. A blue organic light emitting diode. *Japanese Journal of Applied Physics* **38**, 5274–5277 (1999).

[47] Schwartz, G., Reineke, S., Rosenow, T. C., Walzer, K. & Leo, K. Triplet harvesting in hybrid white organic light-emitting diodes. *Advanced Functional Materials* **19**, 1319–1333 (2009).

[48] Tsai, M.-H. *et al.* Triphenylsilyl- and Trityl-Substituted Carbazole-Based Host Materials for Blue Electrophosphorescence. *ACS Applied Materials & Interfaces* **1**, 567–574 (2009).

[49] Zhou, Y. C., Ma, L. L., Zhou, J., Ding, X. M. & Hou, X. Y. Effect of a sensing layer on triplet exciton diffusion in organic films. *Physical Review B* **75**, 132202 (2007).

[50] Wang, Q. & Aziz, H. Degradation of organic/organic interfaces in organic light-emitting devices due to polaron-exciton interactions. *ACS Applied Materials & Interfaces* **5**, 8733–8739 (2013).

[51] Kondakov, D. Y. Role of chemical reactions of arylamine hole transport materials in operational degradation of organic light-emitting diodes. *Journal of Applied Physics* **104**, 84520–84524 (2008).

[52] Kondakov, D. Y., Lenhart, W. C. & Nichols, W. F. Operational degradation of organic light-emitting diodes: Mechanism and identification of chemical products. *Journal of Applied Physics* **101**, 24512–24516 (2007).

[53] Schmidbauer, S., Hohenleutner, A. & Konig, B. Chemical degradation in organic light-emitting devices: Mechanisms and implications for the design of new materials. *Advanced Materials* **25**, 2114–2129 (2013).

[54] Aziz, H., Popovic, Z. D., Hu, N. X., Hor, A. M. & Xu, G. Degradation mechanism of small molecule-based organic light-emitting devices. *Science* **283**, 1900–1902 (1999).

[55] Geffroy, B., Le Roy, P. & Prat, C. Organic light-emitting diode (OLED) technology: materials, devices and display technologies. *Polymer International* **55**, 572–582 (2006).

[56] Sasabe, H. & Kido, J. Development of high performance OLEDs for general lighting. *Journal of Materials Chemistry C* **1**, 1699–1707 (2013).

[57] Coburn, C. & Forrest, S. R. Effects of charge balance and exciton confinement on the operational lifetime of blue phosphorescent organic light-emitting diodes. *Physical Review Applied* **7**, 041002 (2017).

[58] Hochstrasser, R. M. Photoproccesses in the organic solid state. *Photochemistry and Photobiology* **3**, 299–306 (1964).

[59] Bansal, A. K., Holzer, W., Penzkofer, A. & Tsuboi, T. Absorption and emission spectroscopic characterization of platinum-octaethyl-porphyrin (PtOEP). *Chemical Physics* **330**, 118–129 (2006).

[60] Kozlov, V. G., Burrows, P. E., Parthasarathy, G. & Forrest, S. R. Optical properties of molecular organic semiconductor thin films under intense electrical excitation. *Applied Physics Letters* **74**, 1057–1059 (1999).

[61] Kozlov, V. G. *et al.* Structures for organic diode lasers and optical properties of organic semiconductors under intense optical and electrical excitations. *IEEE Journal of Quantum Electronics* **36**, 18–26 (2000).

[62] Baldo, M. A. *et al.* Highly efficient phosphorescent emission from organic electroluminescent devices. *Nature* **395**, 151–154 (1998).

[63] Burrows, H. D., Fernandes, M., de Melo, J. S., Monkman, A. P. & Navaratnam, S. Characterization of the triplet state of tris(8-hydroxyquinoline)aluminium(III) in benzene solution. *Journal of the American Chemical Society* **125**, 15310–15311 (2003).

[64] Makinen, A. J., Hill, I. G. & Kafafi, Z. H. Vacuum level alignment in organic guest-host systems. *Journal of Applied Physics* **92**, 1598–1603 (2002).

[65] Baldo, M. A. & Forrest, S. R. Transient analysis of organic electrophosphorescence: I. Transient analysis of triplet energy transfer. *Physical Review B* **62**, 10958–10966 (2000).

[66] Sandanayaka, A. S. D., Matsushima, T. & Adachi, C. Degradation mechanisms of organic light-emitting diodes based on thermally activated delayed fluorescence molecules. *Journal of Physical Chemistry C* **119**, 23845–23851 (2015).

[67] Jeong, C. *et al.* Understanding molecular fragmentation in blue phosphorescent organic light-emitting devices. *Organic Electronics* **64**, 15–21 (2019).

[68] Song, B., Burlingame, Q. C., Lee, K. & Forrest, S. R. Reliability of mixed-heterojunction organic photovoltaics grown via organic vapor phase deposition. *Advanced Energy Materials* **5**, 1401952 (2015).

[69] Goushi, K., Kwong, R., Brown, J. J., Sasabe, H. & Adachi, C. Triplet exciton confinement and unconfinement by adjacent hole-transport layers. *Journal of Applied Physics* **95**, 7798–7802 (2004).

[70] Tsang, D. P. K. & Adachi, C. Operational stability enhancement in organic light-emitting diodes with ultrathin Liq interlayers. *Scientific Reports* **6** (2016).

[71] Fleetham, T. B., Huang, L., Klimes, K., Brooks, J. & Li, J. Tetradentate Pt(II) complexes with 6-membered chelate rings: A new route for stable and efficient blue organic light emitting diodes. *Chemistry of Materials* **28**, 3276–3282 (2016).

[72] US Department of Energy. 2015 U.S. Lighting Market Characterization — Department of Energy (2015). URL https://www.energy.gov/eere/ssl/2015-us-lighting-market-characterization.

[73] Song, J. *et al.* Lensfree OLEDs with over 50% external quantum efficiency via external scattering and horizontally oriented emitters. *Nature Communications* **9**, 3207 (2018).

[74] Coburn, C., Jeong, C. & Forrest, S. R. Reliable, all-phosphorescent stacked white organic light emitting devices with a high color rendering index. *ACS Photonics* **5**, 630–635 (2018).

[75] Cho, Y. J., Yook, K. S. & Lee, J. Y. Cool and warm hybrid white organic light-emitting diode with blue delayed fluorescent emitter both as blue emitter and triplet host. *Scientific Reports* **5**, 7859 (2015).

[76] Hung, W.-Y. *et al.* A new benzimidazole/carbazole hybrid bipolar material for highly efficient deep-blue electrofluorescence, yellow–green electrophosphorescence, and two-color-based white OLEDs. *Journal of Materials Chemistry* **20**, 10113 (2010).

[77] Tao, Y. *et al.* Multifunctional bipolar triphenylamine/oxadiazole derivatives: highly efficient blue fluorescence, red phosphorescence host and two-color based white OLEDs. *Chem. Commun.* **1**, 77–79 (2009).

[78] Li, G., Fleetham, T. & Li, J. Efficient and stable white organic light-emitting diodes employing a single emitter. *Advanced Materials* **26**, 2931–2936 (2014).

[79] MacAdam, D. L. Visual sensitivities to color differences in daylight. *Journal of the Optical Society of America* **32**, 247–274 (1942).

[80] Liao, L. S., Klubek, K. P. & Tang, C. W. High-efficiency tandem organic light-emitting diodes. *Applied Physics Letters* **84**, 167–169 (2004).

[81] Shen, Z., Burrows, P. E., Bulović, V., Forrest, S. R. & Thompson, M. E. Three-color, tunable, organic light-emitting devices. *Science* **276**, 2009–2011 (1997).

[82] Xia, S. C., Kwong, R. C., Adamovich, V. I., Weaver, M. S. & Brown, J. J. OLED device operational lifetime: insights and challenges. In *2007 IEEE International Reliability Physics Symposium Proceedings. 45th Annual*, 253–257 (2007).

[83] Lee, J. *et al.* Hot excited state management for long-lived blue phosphorescent organic light-emitting diodes. *Nature Communications* **8**, 15566 (2017).

[84] US Department of Energy. US Department of Energy fact sheet: LED Color Stability (2014).

[85] Lee, S., Lee, J. H., Lee, J. H. & Kim, J. J. The mechanism of charge generation in charge-generation units composed of p-doped hole-transporting layer/HATCN/n-doped electron-transporting layers. *Advanced Functional Materials* **22**, 855–860 (2012).

[86] Sun, Y. & Forrest, S. R. Enhanced light out-coupling of organic light-emitting devices using embedded low-index grids. *Nature Photonics* **2**, 483–487 (2008).

[87] Moller, S. & Forrest, S. R. Improved light out-coupling in organic light emitting diodes employing ordered microlens arrays. *Journal of Applied Physics* **91**, 3324–3327 (2002).

[88] Kato, K., Iwasaki, T. & Tsujimura, T. Over 130 lm/W all-phosphorescent white OLEDs for next-generation lighting. *Journal of Photopolymer Science and Technology* **28**, 335–340 (2015).

[89] Reineke, S. *et al.* White organic light-emitting diodes with fluorescent tube efficiency. *Nature* **459**, 234–238 (2009).

[90] Qu, Y., Slootsky, M. & Forrest, S. R. Enhanced light extraction from organic light-emitting devices using a sub-anode grid. *Nature Photonics* **9**, 758–763 (2015).

[91] Wang, Z. B. *et al.* Unlocking the full potential of organic light-emitting diodes on flexible plastic. *Nature Photonics* **5**, 753–757 (2011).

[92] Fery, C., Racine, B., Vaufrey, D., Doyeux, H. & Cina, S. Physical mechanism responsible for the stretched exponential decay behavior of aging organic light-emitting diodes. *Applied Physics Letters* **87**, 213502 (2005).

[93] Meerheim, R., Walzer, K., Pfeiffer, M. & Leo, K. Ultrastable and efficient red organic light emitting diodes with doped transport layers. *Applied Physics Letters* **89**, 61111–61115 (2006).

[94] Liu, B. *et al.* Efficient hybrid white organic light-emitting diodes with extremely long lifetime: the effect of n-type interlayer. *Scientific Reports* **4**, 7198 (2014).

[95] Coropceanu, V. *et al.* Charge transport in organic semiconductors. *Chemical Reviews* **107**, 926–952 (2007).

[96] Bassler, H. Charge transport in disordered organic photoconductors: a Monte Carlo simulation study. *Physica Status Solidi (b)* **175**, 15–56 (1993).

[97] Sarkar, D. & Halas, N. Dember effect in C_{60} thin films. *Solid State Communications* **90**, 261–265 (1994).

[98] Tripathi, A. K., Tripathi, D. C. & Mohapatra, Y. N. Simultaneous and direct measurement of carrier diffusion constant and mobility in organic semiconductors and deviation from standard Einstein relation. *Physical Review B* **84**, 041201 (2011).

[99] Burlingame, Q. *et al.* Centimetre-scale electron diffusion in photoactive organic heterostructures. *Nature* **554**, 77–80 (2018).

[100] Snow cleaning of substrates increases yield of large-area organic photovoltaics. *Applied Physics Letters* **101**, 133901 (2012).

[101] Xiao, X. *et al.* Small-molecule planar-mixed heterojunction photovoltaic cells with fullerene-based electron filtering buffers. *Adv. Energy Mater* **4**, 1301557 (2014).

[102] Burlingame, Q. *et al.* Reliability of small molecule organic photovoltaics with electron-filtering compound buffer layers. *Advanced Energy Materials* **6**, 1601094 (2016).

[103] Xue, J., Rand, B. P., Uchida, S. & Forrest, S. R. A hybrid planar-mixed molecular heterojunction photovoltaic cell. *Advanced Materials* **17**, 66–71 (2005).

[104] Griffith, O. L. *et al.* Charge transport and exciton dissociation in organic solar cells consisting of dipolar donors mixed with C_{70}. *Physical Review B* **92**, 085404 (2015).

[105] Cheyns, D., Kim, M., Verreet, B. & Rand, B. P. Accurate spectral response measurements of a complementary absorbing organic tandem cell with fill factor exceeding the subcells. *Applied Physics Letters* **104**, 093302 (2014).

[106] Olthof, S. *et al.* Ultralow doping in organic semiconductors: Evidence of trap filling. *Physical Review Letters* **109**, 176601 (2012).

[107] Nunomura, S., Che, X. & Forrest, S. R. Charge trapping in mixed organic donor-acceptor semiconductor thin films. *Advanced Materials* **26**, 7555–7560 (2014).

[108] Ting, H.-C. *et al.* Benzochalcogenodiazole-based donor-acceptor-acceptor molecular donors for organic solar cells. *ChemSusChem* **7**, 457–465 (2014).

[109] Itaka, K. *et al.* High-mobility C_{60} field-effect transistors fabricated on molecular-wetting controlled substrates. *Advanced Materials* **18**, 1713–1716 (2006).

[110] Anthopoulos, T. D. *et al.* High performance n-channel organic field-effect transistors and ring oscillators based on C_{60} fullerene films. *Applied Physics Letters* **89**, 213504 (2006).

[111] Kwiatkowski, J. J., Frost, J. M. & Nelson, J. The effect of morphology on electron field-effect mobility in disordered C_{60} thin films. *Nano Letters* **9**, 1085–1090 (2009).

[112] Liu, X., Ding, K., Panda, A. & Forrest, S. R. Charge transfer states in dilute donor–acceptor blend organic heterojunctions. *ACS Nano* **10**, 7619–7626 (2016).

[113] Bürgi, L., Friend, R. H. & Sirringhaus, H. Formation of the accumulation layer in polymer field-effect transistors. *Applied Physics Letters* **82**, 1482–1484 (2003).

[114] Jarrett, C., Pichler, K., Newbould, R. & Friend, R. Transport studies in C_{60} and C_{60}/C_{70} thin films using metal-insulator-semiconductor field-effect transistors. *Synthetic Metals* **77**, 35–38 (1996).

[115] Haddon, R. C. C_{70} thin film transistors. *Journal of the American Chemical Society* **118**, 3041–3042 (1996).

[116] Roichman, Y. & Tessler, N. Generalized Einstein relation for disordered semiconductors—implications for device performance. *Applied Physics Letters* **80**, 1948–1950 (2002).

[117] Sakanoue, T. & Sirringhaus, H. Band-like temperature dependence of mobility in a solution-processed organic semiconductor. *Nature Materials* **9**, 736–740 (2010).

[118] Jurchesu, O. D., Popiniuc, M., van Wees, B. J. & Palstra, T. T. M. Interface-controlled, high-mobility organic transistors. *Advanced Materials* **19**, 688–692 (2007).

[119] Leijtens, T., Lim, J., Teuscher, J., Park, T. & Snaith, H. J. Charge density dependent mobility of organic hole-transporters and mesoporous TiO_2 determined by transient mobility spectroscopy: Implications to dye-sensitized and organic solar cells. *Advanced Materials* **25**, 3227–3233 (2013).

[120] Tummala, N. R., Zheng, Z., Aziz, S. G., Coropceanu, V. & Brédas, J.-L. Static and dynamic energetic disorders in the C_{60}, $PC_{61}BM$, C_{70}, and $PC_{71}BM$ fullerenes. *The Journal of Physical Chemistry Letters* **6**, 3657–3662 (2015).

[121] Torricelli, F., Colalongo, L., Raiteri, D., Kovács-Vajna, Z. M. & Cantatore, E. Ultra-high gain diffusion-driven organic transistor. *Nature Communications* **7**, 10550 (2016).

[122] Kim, M. *et al.* Lateral organic solar cells with self-assembled semiconductor nanowires. *Advanced Energy Materials* **5**, 1401317 (2015).

[123] Boyle, W. S. & Smith, G. E. Charge coupled semiconductor devices. *Bell System Technical Journal* **49**, 587–593 (1970).

[124] Amelio, G. F., Tompsett, M. F. & Smith, G. E. Experimental verification of charge coupled device concept. *Bell System Technical Journal* **49**, 593–600 (1970).

[125] Janesick, J. R., Elliott, T., Collins, S., Blouke, M. M. & Freeman, J. *Scientific charge-coupled-devices*, vol. 26 (1987).

[126] Tiffenberg, J. *et al.* Single-electron and single-photon sensitivity with a silicon skipper CCD. *Physical Review Letters* **119**, 131802 (2017).

[127] Chen, Y. H. *et al.* Vacuum-deposited small-molecule organic solar cells with high power conversion efficiencies by judicious molecular design and device optimization. *Journal of the American Chemical Society* **134**, 13616–13623 (2012).

[128] Ishii, H. *et al.* Kelvin probe study of band bending at organic semiconductor/metal interfaces: Examination of Fermi level alignment. *Physics of Organic Semiconductors* 69–94 (2006).

[129] Kang, S. J. *et al.* Energy level diagrams of C_{60}/pentacene/Au and pentacene/C_{60}/Au. *Synthetic Metals* **156**, 32–37 (2006).

[130] Tanaka, Y., Kanai, K., Ouchi, Y. & Seki, K. Oxygen effect on the interfacial electronic structure of C_{60} film studied by ultraviolet photoelectron spectroscopy. *Chemical Physics Letters* **441**, 63–67 (2007).

[131] Irfan, Zhang, M. L., Ding, H. J., Tang, C. W. & Gao, Y. L. Strong interface p-doping and band bending in C_{60} on MoO_x. *Organic Electronics* **12**, 1588–1593 (2011).

[132] Veenstra, S. C., Heeres, A., Hadziioannou, G., Sawatzky, G. A. & Jonkman, H. T. On interface dipole layers between C_{60} and Ag or Au. *Applied Physics a-Materials Science & Processing* **75**, 661–666 (2002).

[133] Carnes, J. E., Kosonocky, W. F. & Ramberg, E. G. Drift-aiding fringing fields in charge-coupled devices. *IEEE Journal of Solid-State Circuits* **Sc 6**, 322–326 (1971).

[134] Cardinaletti, I. *et al.* Organic and perovskite solar cells for space applications. *Solar Energy Materials and Solar Cells* **182**, 121–127 (2018).

[135] Schreurs, D. *et al.* Methodology of the first combined in-flight and ex situ stability assessment of organic-based solar cells for space applications. *Journal of Materials Research* **33**, 1841–1852 (2018).

[136] Kumar, A. *et al.* Origin of radiation-induced degradation in polymer solar cells. *Advanced Functional Materials* **20**, 2729–2736 (2010).

[137] Paterno, G. M. *et al.* Neutron radiation tolerance of two benchmark thiophene-based conjugated polymers: the importance of crystallinity for organic avionics. *Scientific Reports* **7**, 41013 (2017).

[138] O'Neill, M. J. *et al.* Ultra-light stretched Fresnel lens solar concentrator for space power applications. *Proc. SPIE 5179, Optical Materials and Structures Technologies* **5179**, 116–126 (2003).

[139] Lee, S. *et al.* The role of charge balance and excited state levels on device performance of exciplex-based phosphorescent organic light emitting diodes. *Scientific Reports* **7**, 11995 (2017).

[140] Wang, S. *et al.* Solution-processed phosphorescent organic light-emitting diodes with ultralow driving voltage and very high power efficiency. *Scientific Reports* **5**, 12487 (2015).

[141] Park, Y.-S., Jeong, W.-I. & Kim, J.-J. Energy transfer from exciplexes to dopants and its effect on efficiency of organic light-emitting diodes. *J. Appl. Phys* **110**, 124519 (2011).

[142] Transient analysis of organic electrophosphorescence. II. Transient analysis of triplet-triplet annihilation. *Physical Review B* **62**, 10967–10977 (2000).

[143] Wen, D. Design and operation of a floating gate amplifier. *IEEE Journal of Solid-State Circuits* **9**, 410–414 (1974).